Ա.Ի. Ալիխանյանի անվան ԵՐԵՎԱՆԻ ՖԻԶԻԿԱՅԻ ԻՆՍՏԻՏՈՒՏ

Հակոպով Զավեն Նորայրի

Միջուկային միջավայրում տարբեր տիպի հադրոնների կլանման ուսումնասիրությունը ՀԵՐՄԵՍ գիտափորձի տվյալների հիման վրա

Ա.04.16-« » մասնագիտությամբ ֆիզիկամաթեմատիկական գիտությունների թեկնածուի գիտական աստիճանի հայցման

ատենախոսություն

Գիտական ղեկավար՝ Ակադեմիկոս Ռ.Հ. Ավագյան

Երևան-2006

Yerevan Physics Institute

Zaven Norayr Akopov

Hadron Attenuation in Nuclear Environment at HERMES

Thesis for acquiring the degree of candidate of physical-mathematical sciences in division 01.04.16 “nuclear, elementary particles and cosmic ray physics”

Yerevan-2006

To my beloved father and teacher.

Contents

Introduction

In many experiments addressing the quark-gluon structure of nucleons, whether it is (spin-dependent) deep-inelastic scattering or colliding relativistic heavy ions, jets of hadrons are produced as a result of strong interactions at the parton level. The process that leads from the partons produced in the elementary interaction to the hadron (jets) observed experimentally is referred to as hadronization or quark fragmentation.

It is of considerable importance to acquire a good understanding of the hadronization process, because it can be used to investigate the theory of the strong interaction, Quantum Chromodynamics (QCD), in the non-perturbative regime, and since it plays an important role in the interpretation of data from various experiments. Examples include the flavor decomposition of the nucleon spin, in which the hadron type observed in the experiment serves as a tag of the flavor of the struck quark [1], and studies of parton energy-loss mechanisms in nuclear matter [2], for which explicit QCD predictions exist.

According to most theoretical estimates the hadronization process occurs over length scales varying from a fraction of a femtometer to several tens of femtometers. At these length scales the strength of the strong coupling constant is such that perturbative techniques cannot be applied to evaluate the underlying interactions in a QCD framework. Hence, hadronization is an intrinsically non-perturbative QCD problem, for which only approximative theoretical approaches are presently available. In order to support these theoretical developments, experimental data are vital, since these can be used to gauge the available calculations.

The end-products of the hadronization process in free space are known from e^+e^- annihilation, but very little is known about the space/time development of the process. One way to investigate this is to study the semi-inclusive production of hadrons in deep-inelastic scattering of leptons (SIDIS) from nuclei. Lepto-production of hadrons has the virtue that the energy and momentum of the primordially produced parton are well determined, as it is 'tagged' by the scattered lepton. Employing nuclei of increasing size one can investigate the time-space development of hadronization, thus the nucleus is used as a *length (time)-scale probe* of the

underlying hadronization mechanism. If the hadronization is fast, i.e., the hadrons are produced at small distance scales compared to the typical fm-sizes of atomic nuclei, the relevant interactions in the nuclear environment involve well-known hadronic cross sections like the one between a pion and a nucleon (the pN interaction cross section). If - on the other hand - the hadronization is stretched out over many femtometers, the relevant interactions are partonic and involve the emission of gluons and quark-gluon interactions. These two extremes lead to different predictions for the loss in hadron yield (known as the *attenuation*) in nuclei as compared to that on free nucleons.

In practice, a combination of the two aforementioned mechanisms will probably contribute to the observed attenuation of hadron yields on atomic nuclei. Theoretically, this has led to a range of phenomenological approaches, which are partly summarized in the next section. The available calculations feature different assumed mechanisms (partonic energy-loss or hadronic absorption) and time scales (from less than 1 fm/c to more than 10 fm/c), which results in different dependences on the various kinematic variables. Hence, in order to distinguish between these calculations, precise hadron attenuation data need to be collected in a systematic approach involving a range of nuclei, several hadron types and measurements as a function of several kinematic variables. Such a comprehensive data set is presented in this thesis.

It goes beyond the scope of this work to compare the data to the (many) available theoretical calculations. Instead the data are evaluated so as to address two key issues in the study of hadronization: (i) which are the relevant time or length scales of the process, and (ii) what are the relevant mechanisms.

This thesis presents results for the multiplicities for pions, kaons, protons and antiprotons on Helium, Neon, Krypton and Xenon relative to Deuterium. Furthermore, the existing Krypton data for identified hadrons were reevaluated, the analysis now covering a wider kinematic range than in [3]. Thus by using a wide range of nuclei (from Helium to Xenon) the A-dependence of the attenuation process has been studied in detail for various hadron types.

The dissertation is organized as follows. In Chapter 1 the theoretical framework is described, and some of the available theoretical models are briefly summarized. First part of Chapter 2 contains introduction to the HERMES experimental set-up and description of the

detectors that are relevant to the present measurements, while in second part of the chapter, the data analysis is discussed, including a detailed presentation of the kinematical requirements used and corrections applied to the data. The results for R_A^h as a function of the various kinematical variables are presented and discussed in Chapter 3. This section has several subsections in which certain features of the data, especially those related to the relevant time scales and mechanisms, and the A dependence, are discussed separately.

The results are summarized in the last section, and some conclusions are formulated.

Chapter 1. Hadron Formation in Nuclear Medium

1.1 Inclusive Deep-Inelastic Scattering

1.1.1 Kinematic variables

In lepton-nucleon *Deep-Inelastic Scattering* (DIS), a high-energy lepton with momentum $\vec{k}$ and energy E emits a virtual photon of four-momentum q. The photon is then absorbed by a target nucleon of four-momentum p as shown in Fig. 1.1. The outgoing lepton with momentum $\vec{k}'$ and energy E' is detected under an angle θ.

The hadronic final state X produced by the fragmentation of the target nucleon has a total invariant mass denoted by W and a four-momentum p_X. If the hadrons produced in the final state are not differentiated, the type of reaction is called *inclusive*. The measurements of the incoming and outgoing lepton energy, E and E', and the scattering angle θ completely define the inclusive reaction.

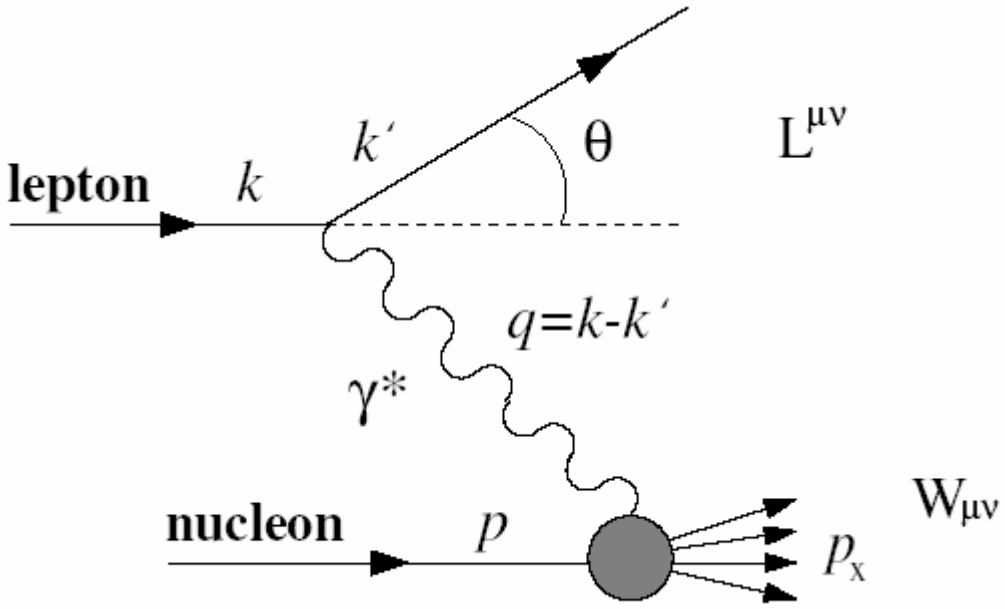

Figure 1.1: Deep inelastic lepton nucleon scattering diagram in lowest order QED.

With the four-momentum transfer in the scattering process, i.e. the four momentum of the virtual photon, given by $q \equiv k - k'$ the invariant variable Q^2 and the energy transfer are defined as:

$$Q^2 \equiv -q^{2lab} 4EE' \sin^2(q/2) \qquad (1.1)$$

$$n \equiv \frac{p \cdot q}{M}^{lab} = E - E' \qquad (1.2)$$

It is useful to introduce two dimensionless variables x and y, referred to as the Bjorken scaling variables, expressed by the equations:

$$x = \frac{Q^2}{2p \cdot q}^{lab} = \frac{Q^2}{2Mn} \qquad (1.3)$$

$$y = \frac{p \cdot q}{p \cdot k}^{lab} = \frac{u}{E} \qquad (1.4)$$

The energy transfer n in the laboratory (*lab*) system is constrained between zero and E, therefore the kinematic range of y is $0 \le y \le 1$. Since both Q^2 and u are positive, x has to be positive too. The other constraint on x comes from the invariant mass squared of the initial virtual photon nucleon system, which must be equal to or greater than the target nucleon mass square:

$$W^2 \equiv (p+q)^2 = M^2 + 2Mn - Q^2 \ge M^2 \qquad (1.5)$$

Using Eq. (1.3) this inequality gives $x \le 1$, therefore $0 \le x \le 1$. In the case of elastic scattering ($W^2 = M^2$) from Eq. (1.5) follows that $x = 1$.

For a fixed beam energy E (27.5 GeV at HERMES) the kinematics of inclusive DIS are determined completely by the measured variables (E', q). This pair of variables is usually converted into (n, Q^2). Figure 1.2 illustrates the allowed range of these deep-inelastic scattering variables for the HERMES experiment.

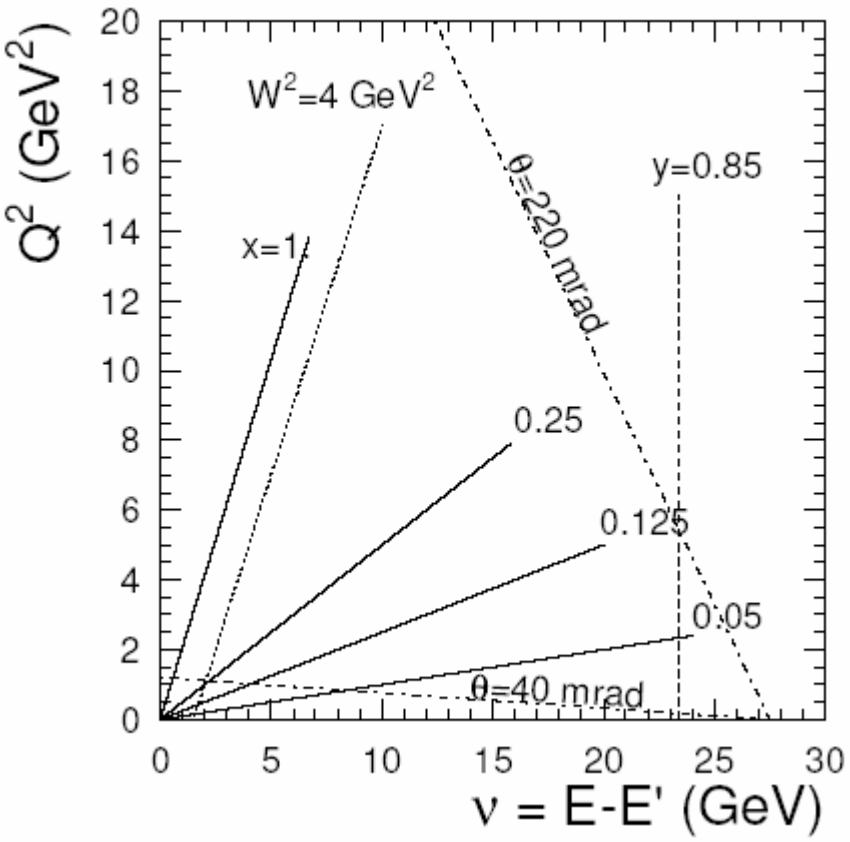

Figure 1.2: Kinematic plane of deep-inelastic scattering at E= 27.5 GeV. For given Q^2 and n values, all the other variables are defined. Lines of constant x ,q , W and y are shown.

The dash-dotted lines represent the geometrical boundaries of the detector acceptance. The dotted line at $W^2 = 4GeV^2$ sets the limit between the DIS and the nucleon resonance regions. The dashed line at y = 0.85 represents the cut used in the analyses presented in this thesis to exclude the kinematic region where QED radiative corrections become prohibitively large.

1.1.2 Unpolarized DIS cross section

A cross section is defined in order to describe the probability that a given scattering process is observed. For the photon exchange process illustrated in Fig. 1.1 the double differential cross section with respect to x and Q^2 is obtained by summing over all final states (including their spin) and averaging over the spin orientation of the initial particles [4],

$$\frac{d^2s}{dxdQ^2} = \frac{2pa^2}{(2ME)^2}\frac{1}{x^2Q^2}L^{mu}W_{mn} \qquad (1.6)$$

where $a = 1/137$ is the electromagnetic coupling constant. The leptonic tensor L^{mu} describes the leptonic vertex of the process, while the hadronic tensor W_{mn} carries information on the hadronic structure of the nucleon.

The hadronic tensor cannot be calculated from our knowledge of the incoming and outgoing fermions, as the hadron does not represent an elementary point-like particle, which is at the basis of the expression for the leptonic tensor. However, using symmetry arguments and QED conservation laws the hadronic tensor can be expressed in terms of four scalar functions depending on n and Q^2, which describe the electromagnetic structure of the nucleon. If the product is taken with the leptonic tensor, and the average over the incoming lepton helicity states is evaluated, the contributions of two out of these four structure functions vanish. By choosing to express W_{mn} in two dimensionless structure functions F_1 and F_2 the differential cross section is given by [4]:

$$\frac{d^2s}{dxdQ^2} = \frac{2pa^2}{Q^4}\left[F_1(Q^2,x)y^2 + \frac{F_2(Q^2,x)}{x}\left(1 - y - \frac{Mxy}{2E}\right)\right] \qquad (1.7)$$

Photo-absorption cross section

The optical theorem allows to extract the hadronic tensor W_{mn} for lepton nucleon scattering from the imaginary part of the hadronic tensor T_{mn} for Compton scattering using the relation $W_{mn} = \mathrm{Im}[T_{mn}]/2p$. A graphical expression of this theorem is shown in Fig. 1.3.

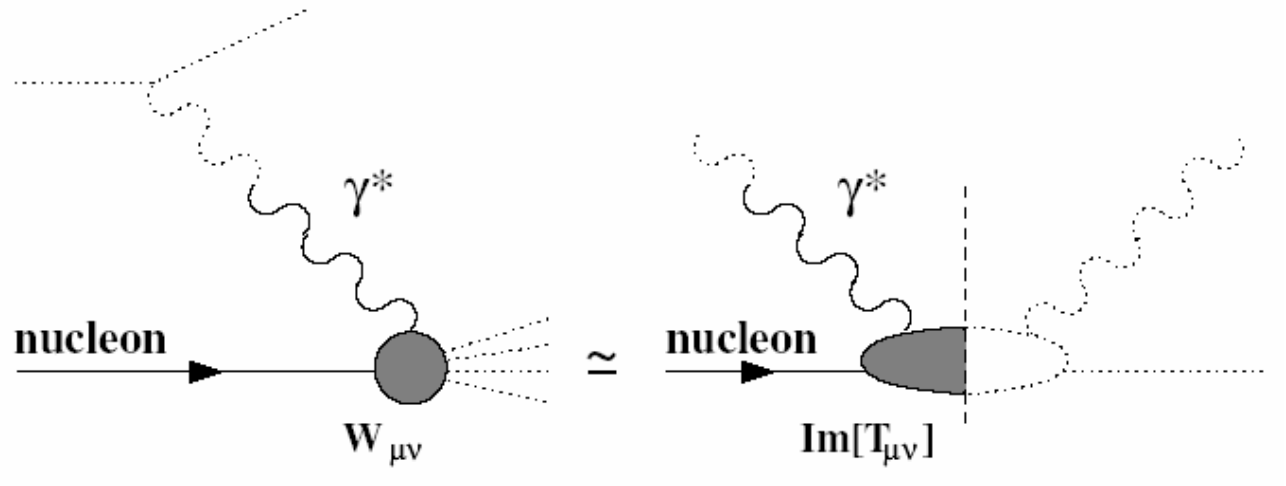

Figure 1.3: *Graphical representation of the optical theorem. The left diagram represents the DIS scattering process, the right one is the diagram for Compton scattering.*

When performing inclusive measurements the experimentally accessible quantity is in fact $\mathrm{Im}[T_{mn}]$. The cross section of Eq. (1.7) can alternatively be described in terms of absorption cross sections for longitudinally (s_L) and transversely (s_T) polarized photons:

$$\frac{d^2s}{dxdQ^2} = \Gamma(s_T(x,Q^2) + e s_L(x,Q^2)) \qquad (2.8)$$

where Γ describes the flux of virtual photons and their degree of polarization:

$$e = \frac{4(1-y) - \frac{Q^2}{E^2}}{4(1-y) + 2y^2 + \frac{Q^2}{E^2}} \qquad (2.9)$$

with e =0 corresponding to purely transverse polarization. Given the three possible photon polarization states

$$e_0^m = \frac{1}{\sqrt{Q^2}}(\sqrt{Q^2+n^2},0,0,n), \qquad e_\pm^m = \mp\frac{1}{\sqrt{2}}(0,1,\pm i,0) \qquad (1.10)$$

there are two spin-orientations of a target with spin $\pm\frac{1}{2}$ that contribute to the transverse cross section, and only one to the longitudinal:

$$s_T = \frac{1}{2}(s_{1/2}^T + s_{3/2}^T) = p(F_1 + g_1 - g^2 g_2) + p(F_1 - g_1 + g^2 g_2) = 2pF_1 \qquad (1.11)$$

$$s_L = s_{1/2}^L = 2p\,(-F_1 + \frac{(1+g^2)}{2x} F_2) \qquad (1.12)$$

with $g^2 = \frac{Q^2}{n^2}$, and g_1 and g_2 the spin-dependent structure functions. The labels of the two cross section components can be understood as follows. "Transverse" refers to $e_{\pm}^m$ (and $e = 0$), implying that the direction of the electric and magnetic fields are transverse to the direction of motion, as for the real photon case, while "Longitudinal" refers to e_0^m implying that the electric and magnetic fields are oscillating in the direction of motion.

From Eq. (1.11) one can see that $F_1(Q^2, x)$ represents the transverse component of the cross section (modulo a constant), while the longitudinal component is proportional to the structure function $F_L(Q^2, x)$ defined as:

$$F_L(Q^2, x) = (1+g^2)F_2(Q^2, x) - 2xF_1(Q^2, x) \qquad (2.13)$$

The structure function $F_2(Q^2, x)$ is a mixture of the transverse and longitudinal component. The ratio of longitudinal to transverse photo-absorption cross sections, R is given by

$$R(x, Q^2) = \frac{s_L}{s_T} = \frac{F_L(x, Q^2)}{2xF_1(x, Q^2)} \qquad (1.14)$$

$$= \frac{(1+g^2)F_2(x, Q^2)}{2xF_1(x, Q^2)} - 1 \qquad (1.15)$$

where Eq. (1.15) is obtained from Eq. (1.14) using the relation (1.13). From Eq. (1.15) the relation between the two structure functions F_1 and F_2 is seen to be given by $F_1 = \frac{(1+g^2)F_2}{2x(1+R)}$ which, when substituted in Eq. (1.7) gives the expression for the differential cross section as a function of F_2 and R:

$$\frac{d^2s}{dxdQ^2} = \frac{2pa^2}{Q^2} \frac{F_2(Q^2, x)}{x} \left(\frac{1 + eR(x, Q^2)}{1 + R(x, Q^2)} \right) \qquad (1.16)$$

1.1.3 Quark Parton Model

The *Quark Parton Model* (QPM) is used to describe the absorption of the virtual photon with the nucleon constituents. The quarks (partons) are assumed to be point-like particles carrying spin $\frac{1}{2}$. In the Bjorken limit of Q^2 and n going simultaneously to infinity the structure functions and can be expressed as

$$F_2(x) = \sum_f e_f^2 x q_f(x) \qquad (1.17)$$

$$F_1(x) = \frac{1}{2x} F_2(x) \qquad (1.18)$$

with $q_f(x)$ the momentum distribution of a quark of flavor f and e_f the quark charge in units of electron charge. Eq. (1.18) is known as the Callan-Gross relation. In the QPM the structure functions are only dependent on the dimensionless variable *x*, which is interpreted as the fractional momentum carried by the struck parton. Increasing the spatial resolution of the scattering process by increasing Q^2 leaves the structure function unchanged, since the quarks in the QPM are assumed to be point-like.

This Bjorken scaling behavior has been confirmed experimentally in good approximation. Scaling violations are, however, observed for large and small values of Q^2, where $F_2(x)$ becomes Q^2 dependent.

In the QPM a value for R can be derived. Substituting the Callan-Gross relation into Eq. (1.15), it can be noted that in the Bjorken limit the structure function R goes to zero:

$$R = \frac{s_L}{s_T} \rightarrow \frac{F_2 - 2xF_1}{2xF_1} = 0 \qquad (1.19)$$

The fact that R vanishes in the QPM can be traced to the spin $\frac{1}{2}$ character of the partons.

1.2 Semi-Inclusive Deep-Inelastic Scattering

In the previous section inclusive reactions have been considered where the only particle detected is the scattered lepton. If in addition to the scattered lepton also one of the produced hadrons is identified the event is called *semi-inclusive*. A schematic representation of a semi-inclusive event in lowest order QED is given in Fig. 1.4.

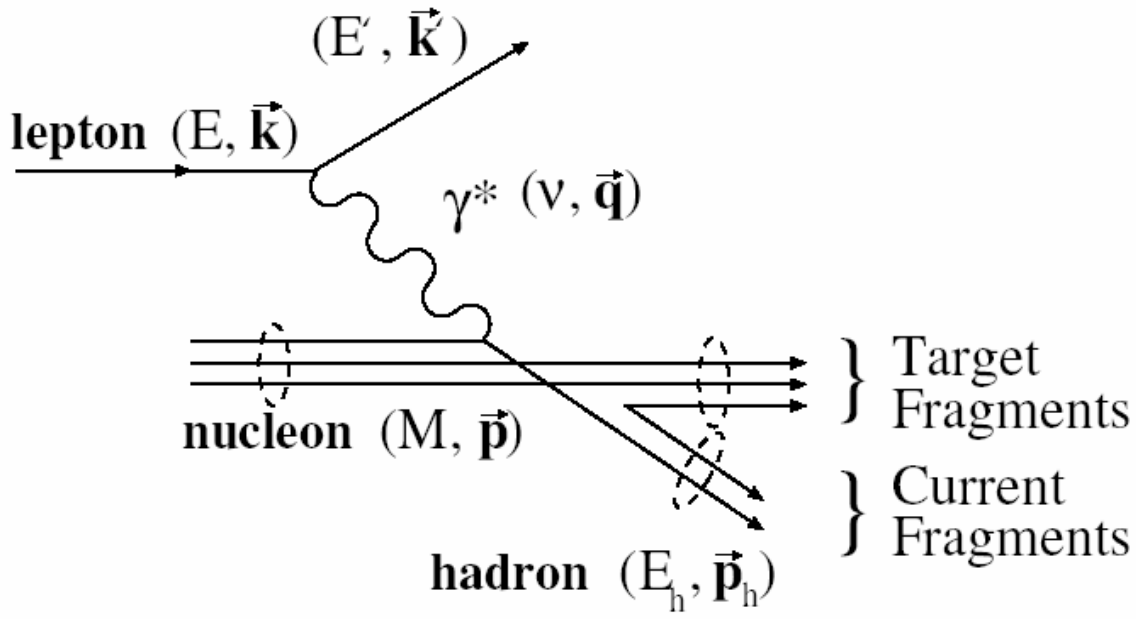

Figure 1.4: Semi inclusive deep-inelastic lepton nucleon scattering diagram in lowest order QED.

The hadron carries information on the flavor of the struck quark. The flavor dependence of *Semi-Inclusive Deep-Inelastic Scattering* (SIDIS) can only be exploited for hadrons originating from struck quarks. These so-called *current fragments* must be separated from the ones originating from the target remnants (*target fragments*). The separation between the current and target fragmentation domains is accomplished by imposing requirements on the kinematics of the detected hadrons, e.g. by requiring that the hadrons are relatively fast in the laboratory frame. For this purpose a lower limit is set on the fractional energy transferred from the virtual photon to the hadron, $z = E_h / n$.

The separation between current and target fragmentation can also be based on the Feynman

scaling variable $x_F = p_{\parallel}^h$ with $p_{\parallel}^h$ the component of $\vec{p}_h$ parallel to the direction of the virtual photon. In general the requirement $x_F > 0$ selects the current fragmentation domain.

1.2.1 Semi-Inclusive DIS cross-section

In semi-inclusive deep-inelastic scattering it is assumed that the timescale for the absorption of a virtual photon is very short as compared to the timescale needed for the quark to fragment into a hadron. The fragmentation process is not calculable in pQCD since it involves long distance processes, and thus corresponds to very low Q^2 values where pQCD techniques cannot be used. Therefore, the fragmentation process in semi-inclusive scattering is parameterized by fragmentation functions $D_f^h(Q^2, z)$, which represent the probability that a quark of flavor f fragments in a hadron of type h with a fraction z of the virtual photon energy $E_h = z\nu$. The kinematic dependence of the fragmentation function involves only Q^2, which represents the effect arising from gluon radiation of the struck quark.

In the QPM the cross section for the process $eN \to ehX$ is assumed to be the product of the differential inclusive cross section, already presented in Eq. (1.7), and the fragmentation probability to find a hadron originating from a quark of any flavor f.

$$\frac{d^3\sigma(eN \to ehX)}{dxdQ^2dz} = \frac{d^2\sigma(eN \to eX)}{dxdQ^2} \frac{\sum_f e_f^2 q_f(x,Q^2) D_f^h(Q^2,z)}{\sum_f e_f^2 q_f(x,Q^2)} \qquad (1.20)$$

Here it is assumed that the quasi-free scattering process (related to the quark momentum distribution $q_f(x)$) and the fragmentation process (described by the fragmentation function $D_f^h(z)$) enter as two independent factors in the cross section (at the flavor level). This is known as *factorization.* From Eq. (1.20) the hadron multiplicity per DIS event is obtained:

$$M_h(Q^2,z) \equiv \frac{1}{\sigma}\frac{d^2\sigma(eN \to ehX)}{dQ^2dz} = \frac{\int dx \sum_f e_f^2 q_f(x,Q^2) D_f^h(Q^2,z)}{\int dx \sum_f e_f^2 q_f(x,Q^2)} \qquad (1.21)$$

where σ represents the differential inclusive DIS cross section $\frac{d^2\sigma(eN \to eX)}{dxdQ^2}$.

1.3 Theoretical Issues and Motivation

The aim of this work is the study of the hadronization process in a nuclear environment. For this purpose the multiplicity ratio R_A^h as experimentally measurable observable is used. The ratio R_A^h depends on the leptonic variables n and Q^2, where $n = E - E'$ and $-Q^2 = q^2 = (k - k')^2$, which are the energy transfer in the target rest frame and the squared four-momentum of the virtual photon, respectively, and on the hadronic variables $z = E_h / n$, the fraction of the virtual photon energy carried by the hadron, and p_t^2, the square of the hadron momentum component transverse to the virtual photon direction. It is defined as the ratio of the differential multiplicity on nucleus *A* to that on deuterium, i.e., it is the ratio of the number of hadrons *h* produced per Deep-Inelastic Scattering (DIS) event on a nuclear target with mass number *A* over that for a deuterium (*D*) target:

$$R_A^h(n, Q^2, z, p_t^2) = \frac{\left(\frac{N^h(n, Q^2, z, p_t^2)}{N^e(n, Q^2)} \right)_A}{\left(\frac{N^h(n, Q^2, z, p_t^2)}{N^e(n, Q^2)} \right)_D} \qquad (1.22)$$

with $N^h(n, Q^2, z, p_t^2)$ is the number of semi-inclusive hadrons in a given (n, Q^2, z, p_t^2)-bin, and $N^e(n, Q^2)$ the number of inclusive DIS positrons in the same n, Q^2-bin. Implicit in this definition is integration over the angle j between the lepton scattering plane and the hadron production plane (see Fig.1.1.1).

Figure 1.5 once again illustrates the definition of the relevant lepton and hadron kinematic variables thoroughly described in previous section. In the absence of nuclear effects R_A^h=1, and experimental results show that this is the case at high energy transfer n [5, 6]. At lower values of n the value of R_A^h has been found to be less than unity [3, 7, 8].

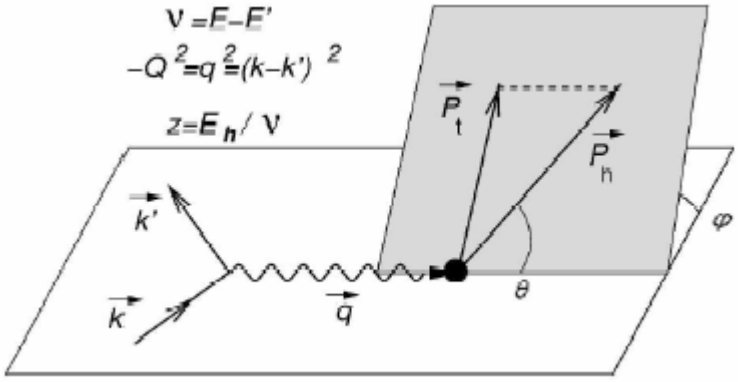

Figure 1.5 Kinematic plane for hadron production in semi-inclusive deep-inelastic scattering and definitions of the relevant leptonic and hadronic variables.

Even if hadronization is not yet quantitatively understood, it is known that the following processes play a role in leptoproduction of hadrons. After a quark in a nucleon is hit by the virtual photon it looses energy by scattering from other quarks and radiating gluons, thus creating quark-antiquark pairs. At some time (colorless) hadrons are formed. Here one can discriminate between the time t_c (and corresponding (constituent) length l_c) that a so-called pre-hadron is formed, and the time t_h that the final physical hadron is formed.*

The (average) length l_c has been estimated [9] based on the Lund model as:

$$l_c = \frac{\ln(1/z^2) - 1 + z^2}{1 - z^2} \times \frac{zn}{k} \qquad (1.23)$$

where k is a non-perturbative scale in the order of the string tension, usually taken as k=1.0 GeV/fm.

According to this formula the average value of l_c goes as $1-z$ for large values of z, and has a broad maximum around z=0.3. Thus at values of n of *5-20* GeV, the hadronization process takes

* In the literature sometimes the name "formation time or length" has different meanings, and also di symbols are used. We will use the name 'formation length' (l_c) for what is often called the pre-hadı constituent) formation length, and "hadron formation length" (l_h) for the hadron (or yo-yo) formation (see e.g. [8, 9]).

place over distances of *1-10* fm, comparable to the size of a nucleus. If the (pre-)hadron is formed inside the nucleus, it can experience so-called final-state interactions in the nucleus, through which it can be absorbed or can produce other (lower energy) hadrons. Thus the use of a nuclear target allows to probe the space-time development of the hadronization process.

At present reliable calculations within Quantum Chromo Dynamics (QCD) of quark hadronization (fragmentation) can not yet be performed because of the major role of 'soft' processes. For that reason various types of models have been developed.

Phenomenological models [10, 11, 12, 13, 14] use formation times/lengths and absorption cross sections of the various hadrons in the nuclear medium. Different formula's for the formation lengths have been used, and in the more advanced versions two lengths scales (l_c and l_h) are distinguished, as well as absorption cross sections for both the quark, the prehadron and the final hadron. The absorption cross sections are usually fitted to obtain the best description of the n - and z-dependence of the experimental data.

Other (QCD inspired) models focus on the energy loss that the hit quark experiences in the nuclear environment [2,15-19]. In [19], twist-4 contributions to the fragmentation functions resulting from multiple scattering and gluon bremsstrahlung in a nuclear medium are calculated. A nuclear attenuation proportional to $A^{2/3}$ is predicted, where the power *2/3* results from the coherence of the gluon radiation process [20], which gives an induced radiative energy loss of a quark traversing a length L of matter proportional to L^2. No hadron absorption is included, as it is assumed that hadronization takes place outside the nucleus.

The effect of a finite formation length l_c is included in [17], in which medium modified fragmentation functions due to partonic energy loss via gluon emission during the time t_f are calculated. Using the quark energy loss determined from Drell-Yan data production, good agreement is found for various hadron species and nuclei. In order to keep the approach as simple as possible, absorption of the produced (pre)hadron is not taken into account.

Another class of models include (pre)hadron absorption, with or without some description of what happens in the hadronization process. In [21] R_A is described in terms of medium modified

fragmentation functions supplemented by nuclear absorption. A rescaling model that also has been used to describe the EMC effect is used to describe the nuclear modification of the fragmentation functions. The (average) formation length is taken from the Lund model [22] [23] calculates the nuclear attenuation of the (leading) hadron with $z>0.5$ by including as major ingredients the (distribution of the) formation length l_c and an absorption cross section of the pre-hadron. The effect of quark energy loss is found to be small.

In [24] the hadron attenuation is investigated within the framework of the Boltzmann-Uehling-Uhlenbeck (BUU) transport model. Since this is a coupled-channels approach, hadrons are not only absorbed, but can also be produced (mainly at low values of z). Some choices, including taking it zero, for the formation time t_c are studied.

An intriguing observation is that all models, notwithstanding their different and sometimes orthogonal ingredients, are able to give a fair and sometimes even good description of the available data. One obvious reason for this is that the decreasing attenuation with increasing value of n is largely due to a simple increase of the formation time t_c with n in the target rest frame due to Lorentz dilatation. In this respect the dependence of R_A on z and A will be more discriminating.

Since the A-dependence is an important ingredient, some remarks should be made about the A-dependence expected for the various mechanisms. As already mentioned the attenuation in the energy-loss model of [25] is given as $1-R_A \sim L^2 \sim A^{2/3}$, whereas in (Glauber type) absorption models it is often presumed that $1-R_A \sim L \sim A^{1/3}$. However, these estimates are too simple. First of all taking $L \sim A^{1/3}$ assumes the nucleus to be a rigid sphere or of Gaussian shape, which is not a good approximation. Taking a realistic model for the matter distribution of a nucleus yields values [26] for $\langle (rl)^2 \rangle$, where r is the density, that globally follow an $A^{0.74}$ form. And it is found that $\langle rl \rangle$ is globall0y proportional to $A^{0.4}$. In addition it has been demonstrated in ref.~\cite{accardi} that inclusion of a distribution for the formation length l_c in absorption calculations increases the exponent, yielding values (for a nucleus described as a rigid sphere) for $1-R_A$ that approximately

follow an $A^{2/3}$ pattern for large values of l_c. Using a realistic matter distribution one finds for l_c =4 fm an $A^{0.6}$ behavior [26].

Thus, in order to disentangle between different models and in particular to have a sensitive probe for energy loss, formation time and absorption effects, detailed data for a wide range in mass number are needed. For these reasons HERMES has taken many more data to extend the available database, the results of which are discussed in the next sections.

Chapter 2. The HERMES Experiment

The **HERMES** experiment **HER**A **ME**asurement of **S**pin is a second generation polarized deep inelastic scattering (DIS) experiment to study the spin structure of the nucleon. It is being run at the HERA storage ring at DESY.

Several experiments over the last decade have provided accurate data on the polarization asymmetry of the cross-section for inclusive scattering where only the scattered lepton is detected. These experiments have been interpreted as showing that at most 30 % of the nucleon spin comes from the spins of the quarks. Further knowledge of the origin of the nucleon's spin can be gained by studying *semi-inclusive* processes involving the detection of hadrons in coincidence with the scattered lepton. These data offer a means of `flavor-tagging' the struck quark to help isolate the contributions to the nucleon spin of the individual quark flavors, including the sea quarks. The interpretation of semi-inclusive data is made clearer if the type of hadron is identified. This is a central theme of the HERMES experiment, which can identify hadrons with very high level of accuracy in a wide kinematic range.

The physics program for HERMES is very broad. The experiment contributes inclusive data with qualitatively different systematic uncertainties to improve the world data set for the x dependence and the integral of the spin structure function $g_1(x)$ for both the proton and the neutron. HERMES is also providing new precise data on semi-inclusive processes by virtue of the good acceptance of the spectrometer combined with hadron identification and the purity of the targets.

The HERA storage ring can be filled with either electrons or positrons, which are accelerated to 27.5~GeV. Positrons have been used since 1995 because longer beam lifetimes are then possible. Since with few exceptions such as the luminosity measurement, the physics processes are the same for positrons and electrons, the term ``positron'' will be used for both in this paper.

In addition to studying polarised DIS using $\overline{H}$, $\overline{D}$, and $^3\overline{He}$ targets, data are collected with unpolarised gases (H_2, D_2, ^{3}He, N_2). This provides in a relatively short period of time (2-3 weeks) high statistics data sets that are used to study important properties of the nucleon not related to spin, such as the flavour asymmetry of the sea, as well as hadronisation in nuclei, which is what this work has been aimed at.

The Hermes [27] experiment utilizes the longitudinally polarised positron (or electron) beam of the Hera accelerator in combination with a polarised internal gas target of hydrogen, deuterium or ^{3}He for the measurement of polarised deep inelastic scattering.

The experiment is located in the East Hall of the Hera accelerator at Desy in Hamburg, Germany. The Hera accelerator consists of positron and proton storage rings with 27.5 GeV and 820 GeV respectively. There are three other experiments at Hera, the two collider experiments Zeus and H1, and Hera B which uses only the proton beam. Figure 2.1 shows a schematic overview of the Hera positron ring indicating the direction of the beam polarization by arrows.

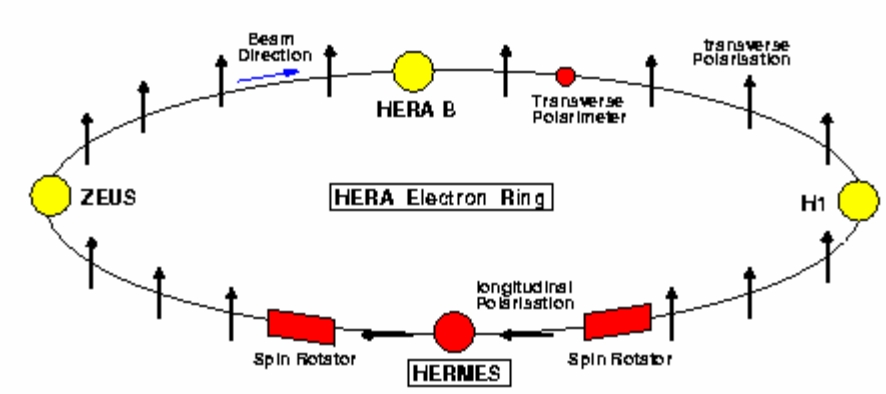

Figure 2.1: Schematic overview of HERA with the four experiments, the beam polarimeter and the spin rotators at the Hermes experiment.

2.1 The Hermes Spectrometer

2.1.1 General Description

The HERMES experiment is located in the East hall of the HERA storage ring complex at DESY. The spectrometer is a forward angle instrument of conventional design. It is symmetric about a central, horizontal shielding plate in the magnet. Due to this symmetry, the description of the detectors contained in this paper will apply typically to only one half of the spectrometer, in particular with respect to the number of detectors quoted and their dimensions. A diagram of the spectrometer is shown in Fig. 2.2. The coordinate system used by HERMES has the z axis along the beam momentum, the y axis vertical upwards, and the x axis horizontal, pointing towards the outside of the ring. The polar (J) and azimuthal (j) scattering angles as well as the initial trajectory for the determination of the particle's momentum are measured by the front tracking system, which consists of drift chambers (DVC, FC1/2). The momentum measurement is completed by two sets of drift chambers behind the magnet (BC1/2 and BC3/4). In addition, there are three proportional chambers in the magnet (MC1/3) to help match front and back tracks as well as to track low momentum particles that do not reach the rear section of the spectrometer.

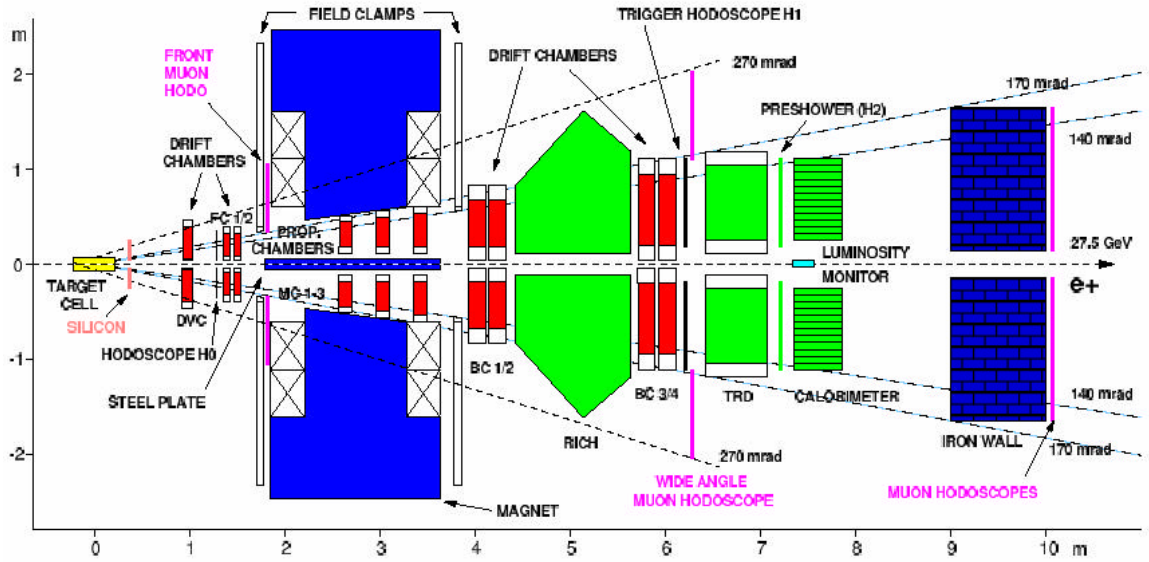

Figure 2.2: Schematic side view of the Hermes spectrometer

Particle identification (PID) is provided by a lead-glass calorimeter, a pre-shower detector (H2) consisting of two radiation lengths of lead followed by a plastic scintillator hodoscope, a transition radiation detector (TRD) consisting of six identical modules, and a Ring Imaging Cerenkov detector (RICH). The particle identification system was designed to provide a hadron rejection factor of 10^4 to yield a very clean DIS positron sample, and exceeds this in practice. Pion and Kaon identification is provided by RICH. The calorimeter and pre-shower detector are included in the trigger along with a second hodoscope (H1) placed in front of the TRD. An additional trigger hodoscope (H0) was included in 1996 in front of FC1 to reduce the trigger rate from background caused by the proton beam.

The acceptance is limited at small angles by an iron plate in the beam plane, which shields the positron and proton beams from the magnetic field of the spectrometer magnet. Both beams go through the spectrometer, separated by 72 cm. Particles with scattering angles within ± 170 mrad in the horizontal direction and between +(-)40 mrad and +(-)140 mrad in the vertical direction are accepted. Therefore, the range of scattering angles is 40~mrad to 220~mrad. The x Bjorken (see (1.3)) range covered by the HERMES experiment is 0.02-1.0, although there is little count rate for $x \geq 0.8$ when W $\leq$ 2 GeV (W is the photon-nucleon invariant mass, see (1.5)). All details, related to Hermes spectrometer could be found in [28].

The experiment is mounted on a large platform that can move on rails together with an attached trailer (ET) containing the electronics and the gas systems. A fixed but removable concrete wall between the platform and the ET shields the main part of the hall from radiation and hence allows access to the electronics while the accelerators are running. Cables and gas pipes between the detectors and the ET are routed beneath the platform to a large cable tray passing under the shielding wall. The experiment was assembled in the East hall outside the shielding during the 1994 HERA run. After the shielding wall had been dismantled, the platform/trailer was moved into place in the ring. The shielding wall was re-erected between the platform and the electronics trailer in such a way that the experiment could be moved far enough within the shielding to allow the HERA maintenance tram access to the tunnel on 24 hours notice.

2.1.2 The Target Region

The HERMES target consists of an open ended storage cell [29] internal to the HERA positron ring. Using an *Unpolarized Gas Feed System* (UGFS) it is possible to deliver ${}^{1}H, {}^{2}H, {}^{4}He, {}^{14}N, {}^{20}Ne$ and ${}^{84}Kr$ gases with total areal densities between 10^{15} and 10^{16} $nucl/cm^2$ to the storage cell. The pressure in the UGFS is regulated via a diaphragm and a termo-valve in order to supply a constant density to the cell. The low rate through the diaphragm can be measured with two barometers, by the pressure dependence of the diaphragm conductance.

From the low rate the target density for each gas can be evaluated given the cell conductance. Unfortunately this method gives an uncertainty on the absolute value of the target density of about 20%, mostly due to the uncertainty on the diaphragm and the cell conductances [30].

2.1.3 The Magnet

The HERMES spectrometer magnet is of the H-type with field clamps in front as well as behind in order to reduce the fringe fields at the position of the drift chambers FC2 and BC1. A massive iron plate in the symmetry plane shields the positron and proton beams as they pass through the magnet.

The most important features of the magnet are:

- It is capable of providing a deflecting power of $\int Bdl$ = 1.5~Tm , although it is operated at 1.3 Tm to reduce power consumption. The smaller field integral does not significantly impair the performance of the spectrometer. The variation of the deflecting power within the acceptance is less than 10 %.
- The gap between the pole faces encloses the geometrical acceptance of $\pm(40.140)$ mrad in the vertical direction. In the horizontal direction ± 170 mrad plus another ± 100 mrad starting halfway through the magnet is provided. The pole faces are tilted parallel to the limits of the vertical angular acceptance. Due to the limited space of 8.5 m for the HERMES spectrometer between the

center of the target and the first quadrupole magnet of the electron machine, only 2.2 m between the drift chambers FC2 on the front and BC1 on the rear side are utilized for the magnet.

- The fringe field at the positions of the adjacent drift chambers does not exceed 0.1 T.
- An effective magnetic shielding substantially reduces the effect of the magnet on the proton and positron beams. In particular, the sextupole moment of the magnetic field in the beam tubes is minimized.
- A correction coil with a deflecting power of 0.08~Tm is accommodated Inside the shielding of the positron beam pipe. This coil is used to correct for fringe fields and the imperfections of the magnetic shielding in this section of the iron plate. It is also intended to compensate the transverse holding field of the target when operating with transverse polarization. It serves as an element of a closed orbit bump with no net global effect on the positron beam.

The field measurements were done with a 3D-Hall probe on an automated 3D-mapping machine. The results exhibit an overall reproducibility of about 10^{-3}, and a field pattern as expected. No homogeneous regions are found due to the high gap to length ratio of the magnet, and a pronounced step in the field is observed that reflects the structure of the iron shielding plate. The detailed field map was integrated into the track reconstruction algorithm, as described later.

2.1.4 The Tracking System

The tracking system serves several functions, which vary somewhat in their performance requirements:

- Determine the event vertex in the target cell to ensure that reconstructed events come only from the sub-mm beam envelope in the target gas, with the expected z-distribution. Also, the analysis of events with multiple tracks requires either a common vertex, or possibly an additional displaced vertex for a reconstructed particle decay.
- Measure the scattering angles for kinematic reconstruction.
- Measure the particle momentum from the track deflection in the spectrometer dipole magnet.
- Identify the hits in the PID detectors associated with each track.

When all tracking detectors are fully operational, the momentum resolution for positrons is limited by Bremsstrahlung in the material of the target cell walls, the 0.3~mm thick stainless steel vacuum window, as well as the first tracking detectors.

The locations of the tracking detectors are shown in Fig. 2.8, the detailed Table which summarizes their properties can be found in [28]. The drift vertex chambers DVC's and the front drift chambers FC1/2 provide both vertex reconstruction to the target, and definition of the scattering angle. In conjunction with the front tracking, the back drift chambers BC1/2 and BC3/4 measure the magnetic deflection and hence the momentum. The BC's also identify the cells in the PID detectors associated with each track. The proportional chambers inside the magnet (MC1/3) were originally intended to ensure that multi-track ambiguities could be resolved. As it happens, chamber occupancies are low enough that this can be accomplished using the drift chambers alone. However, the MC's are found to be very useful for momentum analysis of low energy decay products that are deflected too much to reach the downstream tracking detectors. Since 2001 the silicon detector with the name Lambda Wheels (LW) was installed eight after the target cell (see Fig. 2.2). The aim was to increase the detector acceptance and in particular to augment by a factor of four the yield of reconstructed Lambda hyperons.

Like the rest of the spectrometer, the tracking system is symmetric about the beam plane.

The Drift Chambers

The drift chambers DVC, FC1/2, BC1/2 and BC3/4 are of the conventional horizontal-drift type. Each layer of drift cells consists of a plane of alternating anode and cathode wires between a pair of cathode foils. The cathode wires and foils are at negative high voltage with the anode sense wires at ground potential. The chambers are assembled as modules consisting of six such drift cell layers in three coordinate doublets (UU', XX' and VV'). The wires are vertical for the X planes and at an angle of $\pm 30^0$ to the vertical for the U and V planes. The X', U' and V' planes are staggered with respect to their partners by half the cell size in order to help resolve left-right ambiguities. Each sense plane consists of a fiberglass-epoxy frame laminated to a printed circuit board (PCB) that has solder pads for the wires. Except in the case of the DVC's, the PCB's carry the traces leading past O-ring gas seals to external connectors. The opposite ends of the cathode wires

connect to internal distribution buses for the negative high voltage. Each module is enclosed between metallized Mylar gas windows mounted on metal frames. Identical modules are situated above and below the beam pipe.

The frames of all the drift chambers except the DVC's have sufficient length to allow both ends of all wires in the U and V planes to terminate on the long edges of the frames. Hence all U and V wires and their PCB traces have the same length and similar capacitance. The onboard electronics are mounted along only the one long edge opposite to the beam pipes. The choice of gas mixture for the drift chambers was governed by the serious inconvenience of controlling the hazards of a flammable gas in a tunnel environment. As well, there is an advantage in limiting the drift cell occupation time and hence the number of extraneous hits that must be accommodated in track finding.

The DC readout system consists of Amplifier/Shaper/Discriminator (ASD) cards mounted onboard the drift chambers, driving ECL signals on 30 m long flat cables to LeCroy 1877 Multihit FastBus TDC's in the external electronics trailer. The design goal (especially in the case of the FC's and DVC's) was chamber operation at low gas gain ($\approx 10^4$) to maximize chamber lifetime and reduce particle flux dependence of the gas gain due to space charge effects. To combine this goal with good spatial resolution requires operation at low threshold -- well below 10^5 electrons from the wire.

The Magnet Chambers

The proportional wire chambers MC1 through MC3 located in the gap of the magnet were originally intended to help resolve multiple tracks in case of high multiplicity events. Since low backgrounds have made this unnecessary, their primary function is now the momentum analysis of relatively low energy particles, from the decay of Λ's for example. Since the MC's operate in a strong magnetic field and resolution of ± 1 mm is sufficient, multi-wire proportional chambers with digital single bit-per-wire readout were chosen. The magnet has a tapered pole configuration that implies a different size for each pair of chambers. The active areas of the three chambers are dictated by the spectrometer acceptance together with magnetic dispersion at a nominal trigger threshold positron energy of 3.5 GeV.

The MC system performed reliably with typical efficiency per plane of 98-99 %. Electronics failures in the 1996-97 running period resulted in the loss of only 0.5 % of the channels (3 of 688 cards).

The contribution to the spectrometer momentum resolution for 10 GeV positrons by Coulomb multiple scattering in the magnet chambers and air between FC2 and BC1/2 is J_{rms} = 0.15 mrad. (If the air were replaced by helium, it would be decreased to 0.11 mrad.) Thus the ratio of J_{rms} to the magnet deflection angle is equal to 0.0024, independent of energy. This is small compared to other contributions.

Alignment

Errors in the relative alignment of the various elements of the tracking system are an important contribution to the resolution in reconstructed kinematic quantities. The initial alignment during detector installation was done using conventional optical techniques, but difficulties with optical access to the components limited the expected accuracy of this process to a few hundred micrometers in x and y, and of order 1~mm in z. It was always expected that the relative detector alignment would have to be improved in the data analysis through the study of track residuals with the spectrometer magnet turned off. This procedure was refined over the first three years of operation to the point that drift chamber alignment errors are no longer a major contribution to tracking resolution.

It was considered essential to have a means to continuously monitor the relative alignment of the tracking detectors for two reasons. First, the detectors are mounted on a complex support system that is not simply interconnected so that its response to temperature changes and gradients is difficult to predict. Also, the front detectors are supported ultimately via the spectrometer magnet field clamp, which might suffer distortion from magnetic forces. Such an effect was detected with this monitoring system, and eliminated by stabilizing the clamp mount. Secondly, if a detector must be replaced with a spare after the laborious alignment analysis has been done, it is desirable to be able to avoid having to repeat this process immediately with new field-off data.

A solution to both of these problems is to have on each detector module optical targets that are continuously accessible to a remotely operated image recording system. The type of system that was chosen employs two well-collimated parallel laser beams passing through the entire spectrometer in the beam plane, on either side of and parallel to the beam axis. The 2~cm diameter beams are created by one He-Ne laser and a semi-transparent mirror. Two optical target assemblies are mounted precisely and reproducibly on each detector element. Each assembly includes a remotely-controlled actuator that can move an optical target into the path of a laser beam, arriving at a precise and reproducible stop. Only one target is in a laser beam at a time. The type of target used -- the Fresnel zone plate -- is similar to that used in the SLAC accelerator alignment monitoring system. It is made by etching a precise pattern through a thin metal foil. This avoids any deflection of the beam from imperfections in the planarity of transparent material.

Track Reconstruction

The HERMES reconstruction program (HRC) is very efficient because it makes use of two unusual methods: the tree-search algorithm for fast track finding and a look-up table for fast momentum determination of the tracks. The full reconstruction of 30 Monte Carlo events on HERMES PCFarm takes only one second.

The main task of the reconstruction program is to identify particle tracks using the hits in the tracking chambers. Each detector plane gives spatial information in one coordinate, and only by combining the information of many detectors is it possible to reconstruct the tracks uniquely in space. At each step of the iteration the entire partial track is seen. However only at the end is the full detector resolution reached. The detector resolution is roughly 250 mm and the active width of a chamber is of the order of a few meters. Therefore after about 14 steps in the binary tree, the resolution of the detector of $\approx 1{:}2^{14}$ would be reached. For the purpose of track finding (not fitting) a resolution of $1{:}2^{11}$ is sufficient, which reduces the maximum number of iterations in the HRC tree-search to about 11.

The number of allowed track patterns at the full resolution is of the order of 10^8. Without optimization, this large number would make the algorithm useless for two reasons: memory space

problems to store all the patterns, and CPU time problems to compare with each of them. The following methods avoid these problems: if one compares the allowed patterns from one iteration to those from the following one (called parent and child in the following) it becomes obvious that only a very limited number of children exist for each parent. At initialization time all links between the allowed patterns of each generation are calculated, i.e. all children for each parent are stored in the data base. The number of comparisons now becomes small: if a pattern is recognized at one generation, only its children have to be checked in the next generation. The number of children for each parent is typically 4 to 8. This solves the CPU problem.

Symmetry considerations can be used to reduce the number of patterns that have to be stored. If two patterns are mirror symmetric, or if they are identical except for a transverse shift, they are stored as one pattern. Most important is that if a child is identical to aparent, then the child is linked to the parent and all grand children become identical to the children. This simplification is based on the fact that we are looking only for approximately straight tracks. This reduces the number of branches in the tree-search significantly. The number of patterns in the data base is of the order of 50,000, which is small compared to the original number of 10^8.

As a second feature in HRC, a very fast method has been developed to determine the momentum of a track, which is given by the deflection in the inhomogeneous field of the spectrometer magnet. Tracking through a magnetic field is very CPU intensive. The new method makes obsolete the tracking through the magnetic field on a track by track basis. Instead, a large look-up table is generated only once during initialization. It contains the momentum of a given track as a function of the track parameters in front of and behind the magnet. The relevant track parameters are the position and the slope of the track in front of the magnet and the horizontal slope behind the magnet. The resolution of the table has been chosen such that, using interpolation methods, the contribution by HRC to the precision of the track momentum determination is better than $\Delta p/p=0.5$ %. The look-up table contains 520,000 numbers. This method of momentum determination is extremely efficient.

Tracking system performance

The performance of the tracking system has been studied using the detailed HERMES Monte Carlo (HMC) simulation of the experiment, which is based on the GEANT software package. Resolutions for several quantities were estimated by performing a Gaussian fit to spectra of the difference between the generated and reconstructed quantities. Results for the measured quantities p (momentum) and J (scattering angle) are shown in Figs. 2.11 and, 2.12. The momentum resolution is 0.7-1.25 % over the kinematic range of the experiment, while the uncertainty in the scattering angle is below 0.6 mrad everywhere. Bremsstrahlung in materials in the positron path cause the momentum resolution function to have a standard deviation considerably larger than that of the fitted Gaussian.

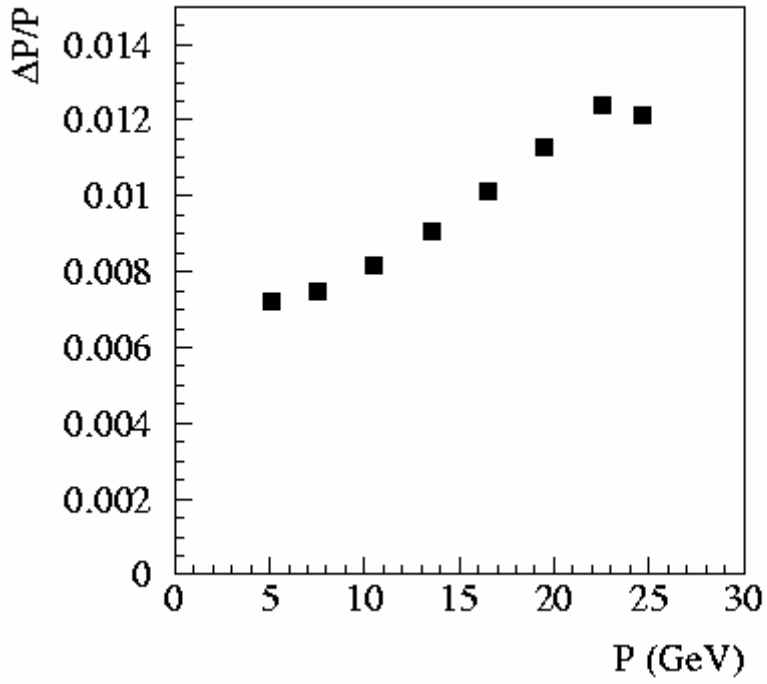

Figure 2.11: Momentum resolution, deduced from Monte Carlo studies

The x resolution varies from 4 % to 8 % while the Q^2 resolution is better than 2 % over most of the kinematic range.

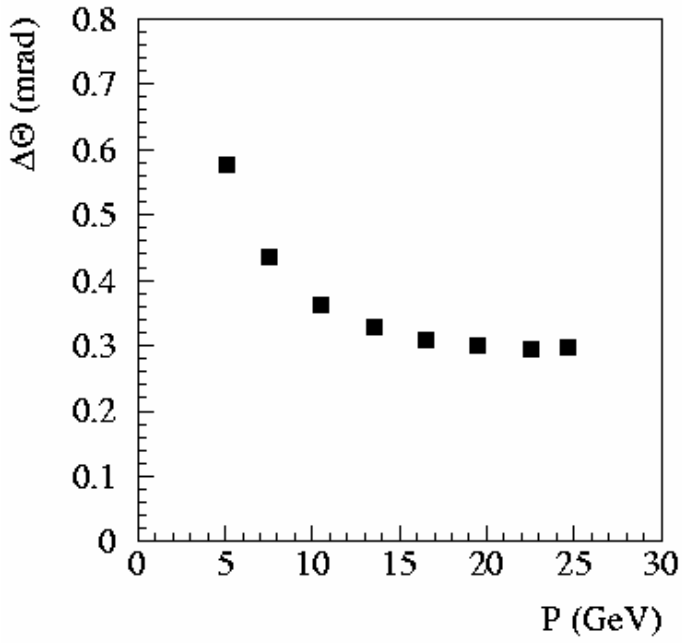

Figure 2.12: Resolution in scattering angle, deduced from Monte Carlo studies

Finally, the absolute calibration of the spectrometer can be checked using the decay of K_S mesons into two pions. The invariant two-pion mass is plotted in Fig. 2.13. The reconstructed K_S mass agrees to one part per mil with the value of the Particle Data Group (497.4 MeV vs. 497.7 MeV). The width of the peak (s = 0.0057, or $\approx$1.1 %) agrees with the resolution determined by Monte Carlo methods.

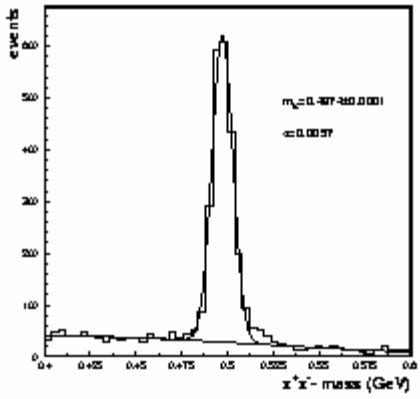

Figure 2.13: Invariant mass of p^+p^- pairs. The reconstructed K_S mass agrees very well with the PDG value

2.1.5 The Particle Identification Detectors

The particle identification (PID) system at HERMES consists of four components and was designed to identify the DIS positron (or electron) with high efficiency and low hadron contamination.

Threshold and Ring Imaging Cerenkov detector

The Cerenkov detector is used for the separation of leptons from hadrons and for pion identification in the momentum range between 4 and 14 GeV. Electromagnetic radiation (Cerenkov light) is emitted when a particle traverses a medium with a velocity larger than the speed of light in that medium, $n \geq c/n$ with n is the refraction index of the medium. The existing threshold Cerenkov detector was replaced in 1998 by a dual radiator Ring Imaging Cerenkov (RICH) to provide particle identification for pions, kaons and protons in the momentum range from 2 to 15 GeV [31]. The detector uses two radiators, a wall of silica aerogel tiles at the entrance of the detector, followed by a volume filled with C_4F_{10} , a heavy fluorocarbon gas.

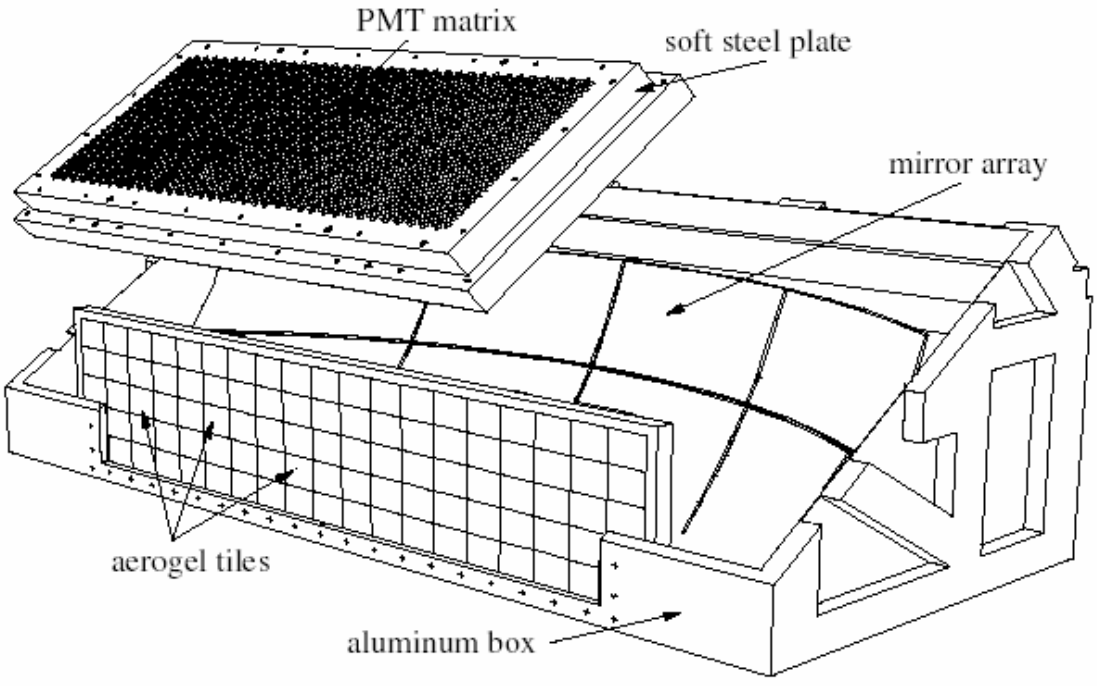

Figure 2.3: A cut away schematic view of the (top) RICH counter.

The photon detector consists of 1934 photomultiplier tubes (PMT) located above (below) the active volume for the top (bottom) part of the detector. The Cerenkov light cones are imaged onto the PMT by a spherical mirror array located at the rear of the radiator box. In Fig. 2.3 a schematic drawing of the main components of the (upper half of the) RICH are shown. Different Cerenkov angles are produced in the aerogel and the heavy gas depending on the index of refraction as $\cos q_c = c/nv$. Moreover, the size of the angle has a different momentum dependence for pions, kaons and protons, as is shown in Fig. 3.4. These differences allow the identi_cation of the different particle types with an efficiency of 98% for pions, 87% for kaons and 92% (82%) for protons (antiprotons).

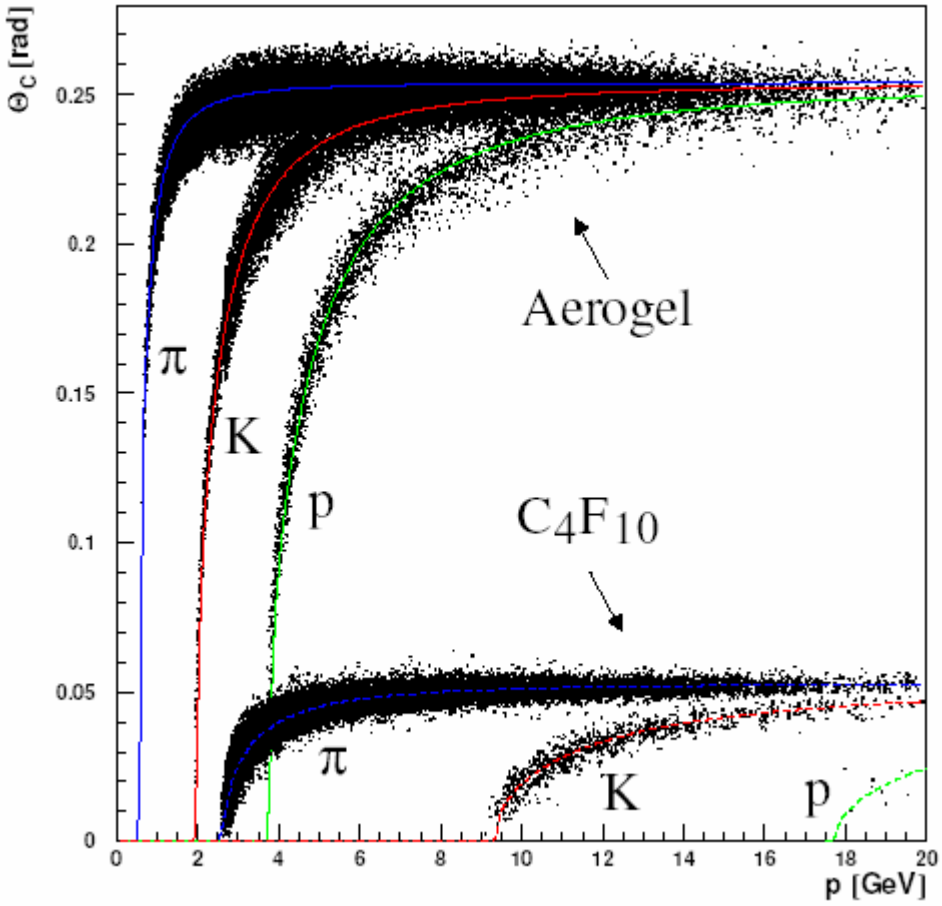

Figure 2.4: *The Cerenkov angle versus hadron momentum for the aerogel (upper band) and* C_4F_{10} *gas radiators (lower band). The data shown are based on a Monte Carlo simulation.*

The Calorimeter

The function of the calorimeter is to provide a first level trigger for scattered positrons, based on energy deposition in a localized spatial region (≥ 3.5 GeV in 1995 and the beginning of 1996 and ≥ 1.4 GeV in late 1996 and 1997); to suppress pions by a factor of ≥ 10 at the first level trigger and ≥ 100 in the off-line analysis; to measure the energy of positrons and also of photons from radiative processes or from p^0 and h decays. The solution chosen to meet these requirements consists of radiation resistant F101 lead-glass blocks arranged in two walls of 420 blocks each above and below the beam. Each block is viewed from the rear by a photomultiplier tube (PMT). The blocks have an area of 9×9 cm^2, a length of 50 cm (about 18 radiation lengths), and are stacked in a 42×10 array. The blocks were polished, wrapped with 0.051 mm thick aluminized mylar foil, and covered with a 0.127~mm thick tedlar foil to provide light isolation. Each block is coupled to a 7.62 cm Philips XP3461 PMT by a silicone glue (SILGARD 184) with refractive index 1.41. A m-metal magnetic shield surrounds the PMT.

To prevent radiation damage of the lead glass, both calorimeter walls are moved away vertically from the beam pipe by 50~cm for beam injection. The monitoring of gain and ageing is achieved using a dye laser at 500~nm, which sends light pulses of various intensities through glass fibres to every PMT of the calorimeter, and additionally to a reference counter photodiode. The various intensities are produced by a rotating wheel with several attenuation plates. The light is split in several stages before being fed into the glass fibres. As the gain of the photodiode is stable, the ratio of the PMT amplitude to that of the photodiode signal can be used to monitor relative gain changes in the photomultipliers. Over three years of operation, there has been no observed degradation of performance that would suggest ageing effects.

Radiation damage to the lead-glass is also monitored indirectly using TF1 blocks placed behind the calorimeter. This material is much more sensitive to radiation damage than F101. Therefore, a degradation of the response would be seen much sooner in these monitor detectors if there were a large radiation dose incident on the back of the calorimeter caused by showers produced by beam loss in the proton machine. So far no variation has been observed in their response, indicating that the effect of radiation damage is negligible.

Measurements with 1-30 GeV electron beams were performed at CERN and DESY with a 3×3 array of counters. Each lead-glass block was also calibrated within ≈ 1 % at DESY in a 3 GeV electron beam incident at the center of the block. The performance of a 3×3 array of counters showed [32]: (i) an energy response to electrons linear within 1 %, over the energy range 1-30 GeV; (ii) an energy resolution that can be parameterized as s (E) /E [%] = $(5.1 \pm 1.1)/\sqrt{E[GeV]}$ + (1.5 ± 0.5): this is similar to that obtained for other large lead-glass calorimeters; (iii) a spatial resolution of the impact point of about 0.7 cm (s); (iv) a PRF of $\approx (2.5 \pm 1.2) \times 10^{3}$ integrated over all energies in combination with the preshower detector, for a 95 % electron detection efficiency.

The ratio E/p (E and p are respectively the energy of positrons measured by the calorimeter and the momentum determined by the spectrometer) has a central value of 1.00 with a width (s) of 0.01, demonstrating that the response of the counters is uniform to $\approx$ 1 %. The long term stability of the detector response of 1 % is determined from the mean value of the E/p distribution, measured for each run for the counters nearest to the beam. This value also includes the contribution of the radiation damage produced in one year of operation, indicating the effect of the radiation damage is negligible.

The overall calibration of the calorimeter can be determined by the reconstruction of p^{0} decays. Fig. 2.17 shows the p^{0} invariant mass for events with two g clusters. The centroid of the peak for the 1995 data is (134.9± 0.2) MeV with a s = (12.5± 0.2) MeV in good agreement with the particle data group value. The calorimeter is described in more detail in a separate paper [33].

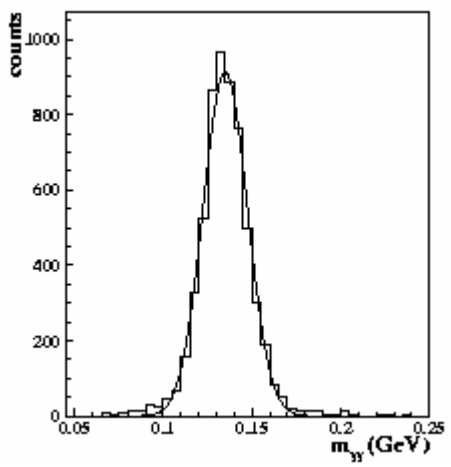

Figure 2.17: π^0 mass reconstructed from 2γ cluster events The Hodoscopes

A scintillator hodoscope (H1) and Pb-scintillator preshower counter (H2) provide trigger signals and particle identification information. Both counters are composed of vertical scintillator modules (42 each in the upper and lower detectors), which are 1~cm thick and 9.3~cm x 91~cm in area. The material for the modules is BC-412 from Bicron Co., a fast scintillator with large attenuation length (300 - 400 cm). The scintillation light is detected by 5.2~cm diameter Thorn EMI 9954 photomultiplier tubes, one coupled via a light guide to the outside end of each scintillator (away from the beam plane). The modules are staggered to provide maximum efficiency with 2 - 3~mm of overlap between each unit.

In addition to providing a fast signal that is combined with the calorimeter and H1 to form the first level trigger (H0 was implemented in 1996; see below), the H2 counter provides important discrimination between positrons and hadrons. This is accomplished with a passive radiator that initiates electromagnetic showers that deposit typically much more energy in the scintillator than minimum ionizing particles. The passive radiator consists of 11 mm (2 radiations lengths) of Pb, sandwiched between two 1.3~mm stainless steel sheets.

Forward Trigger Scintillators

A forward trigger scintillator (H0) placed directly upstream of the front drift chambers was introduced in 1996 to distinguish forward and backward going particles using the time of flight between the front and rear scintillators.

The total time required for a light-speed particle to traverse all trigger detectors is on the order of 18~ns, and hence a backward-going particle produces a pulse in the front counter that is displaced in time by about 36 ns from the normal trigger condition. Such a large time displacement allows for easy elimination of these background events in the trigger.

The front trigger detectors consist of a single sheet of standard plastic scintillator, 3.2 mm thick (0.7 % of a radiation length). The occupancy of the scintillators is such that segmentation of the detector is not necessary. The rate in each paddle is about 10^6 per second. The scintillation light is collected along the edge farthest from the beam axis into two sets of lucite strips and then into two 5.08~cm Thorn EMI 9954SB phototubes.

The Transition Radiation Detector

The purpose of the transition radiation detector (TRD) is to provide a pion rejection factor of at least 100 for 90 % positron efficiency at 5 GeV and above. Only positrons produce transition radiation in the HERMES energy regime and the detection of one or more TR X-rays in coincidence with the charged particle can be used to discriminate between positrons and hadrons. The X-ray is difficult to distinguish because it is emitted at an angle of $1/\gamma$ to the momentum of the charged particle and is therefore not separable in the detector from the positron.

Because the space restrictions imposed on the TRD were not severe, a relatively simple and economical design was chosen. Rather than optimize each module of the TRD for maximum performance, the overall performance is assured by the addition of extra modules. The design of the TRD was optimized using a Monte Carlo program that tracks charged particles and photons down to an energy of 1 keV. Care was taken to model properly the production of δ-rays in the radiator and the detector gas as well as hadronic showers in the radiator. Elements of the TRD simulation were later integrated into the general spectrometer simulation.

The HERMES TRD consists of 6 modules above and below the beam. Each module contains a radiator and a Xe/CH_4 filled proportional chamber. In addition, there are two flush gaps on either side of each detector through which CO_2 is flowed to reduce the diffusion of oxygen and nitrogen into the chamber. Such contaminants would affect the response significantly. CO_2 is used in the flush gaps because it is easily removed from the chamber gas during re-circulation. The use of polyethylene foils as a radiator is not practical for HERMES because of the large size of the modules (active area: 325 x 75 cm^2). It is not possible to maintain a uniform separation of the foils for such a large radiator. A good approximation to a foil radiator is provided by a pseudo-random but predominantly two-dimensional matrix of fibers. Several radiators were compared in a test beam at CERN: foils, fiber matrices with different fiber diameters, and polyethylene foams. Fiber radiators were shown to produce a response only slightly less than that from a foil radiator. The final design uses fibers of 17-20 μm diameter in a material with a density of 0.059 g/cm^3. This density is significantly less than would be found to be optimal if hadronic showers and delta rays from the radiator were ignored. The radiators are 6.35~cm thick, which corresponds to an average of 267 dielectric layers.

The detectors are proportional wire chambers of conventional design, each of which consists of 256 vertical wires of 75 μm gold coated Be-Cu separated by 1.27 cm. The wires are positioned with 25 μm accuracy using precisely machined holes for the crimp pins in plastic strips (Ultem) that are glued to the aluminium chamber frames. The chambers are 2.54 cm thick. Xe/CH_4 (90:10) is used as the detector gas because of its efficient X-ray absorption. The electric field in the chamber is produced by a +3100 V potential applied to the anode wires; the cathode foils are at ground potential. The large voltage on the anode wires is needed to produce an electric field in the critical region between the wires of sufficient strength to collect the ionization electrons within the 1 μsec ADC gate used in the readout electronics. The wire diameter was chosen to be unusually large to allow operation at this high voltage while limiting the gas gain to about 10^4.

Both positrons and hadrons deposit energy in the detector due to the ionisation of the chamber gas (dE/dx). The most probable energy deposited by a 5 GeV pion is about 11 keV. Positrons deposit on average approximately twice this amount of energy due to transition radiation

and the relativistic rise in Pure positron and hadron samples are selected by placing stringent, inefficient conditions on the other PID detector responses. A simple but effective method of analysis is the truncated mean method. In this technique, the largest signal from the six modules is discarded and the average of the remaining five modules is used. This procedure reduces the mean of the positron distribution but has a much more significant effect on the hadron tail that is due to rare events - production of energetic knock-on electrons. Fig. 2.20 shows the truncated mean distributions for the HERMES TRD derived from 1995 data. It is clear that the separation of the hadrons and positrons is greatly enhanced. The pion rejection factor varies with energy because both the energy loss by charged particles and the production of transition radiation depend on the energy of the incident particle. The cut on the response of the detector such that 90 % of the positrons are above the cut is set for higher efficiency for physics analysis.

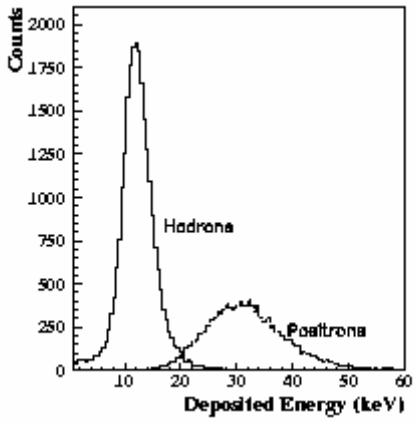

Figure 2.20: Truncated mean for six modules for positrons and hadrons, integrated over all momenta. Data from 1995 were used for this plot

The PRF can be improved using a probability based analysis similar to the one described in the section on PID system performance below. A probability function can be defined as

$$\Gamma_{TRD} = \log_{10}[P_{e^+} / P_h]$$

where P_{e^+} and P_h are the probabilities that a particle was a positron or a hadron respectively. The result of such an analysis for 1996 data is shown in Fig. 2.21. A cut for 90 % positron efficiency results in a PRF of 1460 ± 130. Even at 95 % positron efficiency, the PRF remains very good (489 ± 25).

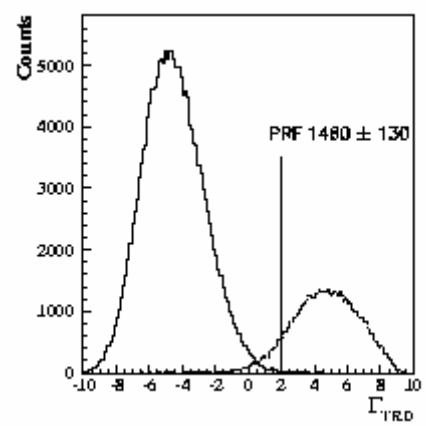

Figure 2.21: The logarithmic likelihood Γ_{TRD}, integrated over all momenta, for plot. The hadrons(positrons) is plotted as the solid line(dashed line). Data from 1996 were used for this vertical line indicates the location of a 90% efficiency positron cut

System Performance

The responses of the four PID detectors are combined to provide good hadron rejection. This has been done in several ways. The simplest technique is to consider the responses individually, determine a cut that separates positrons and hadrons in each detector, and define a positron/hadron as a particle identified as such in all detectors. A very clean sample of a given particle type can be produced in this way but at the cost of efficiency. Typically, this technique is used only for detector studies. The efficiency of the system can be improved while retaining good particle type separation by using a probability based analysis. The responses of the calorimeter, the pre-shower detector, and the Cerenkov detector are combined to produce the quantity PID3 defined as

$$PID3 = \log_{10}[(P^e_{Cal} P^e_{\Pr e} P^e_{Cer}) / (P^h_{Cal} P^h_{\Pr e} P^h_{Cer})]$$

where P_j^i is the probability that a particle of type i produced comparing the detector responses for each track to typical response a given response in detector j. The P_j^i's are determined by functions for each detector called parent distributions. The latter are either derived from the data or modelled using Monte Carlo techniques. The use of momentum dependent parent distributions is required to account for the varying responses of the detectors. PID2 is defined in a similar way to PID3 using only the calorimeter and the pre-shower detector. One can incorporate the TRD into the probability analysis to improve performance even further. The resulting function is labeled PID4. However, one then loses the straightforward systematic cross-checks described above and Monte Carlo simulation must be used to estimate the contamination of each particle sample as well as the detection efficiency. In order to keep as many events as possible for the final analysis, a so-called PID downshifting scheme was implemented. If all PID detectors provide valid data, a cut on a 2-dimensional PID3-TRD plot is used, which is equivalent to a straight cut on PID4. However, if information from either the TRD or the Cerenkov detector is not available a more limited scheme is used: if the TRD data are not available PID3 is used, while if the Cerenkov data are not useful a two-dimensional cut on the PID2-TRD plane is considered. For the analysis of the inclusive data in 1995, the full PID3-TRD scheme was used for over 97 % of the useful events.

Time of flight information from the hodoscopes can be used to separate pions, kaons and protons at low momentum (up to $\approx$2.9 GeV), the detailed description could be found in [34]. Another very effective way to do particle identification is to reconstruct the mass of particles with decay products in the spectrometer. This has been done for p^0, r, h, K_S, j, w, J/y, and Λ.

2.1.6 The Luminosity Monitor

The luminosity measurement is based on the elastic scattering of beam positrons from target gas electrons $e^+e^- \to e^+e^-$ (Bhabha scattering) and the annihilation into photon pairs $e^+e^- \to g\ g$. The cross sections are known precisely, including radiative corrections, e.g. $e^+e^- \to e^+e^-g, e^+e^- \to ggg$. In case of an electron beam in HERA, the process $e^-e^- \to e^-e^-$ (Moller scattering) is used. The scattered particles exit the beam pipe at z = 7.2 m and are detected

in coincidence by two small calorimeters with a horizontal acceptance of 4.6 to 8.9 mrad, which is limited by the size of the beam aperture in the magnet shielding plate. For a beam energy of 27.5 GeV the symmetric scattering angle is 6.1 mrad and both scattered particles have half of the beam energy. Due to the high radiation background in the region very near to the beam, the calorimeter consists of Cerenkov crystals of $NaBi(WO_4)_2$, which have a very high minimize radiation damage, the calorimeters are moved away from the beam pipe exit window by $\approx$ 20 cm in the horizontal direction for beam injection and dumping. Each calorimeter consists of 12 crystals of size $22\times22\times200$ mm^3 in a 3×4 array. The crystals are wrapped in aluminized mylar foil and coupled with optical grease to 1.9 cm Hamamatsu R4125Q photomultipliers with a radiation hard synthetic silica window and a bi-alkali photocathode.

An energy resolution of s (E)/E $\approx (9.3\pm0.1)\,\%/\sqrt{(E)}$ (E in GeV) has been determined for a 3×3 matrix from test beam measurements with 1-6~GeV electrons. Most of the scattered particles hit the inner crystals near the beam pipe. The deposited energy is reduced by lateral shower leakage, especially for hits near the inner crystal edge. Most of the background events have a high energy deposition in only one of the detectors while Bhabha events have a high energy deposition in both detectors. They are separated from background by triggering on a coincident signal with energy above 5~GeV in both the left and right calorimeter. A Bhabha coincidence rate of 132 Hz was measured with this trigger scheme for a beam current of 20 m A and ^{3}He areal target density of 1×10^{15} nucleons/cm^2. This provides a statistical accuracy of the luminosity measurement of 1 %, within about 100 s.

2.1.7 The Trigger

The function of the trigger system is to distinguish interesting events from background with high efficiency, and initiate digitization and readout of the detector signals. HERMES requires physics triggers corresponding to deep-inelastic positron scattering, photo-production processes (where no positron is detected) and additional triggers for detector monitoring and calibration. The trigger hierarchy is potentially capable of four levels. The first-level trigger decision is made within about 400~ns of the event using prompt signals of the scintillator hodoscopes, the calorimeter, and a

few wire chambers. This can be divided into the time necessary for signal formation in the detectors and transportation to the electronics trailer (≈ 250 ns including the transit time of the particle from the target), and the time needed for a decision by the trigger electronics (≈ 150~ns). The first-level trigger initiates digitization by the readout electronics. The second-level trigger could use any information available within the 50 m s during which time a hardware clear of the Fastbus readout electronics is possible. The third-level decision could be made on a timescale of a few hundred micro-seconds by existing digital signal processors in Fastbus, which would first read out only that part of the detector information required for the decision. In fourth level, the full data stream could be filtered by a farm of high performance processors that can make a decision on a timescale of ≤ 1 ms.

2.1.8 Data Acquisition and Readout Electronics

The HERMES *Data AcQuisition system* (DAQ) consists of two separated parts, the frontend electronics located in a trailer close to the experimental area and the online workstation cluster. The connection between the two is realized with optical fibers. The maximum DAQ throughput is 1.5 Mbyte/s. Raw events are collected online and separated in *runs*, of about 450 Mb recorded data. During the time needed for the digitization and readout of the detector, no new trigger can be accepted, leading to a trigger *dead time*. For each trigger a dead time fraction d_i is defined as:

$$d_i = 1 - \frac{T^i_{acc}}{T^i_{gen}}$$

where T^i_{acc} and T^i_{gen} are the number of accepted and generated triggers of type i respectively. The dead time fraction is dependent on the trigger rate. For each trigger a value of d_i is given every 10 seconds, the period of time (chosen arbitrarily) referred to as a *burst*. Data are normally analyzed which have d_i above 0.5, but a typical value for the dead time is higher (i.e. for the DIS trigger dead time around 0.9).

In addition to the standard detector readout, there is implemented a variety of asynchronous independent events, capable of trigger rates exceeding 5 kHz, including the luminosity monitor and

various high speed calibration and monitoring equipment. Depending on the application, the data from these events are either collected by the event collector during idle time or by dedicated additional CHIs and FREs.

Data are written to staging disks over the course of a fill of the storage rings, typically lasting 8-12 hours. The data are copied between fills to storage silos on the DESY main site via a FDDI link and associated hardware. The dead-time during standard running is typically well below 10 % and the downtime due to the data acquisition system is estimated to be below 1 %.

Chapter 3. Data Analysis

3.1.1 Data Quality

The data quality selection for the performed analysis was based on the standard HERMES information on the good bursts, which is done by data quality group for each year of data taking. Additional check on the level of physics was done based on the ratios of semi-inclusive hadrons to the number of DIS positrons (electrons), for each fill of the data taking for all data samples used in this analysis.

Furthermore, the ratio of the DIS positrons to the integrated luminosity has been thoroughly checked. After passing all regular data quality checks a special data set was produced from the standard HERMES micro-DST for each target and each year of data taking. In order to efficiently perform extraction of physics results, this data was set up as a substantial collection of multidimensional histograms (N-tuples), which allowed to investigate different correlations between the kinematical variables, as well as to check the consistency of obtained results for different years of data taking for the same target (e.g. Krypton or Xenon). Such work provides with a portable and powerful tool to perform every possible task related to data checks and analysis.

The typical plots with the comparison of the multiplicities for pions and kaons on Deuterium target for 1999, 2004 and 2005 years are shown in Figures 3.1 and 3.2.

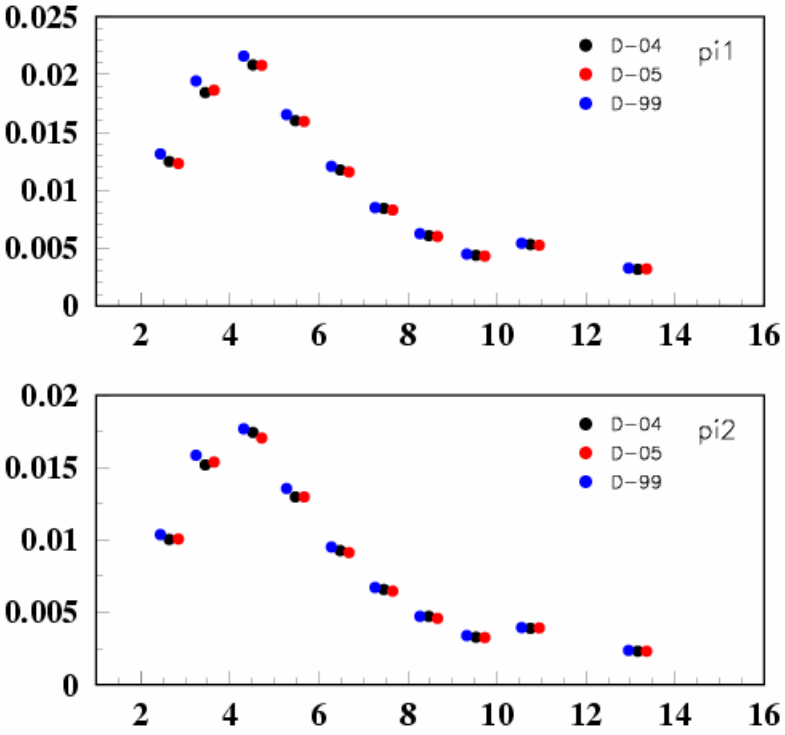

Figure 3.1: Comparison of multiplicities as functions of the hadron momentum for different years, for pions.

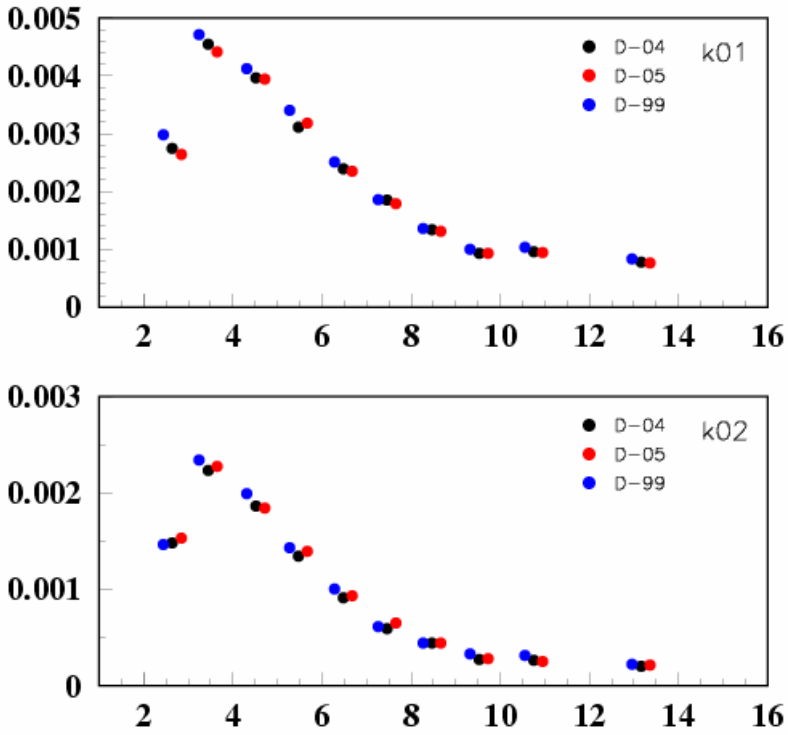

Figure 3.2: Comparison of multiplicities as functions of the hadron momentum for different years, for kaons.

3.1.2 Kinematic cuts and uncertainties

The kinematic requirements imposed on the scattered positrons were identical for all analyzed data $Q^2 > 1\ GeV^2$ ($Q^2 > 0.5\ GeV^2$ for the 12 GeV data), $W^2 = M^2 + 2M\nu - Q^2 > 2$ GeV for the invariant mass of the photon-nucleon system, where M is the nucleon mass, and $y = \nu / E < 0.85$ for the energy fraction of the virtual photon. The requirements on W^2 and y are applied in order to exclude nucleon resonances and to limit the magnitude of the radiative corrections, respectively.

As already mentioned in the previous section, using the RICH detector all charged hadrons were identified in the following momentum range: 2.0 - 15 GeV/c

To decrease the background for the neutral pions selection, the low momentum cut was determined to be 2.5 GeV/c. Data were analyzed in the region $6 < \nu < 23.5$ GeV and $z > 0.2$. For the case of one dimensional dependences: for ν -dependence the minimal cut was equal to 4 GeV, and for z - dependence the minimal cut was equal to 0, while for Q^2 and p_t^2 the minimum cuts were 6 GeV on ν and 0.2 on z. For the 12 GeV analysis pions are selected with $p_h > 2.0$ GeV/c and $z > 0.2$.

The integrated luminosities for all years and targets are listed in Table 3.1. The typical number of counts for DIS positrons and various hadrons, obtained on combined samples of Deuterium and Krypton targets during 1999 and 2004 years are listed in Table 3.2. These numbers for identified hadrons correspond to the kinematical cuts: $\nu > 6$ GeV and $0 < z < 1.2$. Most of the systematic uncertainties related to the detector, the reconstruction efficiencies and particle identification practically cancel in the ratio of the multiplicities. In determining the multiplicity ratios deuterium data collected in the same year as the data for the heavier target were used, to avoid uncertainties due to possible different conditions or functioning of the HERMES spectrometer during the years. It was checked that the multiplicity ratios obtained in different years were consistent within the (rather small) statistical error bars. By studying the multiplicity ratios as a

function of the hadron polar and azimuthal angles it was checked that the values of the charged multiplicities ratio R_A did not depend on the geometrical acceptance. This ratio was found to be constant within the statistical and systematical precision.

The charged pion sample is contaminated by pions originating from the decay of heavier mesons. The main effect on the pion multiplicities is due to the decay of exclusively produced r_0-mesons (pions resulting from the decay of r_0-mesons formed in the fragmentation process are included in R_A), which may affect the multiplicities by an amount ranging from about 1% at low z up to 30% (45%) at high values of z for positive (negative) pions, as estimated from a Monte Carlo simulation. The effect on the multiplicity ratio R_A is much smaller, but does not cancel completely since the r_0-mesons also interact with the nuclear medium. Taking into account the measured nuclear transparency [35] for r_0-mesons, the remaining effect on R_A has been carefully estimated and then corrected for. The value of the correction was included as one of the uncertainties contributing to the total systematic uncertainty.

The resulting overall uncertainty factors are as follows: different parameterizations of fragmentation functions and distribution functions, reflecting on the RC calculation systematics (< 2%), hadron identification (1.5% for neutral pions, 0.5% for charged pions, 2% for kaons, 2% for protons and 6% for antiprotons), overall efficiency (<2%), r_0-meson production for positive (0.3% - 4%) and negative (0.3% - 7%) pions. The estimated values of the total systematic uncertainties are presented in Tables 4.1-4.4 of Section 4.1. The error bars in the figures in the results section represent only the statistical uncertainties.

Target	Integrated Lumi
D_{99}	32.3
Kr_{99}	26.1
D_{00}	119.7
He_{00}	27.9
Ne_{00}	84.2
D_{04}	35.7
Kr_{04}	29.5
Xe_{04}	21.2
D_{05}	61.7
Kr_{05}	21.1
Xe_{05}	21.4

Table 3.1: Integrated luminosities (in pb^{-1}) for the various data sets (the subscript indicates the year the data were collected).

Target	DIS	π^+	π^-	K^+	K^-	p	$\overline{p}$
D	6669k	706k	575k	146k	62k	131k	23k
Kr	3516k	286k	232k	68k	26k	69k	8k

Table 3.2: Number of counts for DIS leptons and various hadrons collected on deuterium and krypton targets in 1999, 2004 and 2005 combined. The numbers are for the following kinematical constraints: n >6 GeV and z > 0:2.

3.1.3 RICH Unfolding

The RICH detector is only efficient for hadron momenta from 2 to 15 GeV/c. For the pions one could go down to as low as 1 GeV/c, however in this case the RICH unfolding procedure becomes inconsistent. Furthermore, the input matrices are only available starting from 2 GeV, so for the pions we also use the range from 2 to 15 GeV/c. Additionally, the RICH provides a quality parameter rQ_p. If this parameter equals to zero, the RICH is unable to correctly identify the particle. Hence another cut is used for rQ_p to be always greater than zero.

The RICH hadron identification efficiency is subject to a certain amount of misidentification that varies with particle momentum. This is described by two complimentary sets of probability matrices called the *P* and the *Q* matrices. An element in the *P*-matrix, P_t^i, gives the probability that a

particle of true type t is identified by the RICH as a type i, where i , $t = p$, K, p and i can also be X, meaning that the RICH was unable to identify the particle. One can define P_t^i as

$$P_t^i = \frac{N_t^i}{\sum_j N_t^j} \tag{3.1}$$

where N_t^i is the number of particles with true type t and identified type i, and write for the P-matrix:

$$P(p,T) = \begin{pmatrix} P_p^p & P_K^p & P_p^p \\ P_p^K & P_K^K & P_p^K \\ P_p^p & P_K^p & P_p^p \\ P_p^X & P_K^X & P_p^X \end{pmatrix} \tag{3.2}$$

The matrix $P(p,T)$ depends on the particle momentum p and the event topology T, more specifically the number of tracks in the detector half where the particle tracks resides. This means there can be more than one Cerenkov cone image on the PMT-matrix. There overlapping rings cause difficulties in the reconstruction of the opening angles, therefore decreasing the identification efficiency. The HERMES RICH group has provided P-matrices [36] in the case of track multiplicity of 1, 2 and more than 2 tracks per detector half. Note that the diagonal elements of this P-matrix are the usual detection efficiencies (see Eq. 3.1) Due to its probabilistic interpretation, the columns of the P matrix are normalized to 1, i.e.:

$$\sum_i P_t^i = 1 \tag{3.3}$$

It was mentioned before, that two complimentary sets of matrices can be used to describe hadron misidentification. The second se it the so-called Q-matrix, where an element Q_t^i gives the probability that a particle identified as being of type i, is in fact of type t. With P_t^i one has the probability that the particle is of true type t, and P_t^i gives us the probability that it is identified as type i, whereas with Q_t^i, however we know the particle is identified as i, and Q_t^i gives the probability that it is truly of type t. So,

$$Q_t^i = \frac{N_t^i}{\sum_s N_s^j} \tag{3.4}$$

and one can write

$$Q = \begin{pmatrix} Q_p^p & Q_K^p & Q_p^p & Q_p^X \\ Q_p^K & Q_K^K & Q_p^K & Q_K^X \\ Q_p^p & Q_K^p & Q_p^p & Q_p^X \end{pmatrix} \tag{3.5}$$

The P and Q matrices are related through Bayes' theorem:

$$Q_t^i = \frac{P_t^i \cdot f_t}{\sum_s P_s^i \cdot f_s} \tag{3.6}$$

in which f_t is the relative flux of the hadron type l

$$f_t = \frac{N_t}{\sum_s N_s}, \qquad N_t = \sum_t N_t^i \tag{3.7}$$

It is important to note that the Q matrix depends on the event sample used, so in fact it depends on the type of physics analysis. Its elements depend on the particle flux, which is obviously different for various analyses. Generation of Q matrices makes things rather complicated and increases the amount of overhead needed for an analysis. The P matrix, in turn, is a pure detector quantity and independent of other factors. So naturally, this is the quantity made available to the collaboration by the RICH group. This choice, albeit very logical, does make things a bit more complicated. Following the definition of the Q matrix, it directly gives us a vector with the true particle probabilities $\vec{N}$, starting from the identified particle type $\vec{I}$,

$$\vec{N} = Q \cdot \vec{I} \tag{3.8}$$

where

$$\vec{N} = \begin{pmatrix} N_p \\ N_K \\ N_p \end{pmatrix} \qquad \vec{I} = \begin{pmatrix} I_p \\ I_K \\ I_p \\ I_N \end{pmatrix} \tag{3.9}$$

For the *P* matrix this relation is:

$$\vec{I} = P \cdot \vec{N} \tag{3.10}$$

In order to obtain the true particle types $\vec{N}$ one has to *unfold* them from the identified particle type in *I.* In this case this technically implies inversion of the *P* matrix.

It is analytically not possible to invert a 3x4 matrix in a closed algorithm, and one would have to resort to minimization or iteration procedures [37]. However, since the fraction of unidentified X-particles is small [36], one can neglect them and use what is called the *truncated P matrix*:

$$P_{trunc}(p,T) = \begin{pmatrix} P_p^p & P_K^p & P_p^p \\ P_p^K & P_K^K & P_p^K \\ P_p^p & P_K^p & P_p^p \end{pmatrix} \tag{3.11}$$

which is a non-singular, square matrix. Therefore it has a unique inverse which enables one to solve the equation 3.10:

$$\vec{N} = P_{trunc}^{-1} \cdot \vec{I}_{trunc}, \text{ where } \vec{I}_{trunc} = \begin{pmatrix} I_p \\ I_K \\ I_p \end{pmatrix} \tag{3.12}$$

So we can determine e.g. the real *K* flux by interpreting N_K as a weight. If we have a particle which is identified as a pion:

$$\vec{I}_{trunc} = \begin{pmatrix} 1 \\ 0 \\ 0 \end{pmatrix} \tag{3.13}$$

Then we would also have to count $(P_{trunc}^{-1})_K^p$ in the true kaon spectrum since there was a small probability that the pion was in fact a kaon. Note that the elements in P_{trunc}^{-1} are not probabilities due to the fact that the matrix was truncated. However, they do provide the correct true hadron fluxes because the so-called *X*-particles are cut out in the analysis anyway.

In this work, event by event correction for the unfolding effect has been performed. In order to determine the statistical weight to apply to each event, the ratio between the true momentum spectra of given hadron type, to the input one has been used, whereas the former has been obtained using the *unfold2a.f* code provided by the RICH group [36]. The input histograms contained data already within all the cuts relevant to the analysis. The effect of the unfolding procedure has been studied both on the separate multiplicities on all nuclear targets, as well as on the super-ratio (attenuation) of the multiplicities, as a function of hadron momentum and z. Figures 3.3, 3.4 and 3.5 show the distributions of the multiplicities with and without the unfolding procedure on the Krypton target and for positive pions, kaons, and protons. More plots containing distributions for all nuclear targets and all hadrons observed in the analysis can be found in Appendix A.

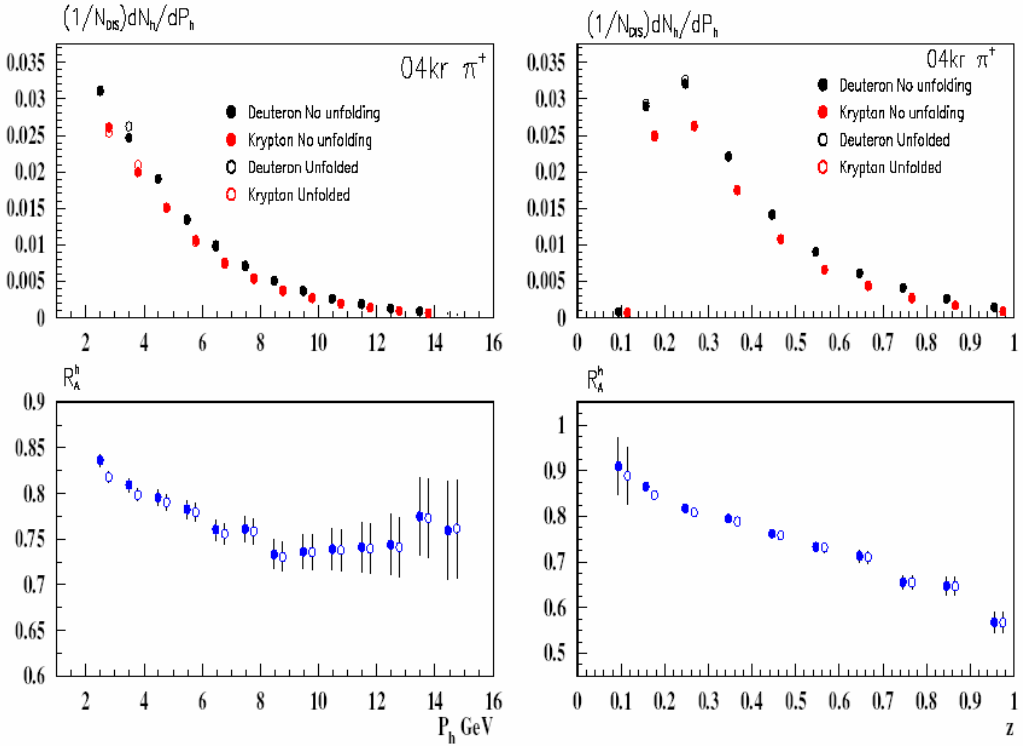

Figure 3.3: Distributions of the multiplicities with and without the unfoldin, versus the hadron momentum (left panel) and z (right panel) for positive pions.

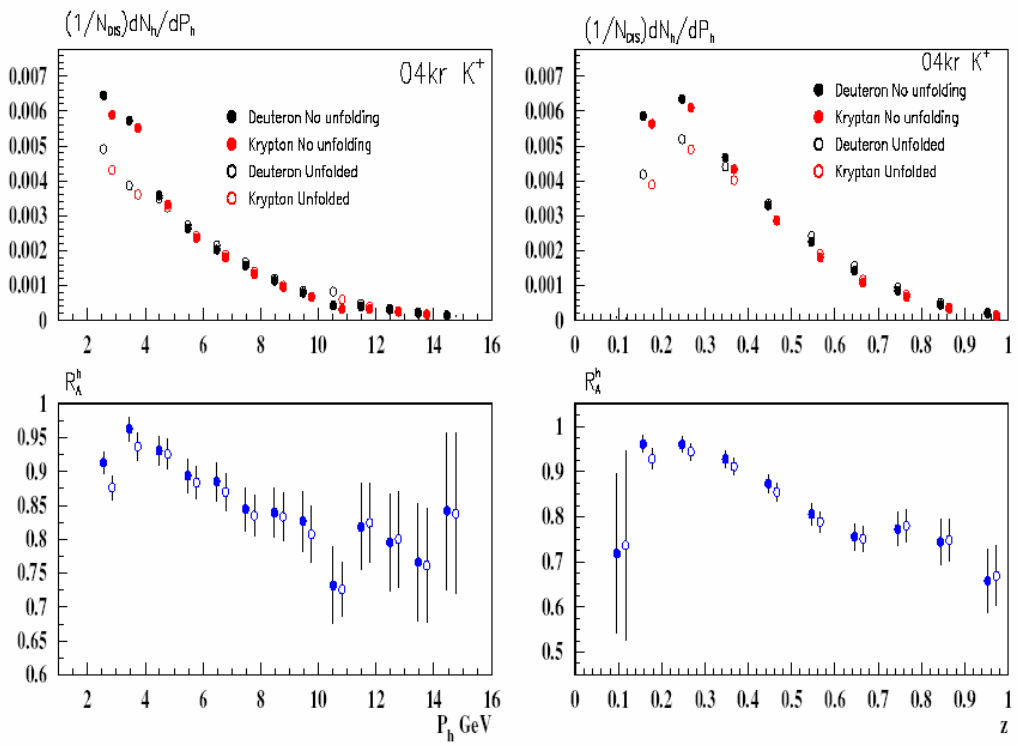

Figure 3.4: Distributions of the multiplicities with and without the unfoldin, versus the hadron momentum (left panel) and z (right panel) for positive kaons.

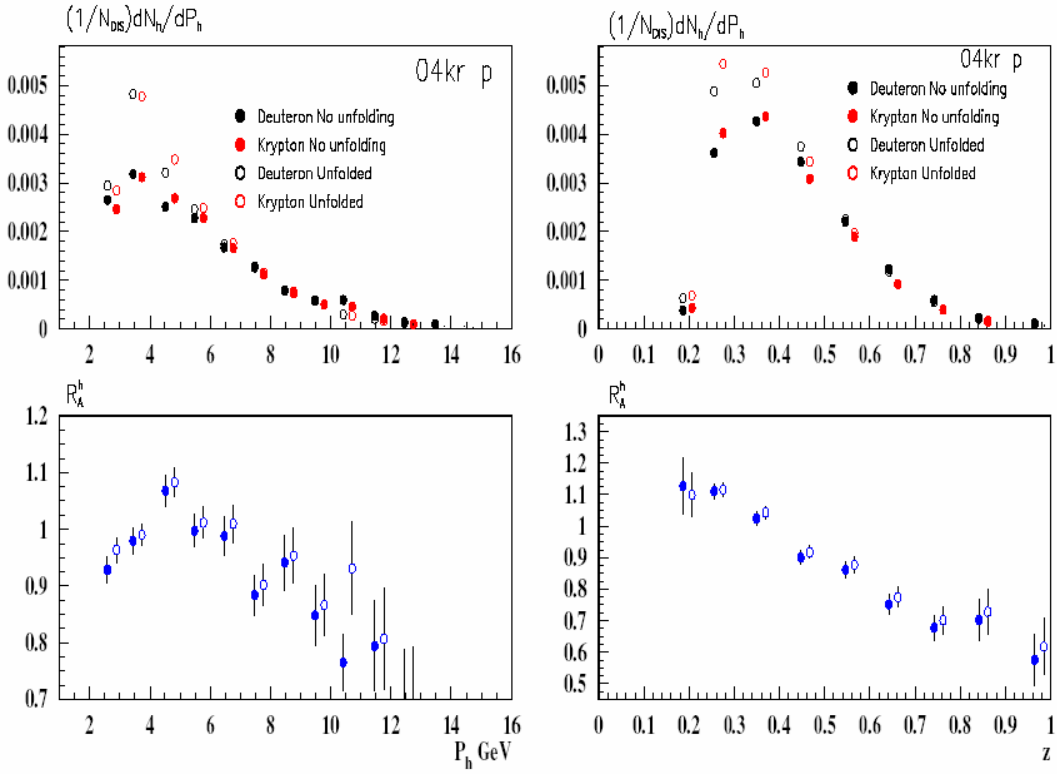

Figure 3.5: Distributions of the multiplicities with and without the unfoldin, versus the hadron momentum (left panel) and z (right panel) for protons.

In order to estimate the systematic uncertainties due to the applied RICH unfolding procedure, two sets of *P* matrixes were produced with different RICH MC production (versions *2a* and *3a*). Then the systematic uncertainty was estimated according to the following expression [38]:

$$\Delta_{sys} = \frac{|R_{2a} - R_{3a}|}{\sqrt{3}} \qquad (3.14)$$

Also different topology of event was taken into account, because of the efficiency of RICH identification strongly depends on the number of charged tracks per half of the detector. Each event was marked by special sign corresponding to this maximum number of tracks per half of detector. Then different type of *P* matrixes was used to make the unfolding procedure following the scheme described above. The typical distributions of tracks per event for the negatively charged detected pions, kaons and protons on deuterium target for top and bottom part of the HERMES detector is shown on Figure 3.6 for two lowest momentum ranges, where the efficiency of identification for the RICH is minimal.

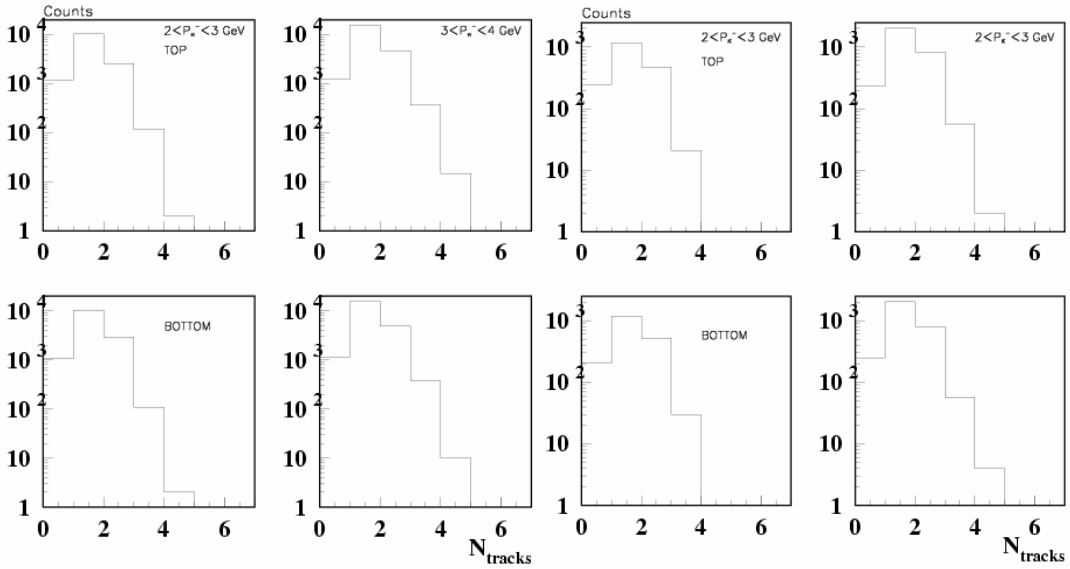

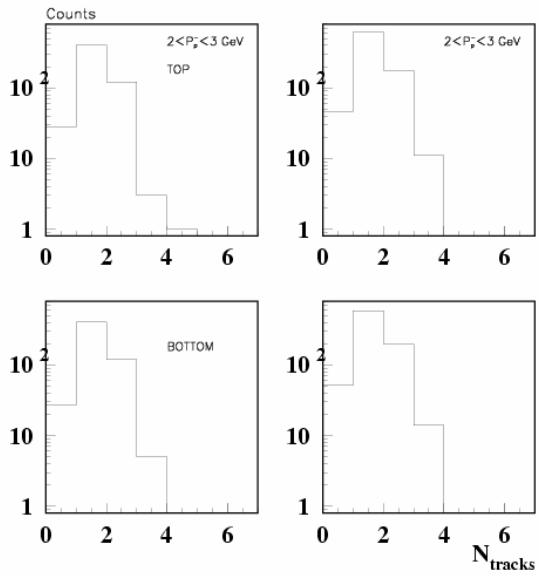

Figure 3.6: Track multiplicities for pions, kaons and protons for two lowest momentum ranges, where RICH efficiency is low.

3.1.4 Corrections for Radiative and Detector Effects

The radiative correction (RC) needs to account for three different processes in which a photon is radiated. The elastic scattering of the positron on the nucleus as a whole, the quasi elastic interaction of the positron with one of the nucleons inside the nucleus, and the inelastic scattering of the positron on a single quark. These contributions are calculated using the TERAD code, a code based on the method outlined in Ref. [39-40-41]. Since TERAD is a code developed for inclusive DIS, it does not account for the z dependence of the radiative corrections. Due to the requirement that a produced hadron is also detected the phase space of the radiated photon can be slightly different from that in the inclusive case and may thus depend on z . To account for this effect, an additional multiplicative correction is calculated using the SIRAD code [42], which was specifically developed for the evaluation of radiative corrections in semi-inclusive deep inelastic scattering on hydrogen. This code properly treats the z dependence of the radiative correction. Detailed description of the RC procedure can be found in Ref [43-44].

The presented data for the multiplicity ratios were corrected for radiative processes in the manner described in references above. The radiative corrections are applied to both the inclusive DIS ratio and the semi-inclusive ratio in Eqn. (1.22). For the inclusive cross sections elastic, quasi-elastic and inelastic processes are taken into account, whereas for the semi-inclusive ratio only inelastic radiative processes contribute. The correction for the latter ratio was taken to be independent of z. Since the inelastic radiative effects are almost the same for nucleus A and D, the size of the radiative corrections applied to R_A was rather small in most of the kinematic range. Only in kinematical points where the elastic and quasi-elastic tails are non-negligible, i.e., at the highest value of n and lowest value of Q^2 (low x_{Bj}), there is a noticeable effect on nuclear attenuation, with a maximum (increase) of R_A of about 7% for Xenon and Krypton, 4.5% for Neon and 1% for Helium.

In addition, the DIS cross section has to be corrected for the inefficiency caused by the photon shower effect, which is a detector inefficiency caused by the radiated photons. In inelastic processes such photons are mostly emitted in the direction of either the beam lepton (*initial state radiation*, ISR) or the scattered lepton (*final state radiation*, FSR). On the other hand hard photons associated with nuclear elastic scattering, i.e. Compton scattering, are emitted typically at very small angles. The Bethe-Heitler cross section for radiative elastic processes predicts that in kinematic conditions corresponding to quite small values of x, the Compton peak becomes much more prominent compared to ISR and FSR, simply because smaller values of Q^2 become kinematically available, and the cross section is proportional to a factor $1/Q^4$. At low x and Q^2 the Compton photons are emitted at very small angles, and these energetic photons from nuclear targets have a high probability of hitting the detector frames surrounding the beam line in front of the spectrometer magnet, and may produce extensive electromagnetic showers. In such a case the high multiplicity seen by the tracking detectors makes it impossible to perform track reconstruction. This will result in a large inefficiency in particular in the kinematic region where these photons are emitted, i.e. corresponding to small values of and x and Q^2. Corrections for these process-specific inefficiencies must be applied, since they increase in severity as the of nuclear targets increases. A

GEANT-based Monte Carlo was set up that includes a detailed geometry description of the detector frames and the beam pipe. The resulting reconstruction efficiencies x_A for target nucleus A compared to that for deuterium are shown in Fig. 3.7 as a function of x for the different targets.

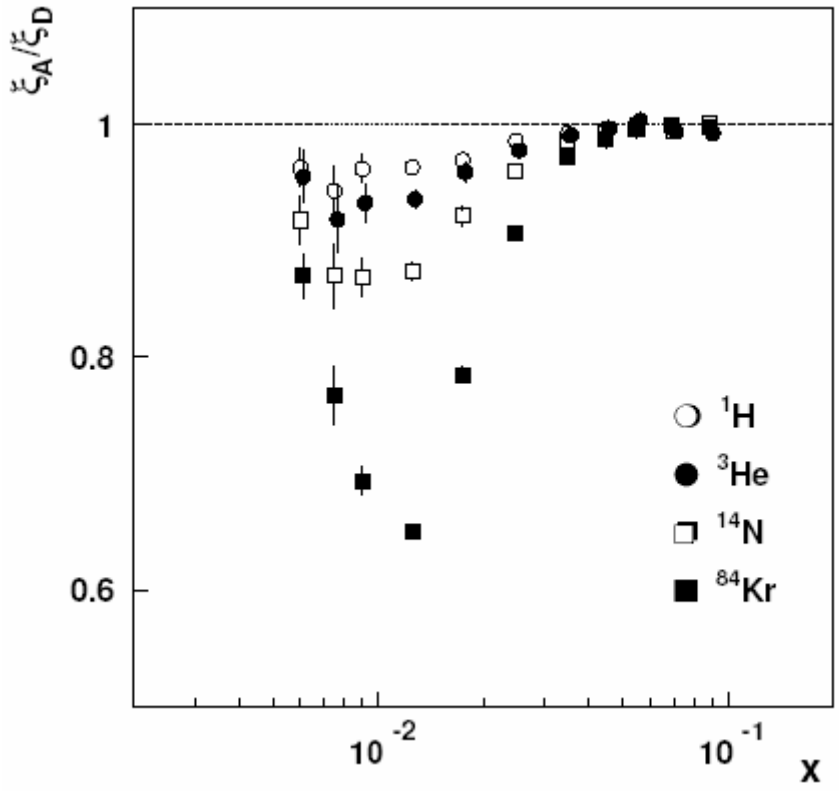

Figure 3.7: Ratio of track reconstruction efficiencies in H, He, N and Kr with respect to that in deuterium as a function of x.

The reconstruction losses are strongly dependent on target material and on , and consequently on x and Q^2. {Note that these reconstruction efficiencies, which have been determined from a Monte Carlo simulation, include not only the tracking efficiency but also geometric acceptance effects.

As for the semi-inclusive analysis, the photon shower corrections are also quite small, reaching a maximum of 7% in the highest n-bin (which corresponds to the lowest x value). The photon shower correction for each n-bin of the present analysis has been calculated separately for the 1999 Krypton and Deuteron data [44] and is shown in Fig. 3.8.

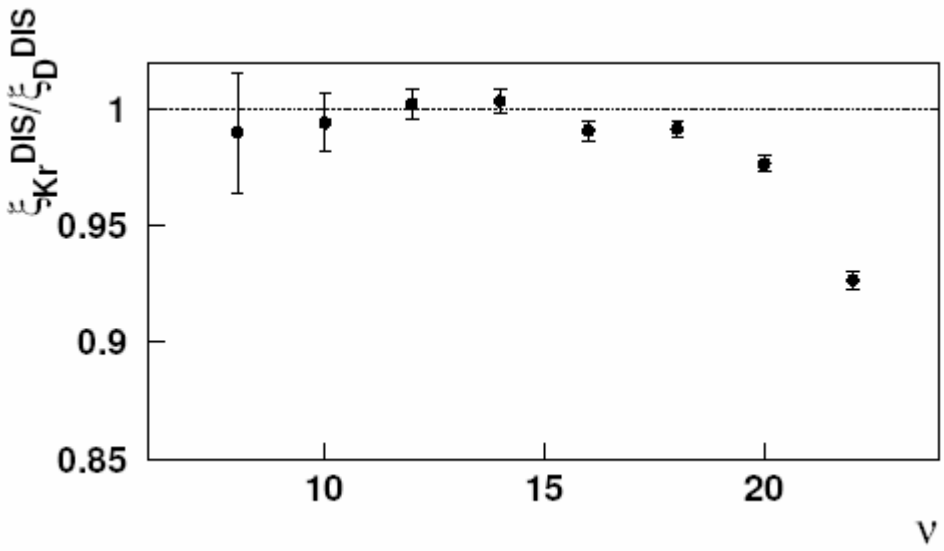

Figure 3.8: Ratio of efficiencies for the detection of DIS events on krypton and deuterium in the ν *range covered by the semi-inclusive analysis.*

Since present analysis uses more data samples from more recent data collected in 2000, 2004 and 2005 years of data taking, the application of the same correction described above (which was applied to the 1999 data) had to be studied with regard to the new data. Therefore, a special *mDST* has been set up for both 1999 and 2004 data, which involved geometrically reproducing the detector with either Top or the Bottom part forcefully blanked out in order to observe events that only went to either half of the spectrometer. The data for this production has then been compared with a normal production that has both halves of the spectrometer enabled. The results of such comparison are presented in Fig. 3.9. The data is presented in terms of the All/TOP/BOT ratios as functions of x. The ratios are built as follows: for each case, let's say All/TOP, the nominator contains the DIS events from normal production selected – by series of cuts - in a way that only the ones that went into the upper half of the detector are involved, and the denominator has the DIS events from the special production where only the upper half of the detector was on, meaning that bottom part was blanked out. And naturally, the All/BOT is built in a similar way but vice versa.

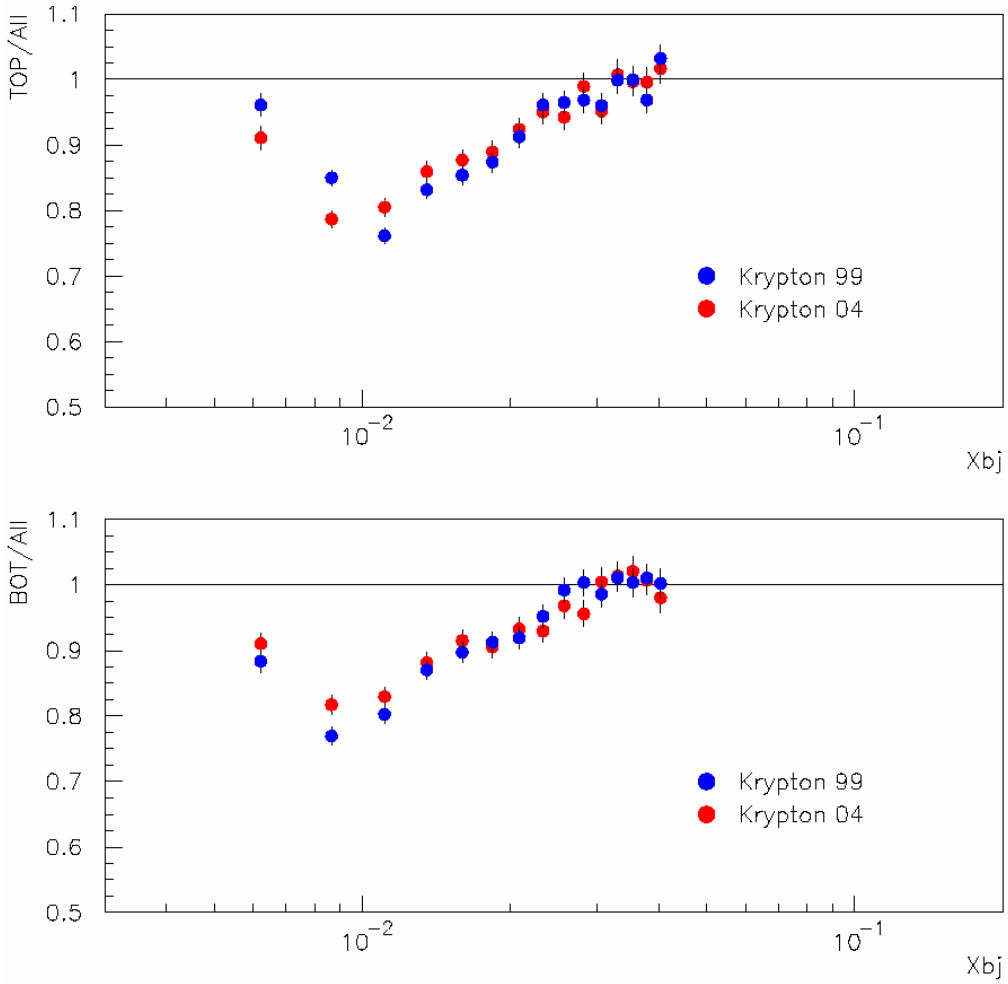

Figure 3.9: Comparison of the Top/Bottom ratios for data from 1999 and 2004 Krypton production as a function of x

From these first results we can already see no dramatic difference between the 1999 and 2004 (except for the extreme low x bins, but they are not used in the attenuation analysis). In addition to that, a special Monte-Carlo production for 2004 results has been performed with artificially introduced misalignment in the geometry file to match the conditions in the data production. The result of this MC production has also been compared with the data, which is demonstrated on Fig. 3.10. One can note very nice agreement between both the MC and data for Krypton and Xenon and throughout the 1999 and 2004 data production. This allows us to safely apply the shower correction of 1999 Krypton data to the latest 2004 and 2005 Krypton and Xenon data.

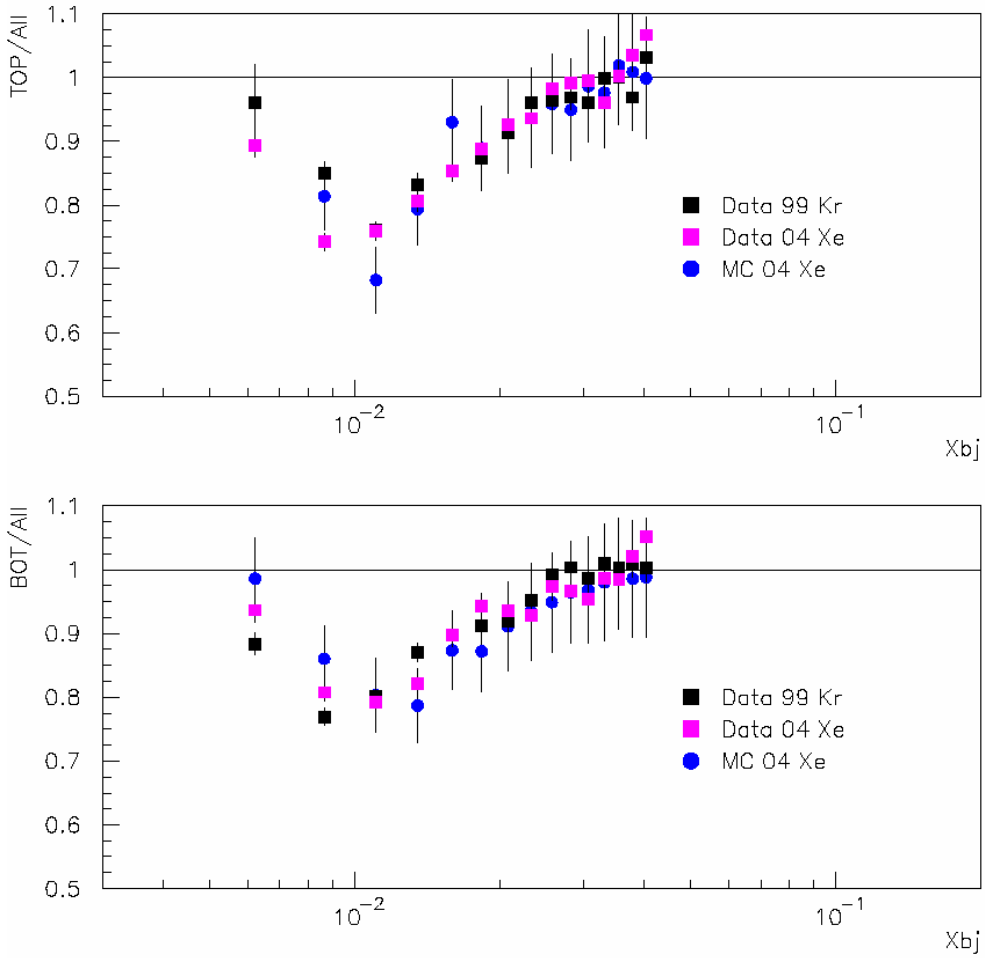

Figure 3.10: Comparison of the 2004 MC and 2004,1999 data for the showering effect as a function of x.

3.1.5 Corrections due to exclusive r_0 production

The semi-inclusive pions sample used in present analysis could be contaminated by another pions coming from the decay of exclusive r_0 meson. Because of different mechanism of production for those pions it is very important to estimate possible influence of such pions on measured multiplicity ratio. To perform such estimate the Monte Carlo studies were done, using one of the existing generators for exclusive r_0 production, which is *rhoMC* [45]. The advantage of this generator is the incorporated parameter, such as the slopes value in differential cross-section as a function of t Mandelstam for different nuclear targets. The forward diffractive peak of the cross section as a function of *t'* was modeled according to:

$$\frac{dN}{dt} \propto e^{-b|t|}$$

where *b* represents the values of the slope parameters listed in Table 3.3.

Also the experimental information existing at HERMES collaboration about the relation between the coherent and incoherent parts of the cross section on different nuclei was used.

Nuclear targets	Deutron	Neon	Krypton	Xenon
Slope values GeV^{-2}	**24.4**	**50**	**148**	**201**

Table 3.3 Typical slope values use for the MC simulation

The scheme to calculate this correction factor is based on our knowledge on experimental determined number of coherent r_0 on different nuclear target and acceptance function, which reflects the ratio of two and only one pion from the exclusive r_0 detected by HERMES spectrometer. This ratio was calculated using the *rhoMC* generator. The following formulae clearly explain the approach:

$$R^{Corr} = \frac{\left[\frac{N_p^{SIDIS} - N_p^r}{N_{DIS}}\right]^A}{\left[\frac{N_p^{SIDIS} - N_p^r}{N_{DIS}}\right]^D} = \frac{N_{DIS}^D (N_p^{SIDIS})^A}{N_{DIS}^A (N_p^{SIDIS})^D} \times \frac{\left[1 - \frac{(N_p^r)^A}{(N_p^{SIDIS})^A}\right]}{\left[1 - \frac{(N_p^r)^D}{(N_p^{SIDIS})^D}\right]} =$$

$$= R^{Meas} \times \frac{\left[1 - \frac{(N_p^r)^A}{(N_p^{SIDIS})^A}\right]}{\left[1 - \frac{(N_p^r)^D}{(N_p^{SIDIS})^D}\right]} = h(z) \qquad (3.15)$$

where $N_p^r = N_{2p}^r + N_{1p}^r = N_{2p}^r(1 + \frac{N_{1p}^r}{N_{2p}^r})$. Whereas only the value of $C(z) = \frac{N_{1p}^r}{N_{2p}^r}(z)$ is obtained from *rhoMC*. The remaining values come from the experimental data, and are used in the calculation. Data selection to extract the exclusive r_0 meson from the data has been done according to the following criteria:

Fiducial volume cuts

Trigger 21 required

|g1Track.rVertZ| < 18cm, g1Track.rVertD < 0.75cm

$|q_x|$ < 0.18, 0.04 < q_y < 0.14

Q^2 > 1, W^2 > 4, y <0.85

ΔE < 0.6

0.6 < $?_{p^+p^-}$ < 1 GeV

Figure 3.11 shows a typical plot for the invariant mass of the two opposite charged pions with a prominent peak corresponding to r_0-meson.

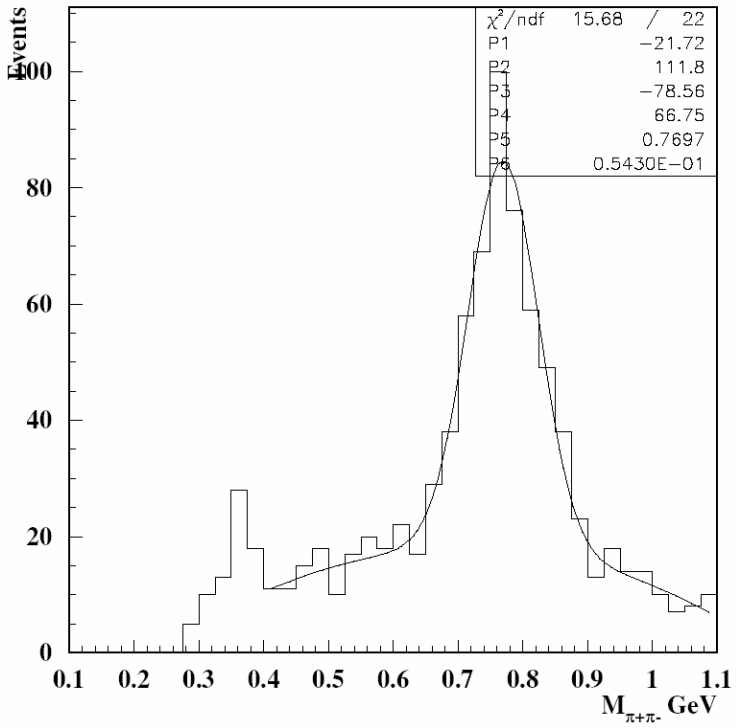

Figure 3.11: The invariant mass of p^+p^- from the Xenon data with ΔE < 0.6.

The comparison of results for the fraction of energy carried by one of the pions from the r_0-meson decay is shown in Figure 3.12. On the next plot (Fig. 3.13) one can see the ratio of events with only one and with two detected pions from the r_0-meson decay for Deuteron, Krypton and Xenon targets. This ratio is obtained from the *rhoMC* simulation.

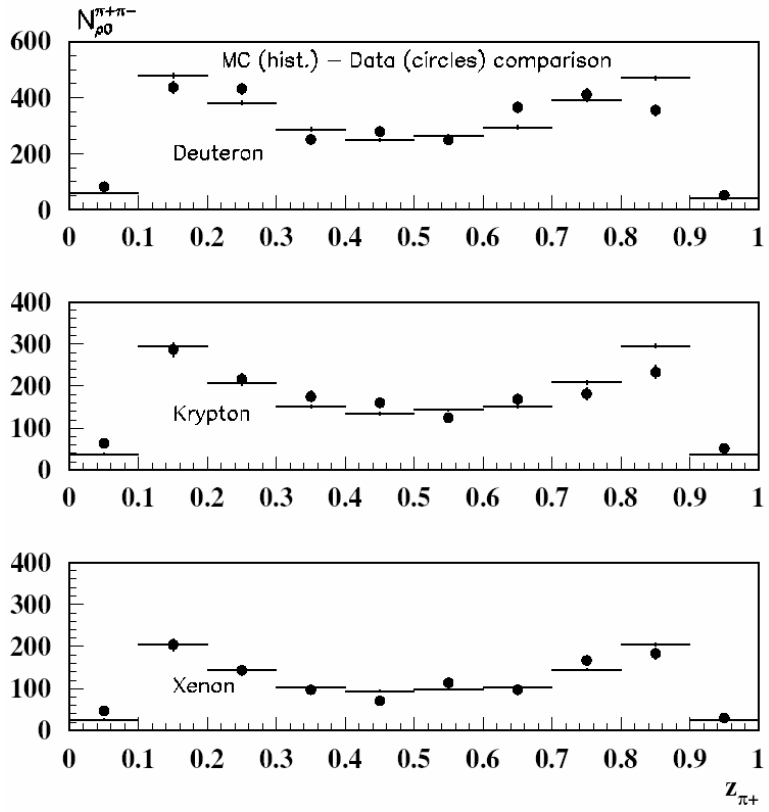

Figure 3.12: The comparison of z_{p^+} distribution from rhoMC (histogramm) with the data (circles).

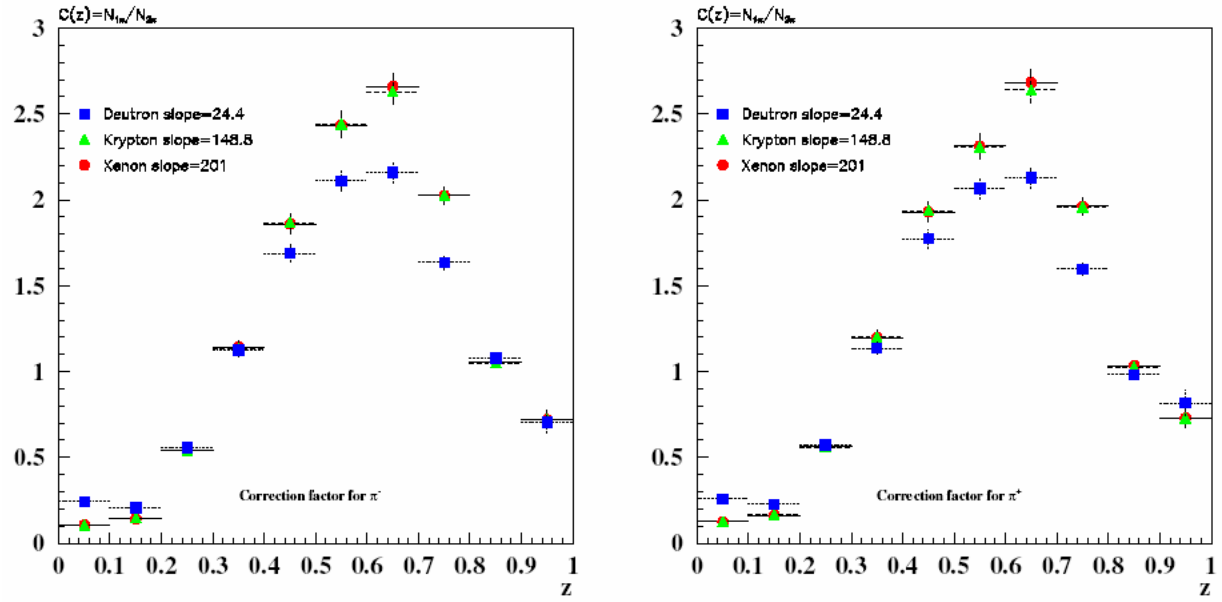

Figure 3.13: The ratio $\frac{N_{1p}^r}{N_{2p}^r}$ of only one accepted pions from the r_0-meson decay to the case when both pions are accepted, calculated with rhoMC as a function of $z_{p^\pm}$

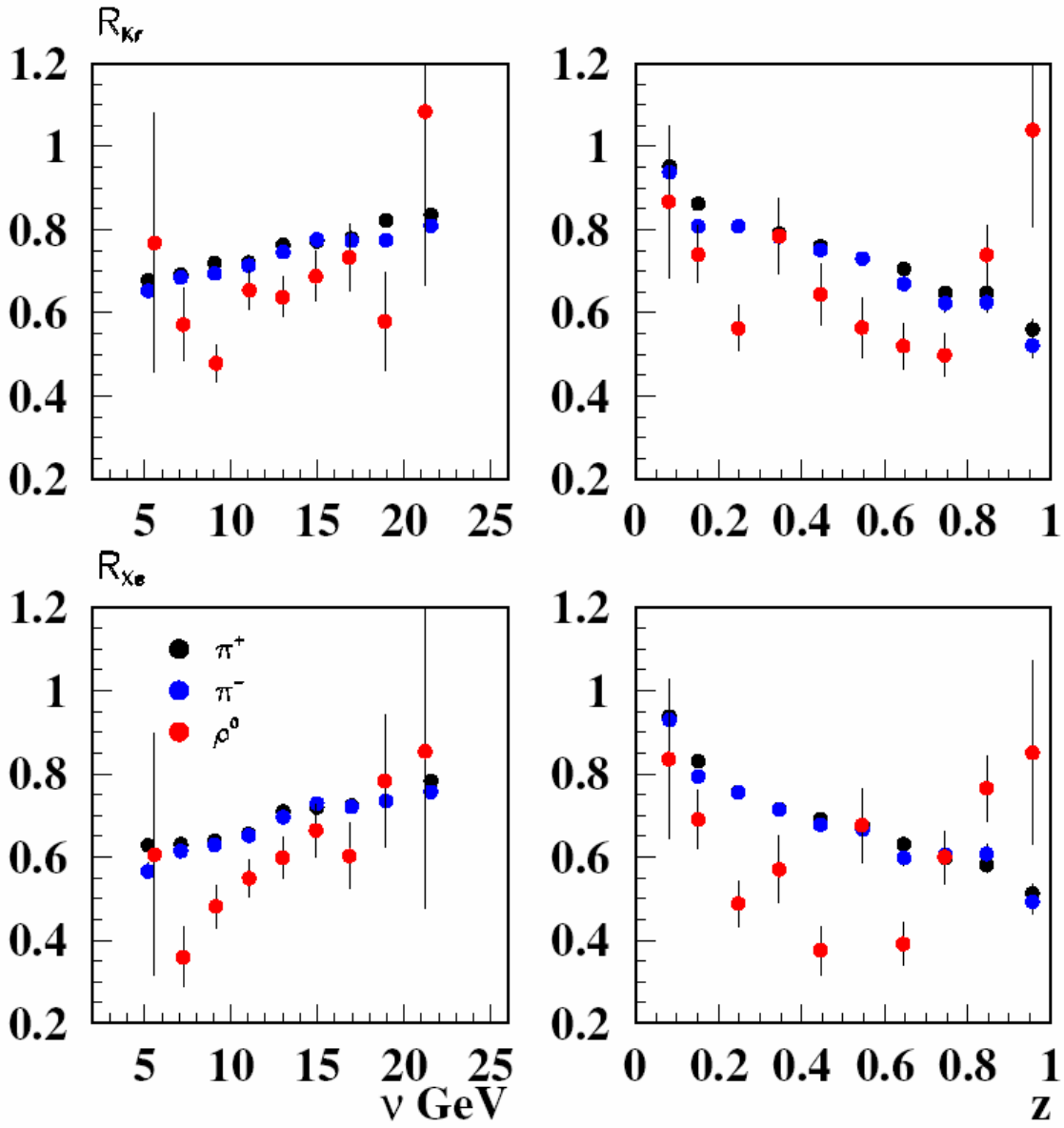

Figure 3.14: The attenuation ratio for semi-inclusive pions and exclusive r_0-mesons as a function of n (left panels) and z (right panels).

The multiplicity ratios for the exclusive r_0-mesons as functions of n and z for Krypton and Xenon nuclear targets have been calculated and are shown in Figure 3.14. Figure 3.15 presents the calculated correction factor for the multiplicity ratio due to exclusive r_0 production as a function of z_p, and finally Figure 3.16 shows the same correction factor, but calculated for the number of semi-inclusive pions for Deutron, Krypton and Xenon nuclear targets.

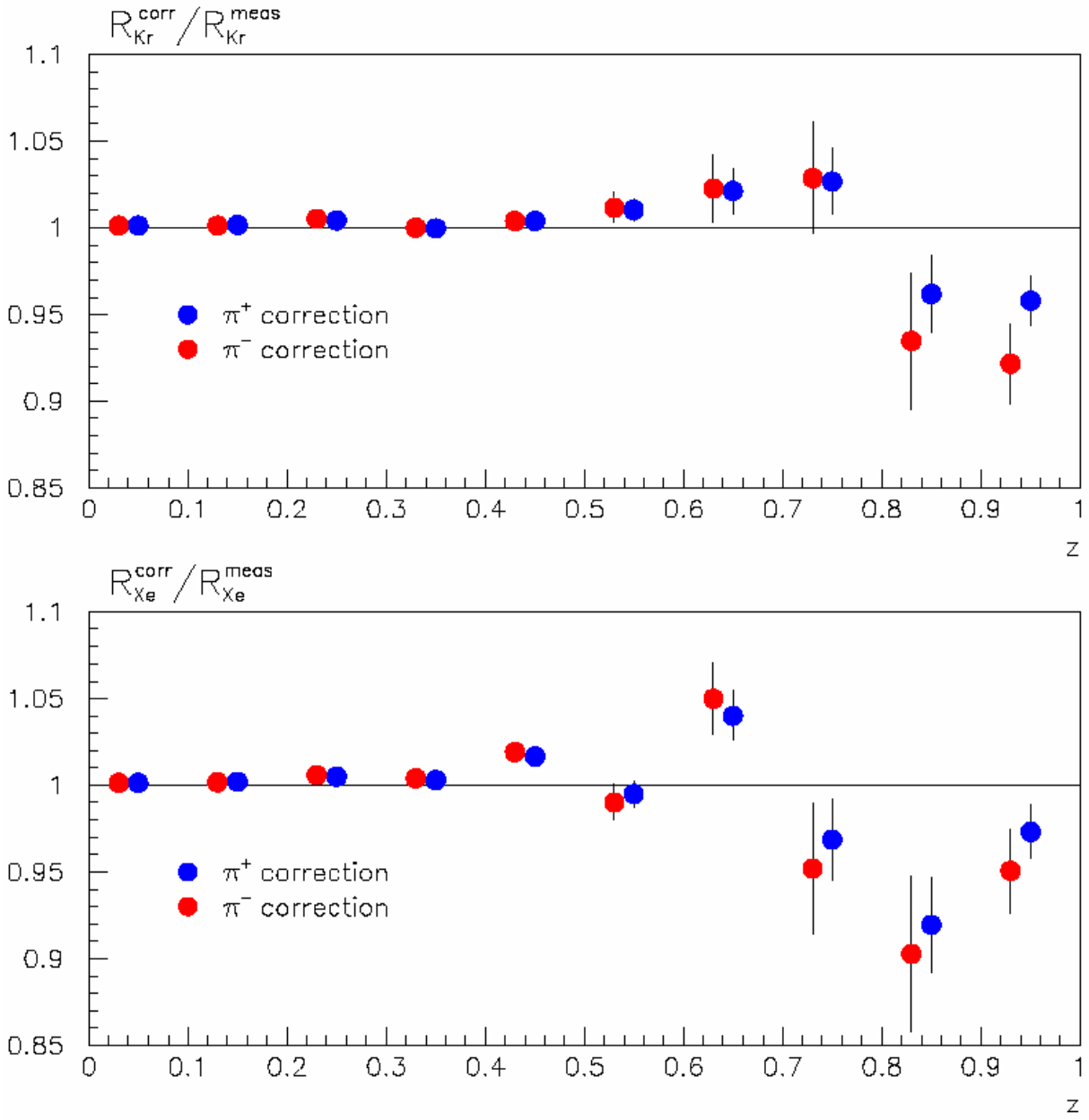

Figure 3.15: The calculated correction due to exclusive ρ_0-meson production to the attenuation ratio for Krypton (top panlel) and Xenon (bottom panel), as a function of z.

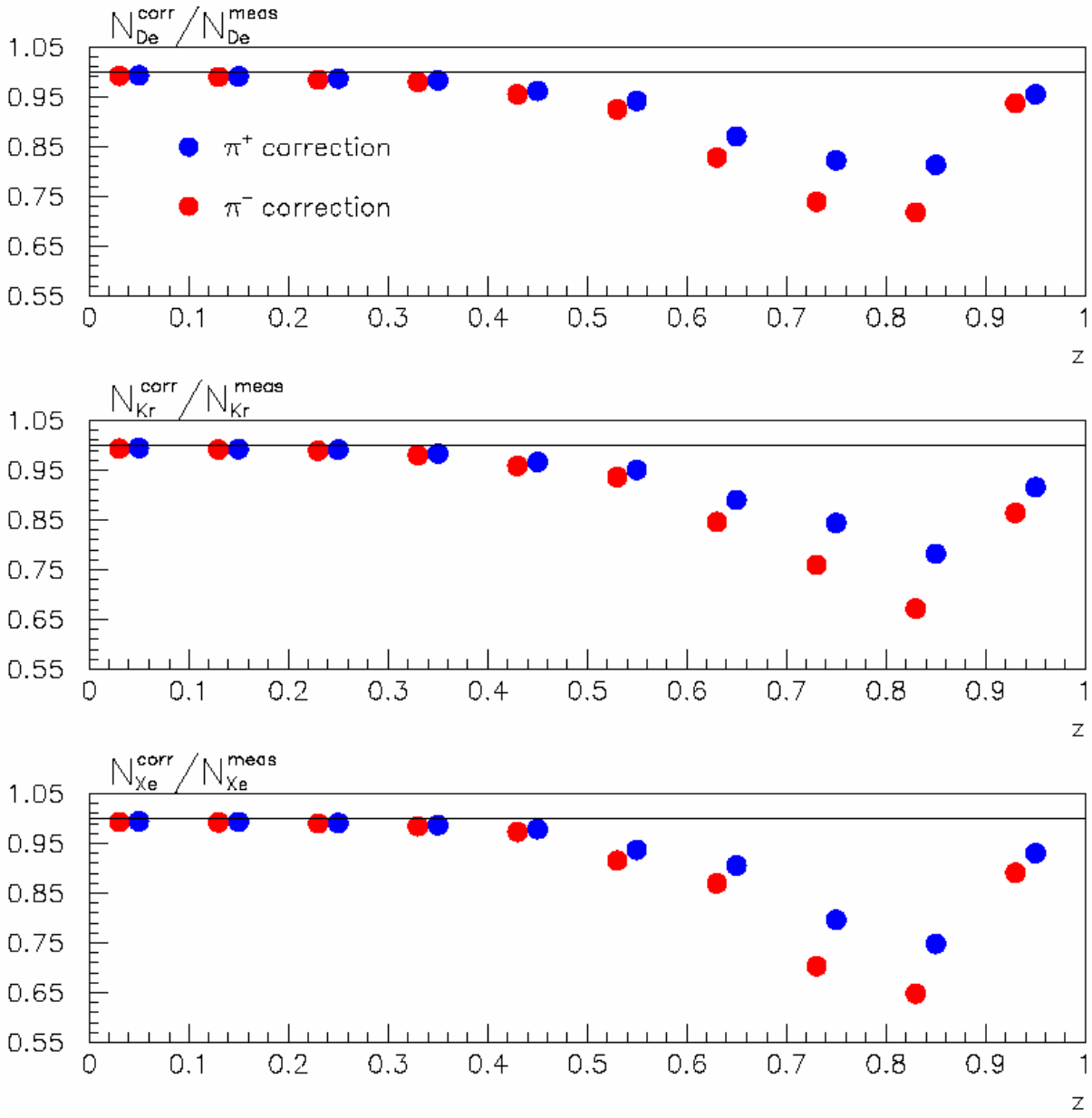

Figure 3.16: The calculated correction due to exclusive r_0-meson production to the number of semi-inclusive pions for Deutron (top panel), Krypton (middle panlel) and Xenon (bottom panel), as a function of z.

The scheme described in this section has a substantial advantage. Since the only quantity for which Monte-Carlo simulation is necessary is the two-pion to one-pion ratio $C(z) = \frac{N_{1p}^r}{N_{2p}^r}(z)$, the calculation depends very little on the MC generator used. The shape and level of such correction factor calculated using the PYTHIA generator [46], is very similar to those obtained in this work. As it is shown from the last plots, this correction for the multiplicities reaches a maximum of 25-35% at higher values of $z \sim 0.8$-0.9.

Chapter 4. Results

4.1 One-dimensional results

The first results for the hadron multiplicity ratios were obtained for the Nitrogen target, using the data from the 1997 production [8]. The differential multiplicity of charged hadrons and identified charged pions from nitrogen relative to that from deuterium have been measured as a function of n and z. Already then, substantial reduction of the multiplicity ratio R_A has been observed at low n and high z. Also, significant difference of the n -dependence of R_A^h was found between the positive and negative hadrons. This is interpreted in terms of different formation times of protons and pions. Figures 4.1 and 4.2 show the z- and n -dependence of the multiplicity ratio for hadrons and pions. One has to note that in 1997 year of data taking, the RICH detector was not yet in operation, and a threshold Cerenkov counter was used to distinguish hadrons with energies of over 1.4 *GeV* from leptons.

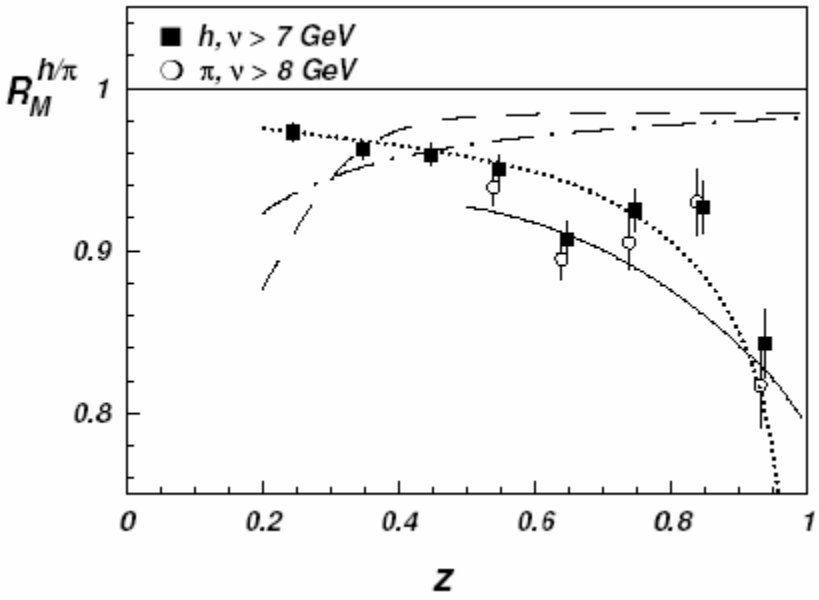

Figure 4.1: The multiplicity ratio as a function of z for all charged pions (open circles) and all charged hadrons including pions (closed squares).

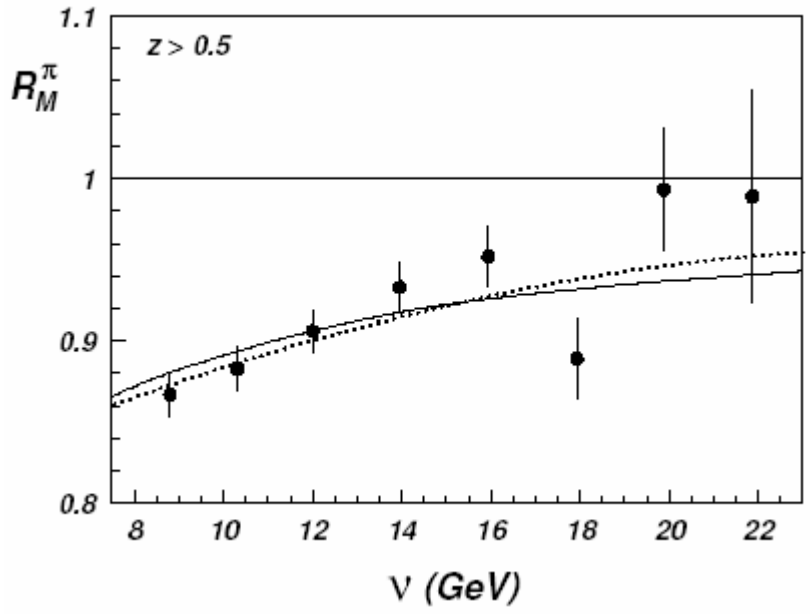

Figure 4.2: The multiplicity ratio as a function of n *for charged pions with* $z > 0.5$.

Next set of results have been obtained using a heavier nuclear target, Krypton for various identified hadrons [3,47]. R_A^h have been determined as a function of n, z and p_t^2. Once again, strong reduction of the multiplicity ratio in the nuclear medium at low n and high z is observed, with significant differences among various hadrons. The distribution of the hadron transverse momentum is broadened towards high p_t^2 in the nuclear medium, in a manner resembling the Cronin effect previously observed in collisions of heavy ions and protons with nuclei. The results are shown in Figures 4.3 and 4.4

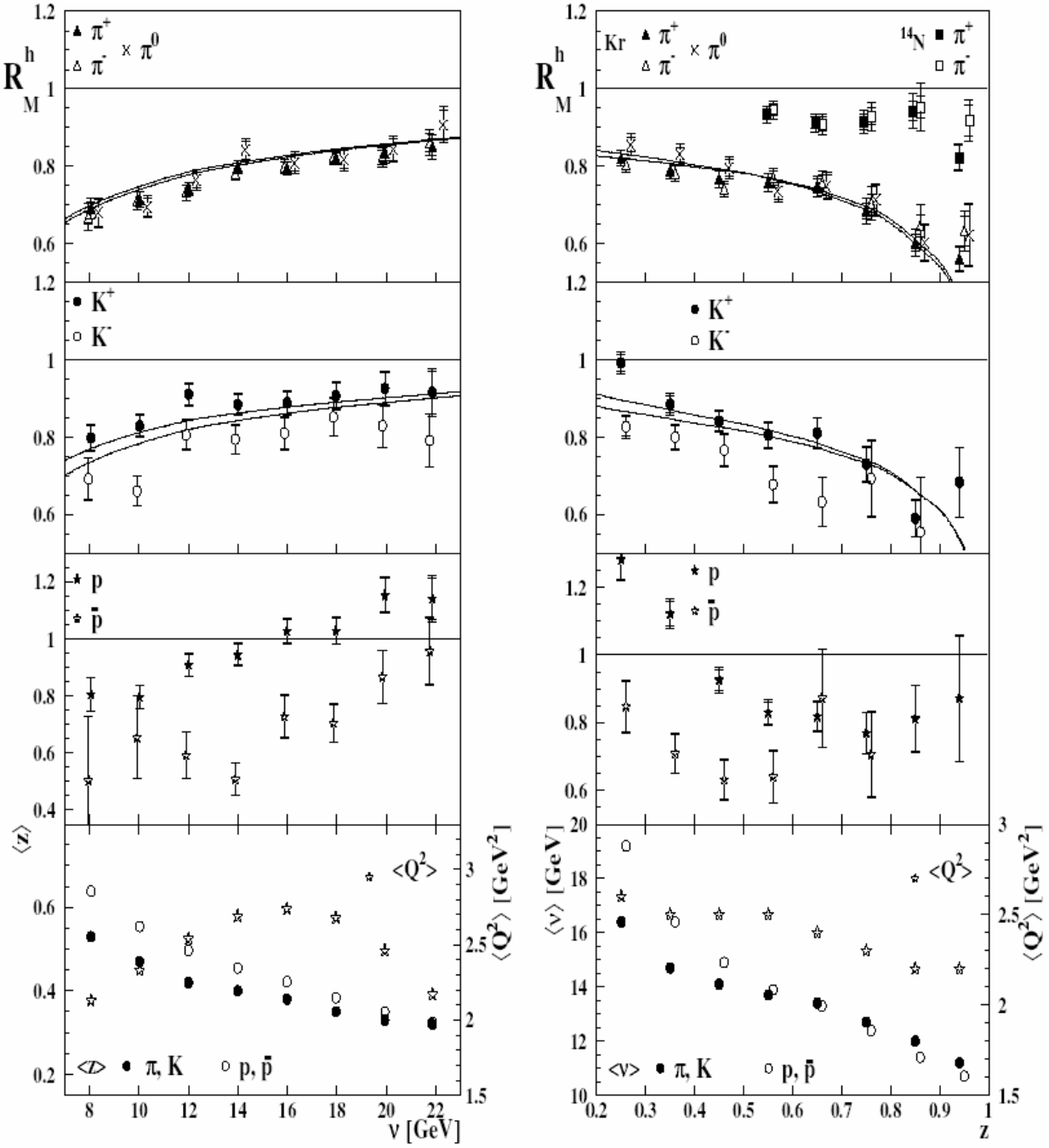

Figure 4.3: Multiplicity ratios for identified pions, kaons protons and antiprotons from a Krypton target as a function of ν *for* $z > 0.2$ *and* z *for* $\nu > 7$*Gev.*

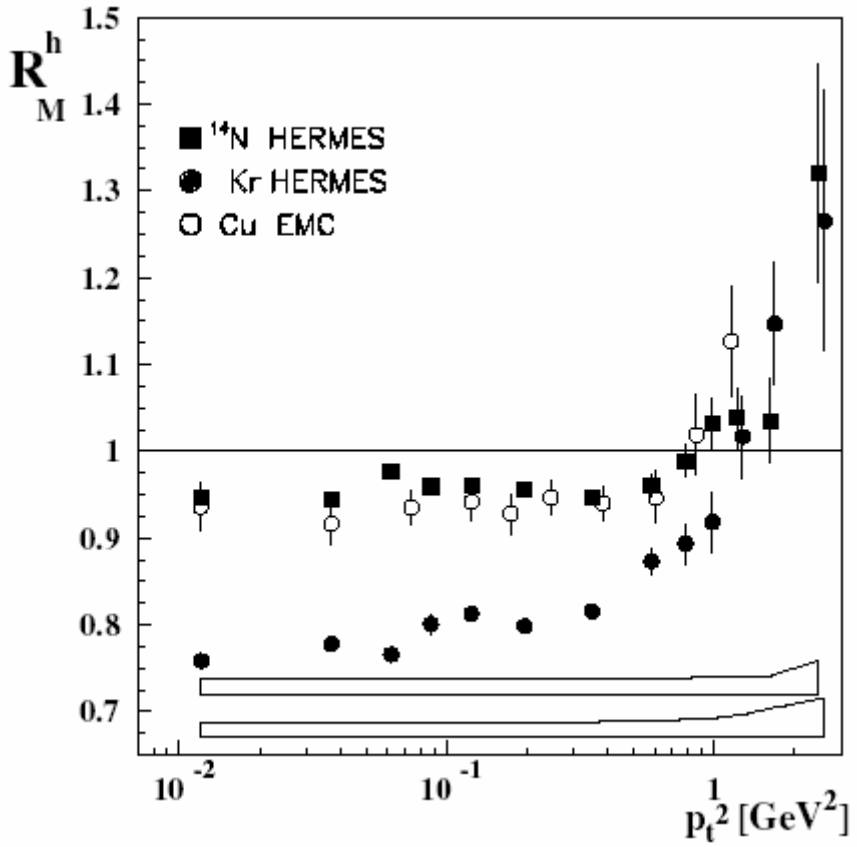

Figure 4.4: Multiplicity ratio for charged hadrons versus p_t^2 for ν >7 GeV and z >0.2. The HERMES data on Krypton and Nitrogen are compared to the EMC [5] data for Cuprum in the range of 10 < ν < 80 GeV

Following those results more studies were undertaken, and while HERMES has accumulated substantial statistics on heavier nuclear targets, the analysis could be expanded to re-include all of the data sets and also, using the particle identification mechanisms, present the results for different types of hadrons. The hadron multiplicity ratio as defined in Eq. 1.22 was determined as function of the leptonic (Q^2 and ν) and hadronic (z and p_t^2) variables for all identified particles and all targets. Figures 4.5, 4.6, 4.7 and 4.8 show the kinematic dependences of R_A on ν , z , Q^2 and p_t^2 for the different nuclei for all identified hadrons: positive (pions, kaons and protons), negative (pions, kaons and anti-protons), and neutral (pions), respectively. The basic feature of the data (visible for all variables) is the decrease of R_A with increasing value of the mass number of the

nucleus. Furthermore, a strong similarity between the data for p^+, p^- and p^0, and a clear difference between those for K^+ and K^-, and those for p and $\overline{p}$ should be noted. These features can qualitatively be understood from the following global arguments. Since we use (almost) isoscalar targets, both the production and the absorption of pions is in first instance independent of their charge. A slightly larger attenuation of p^- compared to p^+ observed even for Neon, especially at low n and z (i.e. low momenta) can be explained by different absorption of lower energy p^+ and p^-.

The values of R_A^h for K^+ and K^- show the same behavior as function of the various variables, but $R_A^{K^-}$ is consistently smaller than $R_A^{K^+}$. Positive kaons are largely produced from valence quarks, while negative kaons (except at small values of *x*) are produced mainly from gluons (the production rate on Deuteron is already rather different). This leads to a steeper dependence of the K^- fragmentation function on z, and thus a reduced production, if the parton has lost energy before hadronization, Also, due to their quark content, nuclear absorption cross sections are larger for K^- than for K^+. Hence both the energy-loss/fragmentation process and absorption of the produced kaon can explain the observed values for R_A^h. Protons have some special features that make them not directly comparable to any of the other particles. Because they are already present in a nucleus, first of all not all of them have to come from hadronization (there is a very large difference in production of p and $\overline{p}$ on D). Furthermore, during subsequent interactions in the nuclear volume they generally are not absorbed, but by scattering give rise to more nucleons, both protons and neutrons, at lower z, therefore possibly even increasing R.

In the next subsections the dependence of R on the kinematical variables n, z, Q^2 and p_t^2 will be discuss?d separately. Tables 4.1, 4.2, 4.3 and 4.4 give, for Krypton, typical representative example of values of R_A^h and the statistical and systematical uncertainties, as well as

the average values of the kinematic quantities that were integrated over. Those average values hardly depend on the target at all.

bin	ν range	$\langle\nu\rangle/GeV$	$\langle Q^2\rangle/GeV^2$	$\langle z\rangle$	$\langle p_T^2\rangle/GeV^2$	$R_{Kr}^{\pi^+}$	Δ_{stat}	Δ_{sys}
1	4.0 - 6.0	5.266	1.988	0.584	0.255	0.675	0.011	0.021
2	6.0 - 8.0	7.148	2.150	0.501	0.170	0.676	0.006	0.025
3	8.0 - 10.0	9.093	2.324	0.448	0.144	0.711	0.005	0.027
4	10.0 - 12.0	11.029	2.494	0.422	0.151	0.735	0.005	0.028
5	12.0 - 14.0	13.009	2.660	0.408	0.173	0.755	0.005	0.028
6	14.0 - 16.0	14.987	2.770	0.395	0.202	0.782	0.005	0.027
7	16.0 - 18.0	16.981	2.738	0.372	0.235	0.795	0.005	0.025
8	18.0 - 20.0	18.963	2.610	0.353	0.279	0.829	0.007	0.025
9	20.0 - 23.5	21.535	2.286	0.328	0.334	0.854	0.008	0.025
						$R_{Kr}^{\pi^-}$		
1	4.0 - 6.0	5.272	1.969	0.581	0.231	0.642	0.013	0.026
2	6.0 - 8.0	7.156	2.096	0.500	0.156	0.679	0.007	0.035
3	8.0 - 10.0	9.090	2.287	0.448	0.138	0.699	0.006	0.037
4	10.0 - 12.0	11.032	2.429	0.420	0.143	0.729	0.005	0.038
5	12.0 - 14.0	13.009	2.583	0.404	0.168	0.762	0.005	0.039
6	14.0 - 16.0	14.996	2.653	0.387	0.196	0.783	0.006	0.036
7	16.0 - 18.0	16.978	2.670	0.368	0.233	0.804	0.006	0.031
8	18.0 - 20.0	18.966	2.573	0.345	0.271	0.814	0.007	0.028
9	20.0 - 23.5	21.547	2.245	0.323	0.333	0.845	0.008	0.028
						$R_{Kr}^{K^+}$		
1	4.0 - 6.0	5.278	1.951	0.582	0.327	0.856	0.031	0.025
2	6.0 - 8.0	7.145	2.135	0.502	0.232	0.852	0.018	0.025
3	8.0 - 10.0	9.097	2.343	0.444	0.192	0.836	0.013	0.024
4	10.0 - 12.0	11.02	2.559	0.408	0.178	0.865	0.011	0.025
5	12.0 - 14.0	13.000	2.735	0.392	0.195	0.883	0.011	0.025
6	14.0 - 16.0	14.973	2.826	0.388	0.225	0.886	0.012	0.025
7	16.0 - 18.0	16.980	2.838	0.375	0.264	0.908	0.014	0.026
8	18.0 - 20.0	18.953	2.683	0.365	0.314	0.912	0.017	0.026
9	20.0 - 23.5	21.528	2.370	0.347	0.382	0.937	0.019	0.027
						$R_{Kr}^{K^-}$		
1	4.0 - 6.0	5.333	1.898	0.535	0.279	0.694	0.054	0.020
2	6.0 - 8.0	7.164	2.084	0.446	0.185	0.651	0.026	0.018
3	8.0 - 10.0	9.113	2.293	0.385	0.159	0.691	0.019	0.020
4	10.0 - 12.0	11.047	2.454	0.356	0.154	0.748	0.017	0.021
5	12.0 - 14.0	12.996	2.529	0.344	0.165	0.772	0.016	0.022
6	14.0 - 16.0	14.988	2.652	0.345	0.195	0.773	0.017	0.022
7	16.0 - 18.0	16.961	2.668	0.348	0.233	0.810	0.020	0.023
8	18.0 - 20.0	18.959	2.535	0.338	0.281	0.815	0.023	0.023
9	20.0 - 23.5	21.555	2.204	0.326	0.347	0.873	0.025	0.025
						R_{Kr}^{p}		
1	4.0 - 6.0	5.191	2.031	0.569	0.236	0.806	0.018	0.025
2	6.0 - 8.0	7.073	2.183	0.470	0.162	0.863	0.014	0.026
3	8.0 - 10.0	9.044	2.365	0.434	0.152	0.909	0.013	0.026
4	10.0 - 12.0	11.025	2.558	0.416	0.171	0.941	0.013	0.027
5	12.0 - 14.0	13.013	2.712	0.407	0.197	0.988	0.013	0.029
6	14.0 - 16.0	14.986	2.828	0.392	0.235	1.020	0.014	0.032
7	16.0 - 18.0	16.981	2.804	0.381	0.281	1.075	0.017	0.035
8	18.0 - 20.0	18.961	2.684	0.365	0.335	1.109	0.022	0.037
9	20.0 - 23.5	21.541	2.329	0.341	0.400	1.123	0.025	0.036
						$R_{Kr}^{\bar{p}}$		
1	4.0 - 6.0	5.266	2.112	0.520	0.235	0.550	0.065	0.016
2	6.0 - 8.0	7.153	1.983	0.416	0.169	0.503	0.036	0.015
3	8.0 - 10.0	9.082	2.143	0.377	0.146	0.548	0.029	0.017
4	10.0 - 12.0	11.061	2.305	0.365	0.157	0.583	0.026	0.021
5	12.0 - 14.0	13.041	2.513	0.369	0.183	0.595	0.024	0.020
6	14.0 - 16.0	15.016	2.686	0.363	0.208	0.626	0.024	0.021
7	16.0 - 18.0	16.965	2.668	0.363	0.249	0.658	0.027	0.020
8	18.0 - 20.0	18.985	2.538	0.359	0.304	0.722	0.033	0.020
9	20.0 - 23.5	21.625	2.253	0.334	0.366	0.794	0.038	0.023

Table 4.1: Values of $R(\nu)$ of identified hadrons for Krypton, together with its statistical and systematic uncertainties, and the average values of ν, Q^2, z and p_t^2.

.

bin	z range	$\langle z \rangle$	$\langle \nu \rangle / GeV$	$\langle Q^2 \rangle / GeV^2$	$\langle p_T^2 \rangle / GeV^2$	$R_{Kr}^{\pi^+}$	Δ_{stat}	Δ_{sys}
1	0.0 - 0.1	0.095	22.228	2.141	0.062	0.945	0.033	0.029
2	0.1 - 0.2	0.155	18.317	2.593	0.104	0.879	0.004	0.031
3	0.2 - 0.3	0.247	15.892	2.781	0.163	0.816	0.003	0.030
4	0.3 - 0.4	0.345	14.762	2.815	0.217	0.782	0.004	0.027
5	0.4 - 0.5	0.446	14.305	2.784	0.260	0.759	0.005	0.024
6	0.5 - 0.6	0.546	13.982	2.749	0.287	0.739	0.006	0.022
7	0.6 - 0.7	0.646	13.685	2.664	0.296	0.722	0.007	0.022
8	0.7 - 0.8	0.746	12.827	2.572	0.260	0.676	0.009	0.022
9	0.8 - 0.9	0.845	11.838	2.420	0.210	0.627	0.010	0.030
10	0.9 - 1.2	0.952	10.712	2.443	0.170	0.544	0.012	0.023
						$R_{Kr}^{\pi^-}$		
1	0.0 - 0.1	0.095	22.215	2.140	0.060	0.899	0.032	0.029
2	0.1 - 0.2	0.155	18.404	2.569	0.103	0.863	0.004	0.042
3	0.2 - 0.3	0.246	16.028	2.710	0.166	0.805	0.004	0.041
4	0.3 - 0.4	0.345	14.837	2.742	0.221	0.774	0.004	0.034
5	0.4 - 0.5	0.445	14.329	2.733	0.260	0.745	0.006	0.027
6	0.5 - 0.6	0.546	13.939	2.658	0.280	0.743	0.007	0.026
7	0.6 - 0.7	0.646	13.575	2.562	0.273	0.727	0.009	0.026
8	0.7 - 0.8	0.746	12.820	2.420	0.228	0.700	0.010	0.032
9	0.8 - 0.9	0.845	11.844	2.282	0.169	0.684	0.012	0.054
10	0.9 - 1.2	0.953	10.781	2.268	0.137	0.579	0.014	0.037
						$R_{Kr}^{K^+}$		
1	0.0 - 0.1	0.096	22.539	1.994	0.055	0.998	0.125	0.029
2	0.1 - 0.2	0.157	18.535	2.514	0.123	1.056	0.011	0.032
3	0.2 - 0.3	0.247	15.456	2.735	0.184	0.986	0.010	0.029
4	0.3 - 0.4	0.346	14.335	2.818	0.236	0.906	0.010	0.026
5	0.4 - 0.5	0.446	13.974	2.857	0.276	0.848	0.011	0.024
6	0.5 - 0.6	0.546	13.812	2.851	0.310	0.822	0.013	0.023
7	0.6 - 0.7	0.645	13.675	2.904	0.344	0.787	0.016	0.022
8	0.7 - 0.8	0.745	12.826	2.799	0.332	0.761	0.019	0.022
9	0.8 - 0.9	0.844	11.963	2.752	0.286	0.688	0.024	0.019
10	0.9 - 1.2	0.948	11.165	2.634	0.234	0.645	0.034	0.018
						$R_{Kr}^{K^-}$		
1	0.0 - 0.1	0.096	22.628	1.913	0.056	0.907	0.142	0.027
2	0.1 - 0.2	0.156	18.646	2.493	0.115	0.883	0.012	0.025
3	0.2 - 0.3	0.245	15.704	2.686	0.174	0.823	0.011	0.024
4	0.3 - 0.4	0.344	14.717	2.720	0.227	0.783	0.013	0.022
5	0.4 - 0.5	0.444	14.398	2.633	0.265	0.760	0.017	0.022
6	0.5 - 0.6	0.544	14.244	2.548	0.298	0.709	0.020	0.020
7	0.6 - 0.7	0.643	14.538	2.572	0.330	0.673	0.029	0.020
8	0.7 - 0.8	0.740	13.826	2.501	0.332	0.637	0.042	0.018
9	0.8 - 0.9	0.841	13.309	2.512	0.226	0.632	0.070	0.020
10	0.9 - 1.2	0.949	12.886	2.381	0.140	0.670	0.146	0.034
						R_{Kr}^{p}		
1	0.0 - 0.1	-	-	-	-	-	-	-
2	0.1 - 0.2	0.186	19.855	2.186	0.114	1.045	0.034	0.032
3	0.2 - 0.3	0.254	15.919	2.566	0.173	1.138	0.012	0.033
4	0.3 - 0.4	0.347	13.842	2.830	0.219	1.034	0.010	0.029
5	0.4 - 0.5	0.445	13.513	2.949	0.273	0.943	0.011	0.027
6	0.5 - 0.6	0.544	13.425	2.982	0.317	0.872	0.014	0.025
7	0.6 - 0.7	0.643	13.117	2.940	0.336	0.788	0.018	0.023
8	0.7 - 0.8	0.743	12.013	2.881	0.338	0.728	0.025	0.021
9	0.8 - 0.9	0.843	11.143	2.826	0.340	0.689	0.038	0.020
10	0.9 - 1.2	0.958	9.962	2.859	0.333	0.600	0.052	0.017
						$R_{Kr}^{\bar{p}}$		
1	0.0 - 0.1	-	-	-	-	-	-	-
2	0.1 - 0.2	0.186	20.089	2.172	0.132	0.595	0.043	0.025
3	0.2 - 0.3	0.251	16.560	2.539	0.179	0.666	0.016	0.023
4	0.3 - 0.4	0.345	15.238	2.696	0.246	0.667	0.019	0.022
5	0.4 - 0.5	0.445	15.725	2.751	0.309	0.649	0.026	0.020
6	0.5 - 0.6	0.543	15.798	2.640	0.347	0.600	0.034	0.017
7	0.6 - 0.7	0.641	15.164	2.534	0.354	0.569	0.048	0.016
8	0.7 - 0.8	0.738	14.125	2.749	0.406	0.472	0.066	0.013
9	0.8 - 0.9	0.847	13.258	3.050	0.318	0.297	0.074	0.009
10	0.9 - 1.2	0.967	11.280	3.149	0.991	0.201	0.073	0.009

Table 4.2: Values of R(z)) of identified hadrons for Krypton, together with its statistical and systematic uncertainties, and the average values of n , Q^2, z *and* p_t^2.

bin	Q^2 range/GeV^2	$\langle Q^2 \rangle / GeV^2$	$\langle p_T^2 \rangle / GeV^2$	$\langle \nu \rangle / GeV$	$\langle z \rangle$	$R_{Kr}^{\pi^+}$	Δ_{stat}	Δ_{sys}
1	1.0 - 1.5	1.233	0.218	14.750	0.399	0.748	0.004	0.025
2	1.5 - 2.0	1.732	0.214	14.598	0.397	0.757	0.004	0.026
3	2.0 - 3.0	2.436	0.215	14.810	0.392	0.771	0.004	0.026
4	3.0 - 4.0	3.444	0.216	15.029	0.386	0.802	0.006	0.027
5	4.0 - 5.0	4.448	0.214	15.068	0.384	0.806	0.008	0.028
6	5.0 - 6.0	5.453	0.209	15.004	0.384	0.814	0.010	0.028
7	6.0 - 8.0	6.801	0.204	14.815	0.384	0.813	0.011	0.028
8	8.0 - 25.	9.448	0.192	14.640	0.393	0.791	0.017	0.028
						$R_{Kr}^{\pi^-}$		
1	1.0 - 1.5	1.231	0.215	14.837	0.399	0.741	0.004	0.032
2	1.5 - 2.0	1.729	0.209	14.705	0.393	0.762	0.005	0.034
3	2.0 - 3.0	2.432	0.211	14.959	0.384	0.771	0.005	0.035
4	3.0 - 4.0	3.440	0.210	15.105	0.377	0.798	0.007	0.036
5	4.0 - 5.0	4.446	0.208	15.142	0.374	0.802	0.009	0.036
6	5.0 - 6.0	5.449	0.207	15.150	0.375	0.817	0.012	0.037
7	6.0 - 8.0	6.798	0.201	14.825	0.374	0.824	0.013	0.038
8	8.0 - 25.	9.436	0.193	14.503	0.375	0.841	0.022	0.039
						$R_{Kr}^{K^+}$		
1	1.0 - 1.5	1.236	0.251	14.354	0.390	0.852	0.009	0.024
2	1.5 - 2.0	1.733	0.242	14.152	0.397	0.876	0.011	0.025
3	2.0 - 3.0	2.439	0.244	14.492	0.396	0.899	0.010	0.025
4	3.0 - 4.0	3.449	0.237	14.744	0.396	0.915	0.014	0.026
5	4.0 - 5.0	4.458	0.234	14.854	0.398	0.947	0.019	0.027
6	5.0 - 6.0	5.449	0.226	14.940	0.394	0.922	0.024	0.026
7	6.0 - 8.0	6.779	0.230	14.627	0.400	0.878	0.025	0.025
8	8.0 - 25.	9.483	0.197	14.531	0.411	0.803	0.036	0.023
						$R_{Kr}^{K^-}$		
1	1.0 - 1.5	1.233	0.226	14.998	0.354	0.762	0.013	0.022
2	1.5 - 2.0	1.732	0.222	14.916	0.353	0.777	0.016	0.022
3	2.0 - 3.0	2.435	0.217	15.156	0.351	0.791	0.015	0.022
4	3.0 - 4.0	3.445	0.211	15.219	0.345	0.774	0.020	0.022
5	4.0 - 5.0	4.450	0.213	15.286	0.338	0.807	0.029	0.023
6	5.0 - 6.0	5.445	0.207	15.120	0.339	0.809	0.038	0.023
7	6.0 - 8.0	6.772	0.202	14.821	0.339	0.756	0.040	0.021
8	8.0 - 25.	9.309	0.186	14.318	0.340	0.898	0.074	0.026
						R_{Kr}^{p}		
1	1.0 - 1.5	1.237	0.245	14.055	0.390	0.975	0.011	0.028
2	1.5 - 2.0	1.734	0.239	13.946	0.397	1.008	0.013	0.029
3	2.0 - 3.0	2.443	0.239	14.139	0.401	1.005	0.012	0.029
4	3.0 - 4.0	3.446	0.233	14.490	0.402	1.030	0.016	0.030
5	4.0 - 5.0	4.452	0.237	14.590	0.410	0.988	0.021	0.029
6	5.0 - 6.0	5.450	0.241	14.636	0.416	1.009	0.028	0.030
7	6.0 - 8.0	6.786	0.242	14.652	0.422	0.957	0.028	0.028
8	8.0 - 25.	9.450	0.244	14.519	0.449	0.916	0.043	0.027
						$R_{Kr}^{\bar{p}}$		
1	1.0 - 1.5	1.234	0.259	15.815	0.358	0.611	0.018	0.018
2	1.5 - 2.0	1.733	0.242	15.588	0.361	0.672	0.024	0.021
3	2.0 - 3.0	2.433	0.243	15.850	0.360	0.653	0.021	0.021
4	3.0 - 4.0	3.440	0.240	16.159	0.361	0.650	0.030	0.021
5	4.0 - 5.0	4.450	0.245	16.616	0.360	0.705	0.043	0.027
6	5.0 - 6.0	5.443	0.195	16.037	0.364	0.692	0.059	0.024
7	6.0 - 8.0	6.757	0.232	15.642	0.377	0.642	0.060	0.025
8	8.0 - 25.	9.294	0.278	15.336	0.428	0.662	0.112	0.020

Table 4.3: Values of $R(Q^2)$ of identified hadrons for Krypton, together with its statistical and systematic uncertainties, and the average values of n, Q^2, z and p_t^2.

bin	p_T^2 range/GeV^2	$\langle p_T^2 \rangle / GeV^2$	$\langle \nu \rangle / GeV$	$\langle Q^2 \rangle / GeV^2$	$\langle z \rangle$	$R_{Kr}^{\pi^+}$	Δ_{stat}	Δ_{sys}
1	0.00 - 0.05	0.023	13.049	2.694	0.388	0.739	0.004	0.021
2	0.05 - 0.10	0.073	14.106	2.773	0.399	0.743	0.005	0.022
3	0.10 - 0.30	0.182	15.212	2.751	0.400	0.771	0.003	0.028
4	0.30 - 0.50	0.384	16.061	2.779	0.419	0.796	0.006	0.024
5	0.50 - 0.70	0.585	16.575	2.802	0.455	0.833	0.010	0.025
6	0.70 - 0.90	0.787	16.755	2.800	0.489	0.877	0.016	0.026
7	0.90 - 1.10	0.987	17.155	2.766	0.522	0.895	0.024	0.026
8	1.10 - 1.40	1.226	17.381	2.836	0.544	0.918	0.031	0.027
9	1.40 - 1.95	1.606	17.664	2.813	0.569	1.094	0.050	0.031
10	1.95 - 5.00	2.410	18.389	2.784	0.596	1.240	0.104	0.036
						$R_{Kr}^{\pi^-}$		
1	0.00 - 0.05	0.023	13.071	2.647	0.388	0.727	0.004	0.021
2	0.05 - 0.10	0.073	14.110	2.691	0.398	0.763	0.005	0.025
3	0.10 - 0.30	0.182	15.358	2.687	0.392	0.765	0.004	0.036
4	0.30 - 0.50	0.383	16.312	2.694	0.401	0.796	0.007	0.026
5	0.50 - 0.70	0.585	16.791	2.707	0.428	0.835	0.011	0.027
6	0.70 - 0.90	0.786	17.118	2.692	0.460	0.871	0.018	0.027
7	0.90 - 1.10	0.987	17.285	2.719	0.488	0.886	0.027	0.027
8	1.10 - 1.40	1.224	17.585	2.697	0.520	0.978	0.038	0.029
9	1.40 - 1.95	1.607	17.948	2.646	0.536	1.072	0.056	0.032
10	1.95 - 5.00	2.428	18.616	2.708	0.591	1.160	0.111	0.034
						$R_{Kr}^{K^+}$		
1	0.00 - 0.05	0.022	13.083	2.804	0.379	0.833	0.009	0.024
2	0.05 - 0.10	0.073	14.005	2.864	0.395	0.834	0.012	0.024
3	0.10 - 0.30	0.186	14.635	2.762	0.403	0.887	0.008	0.025
4	0.30 - 0.50	0.385	15.137	2.768	0.427	0.932	0.013	0.027
5	0.50 - 0.70	0.586	15.642	2.891	0.467	0.938	0.020	0.028
6	0.70 - 0.90	0.787	16.075	2.876	0.500	0.942	0.031	0.030
7	0.90 - 1.10	0.988	16.517	2.890	0.525	1.029	0.047	0.029
8	1.10 - 1.40	1.225	17.000	2.774	0.554	1.050	0.057	0.032
9	1.40 - 1.95	1.602	17.177	2.837	0.571	1.231	0.090	0.035
10	1.95 - 5.00	2.405	18.269	2.730	0.583	1.407	0.188	0.041
						$R_{Kr}^{K^-}$		
1	0.00 - 0.05	0.023	13.461	2.673	0.343	0.728	0.013	0.021
2	0.05 - 0.10	0.073	14.509	2.653	0.352	0.762	0.017	0.022
3	0.10 - 0.30	0.186	15.318	2.620	0.349	0.795	0.012	0.023
4	0.30 - 0.50	0.384	16.044	2.681	0.367	0.800	0.019	0.023
5	0.50 - 0.70	0.582	16.860	2.685	0.405	0.811	0.031	0.023
6	0.70 - 0.90	0.787	17.318	2.588	0.433	0.855	0.049	0.024
7	0.90 - 1.10	0.984	17.930	2.609	0.471	0.924	0.079	0.026
8	1.10 - 1.40	1.229	17.769	2.830	0.478	0.913	0.096	0.030
9	1.40 - 1.95	1.614	18.350	2.489	0.506	0.878	0.132	0.027
10	1.95 - 5.00	2.373	19.163	1.997	0.568	1.115	0.285	0.078
						R_{Kr}^{p}		
1	0.00 - 0.05	0.023	12.334	2.667	0.387	0.938	0.010	0.027
2	0.05 - 0.10	0.073	13.188	2.852	0.405	0.955	0.013	0.028
3	0.10 - 0.30	0.183	14.456	2.870	0.420	0.953	0.009	0.028
4	0.30 - 0.50	0.386	15.685	2.837	0.440	1.052	0.016	0.032
5	0.50 - 0.70	0.587	16.312	2.822	0.466	1.183	0.028	0.039
6	0.70 - 0.90	0.789	16.444	2.910	0.488	1.273	0.044	0.045
7	0.90 - 1.10	0.986	16.716	2.826	0.508	1.385	0.070	0.055
8	1.10 - 1.40	1.223	16.694	2.823	0.525	1.511	0.096	0.048
9	1.40 - 1.95	1.622	16.858	2.950	0.559	1.868	0.165	0.074
10	1.95 - 5.00	2.423	17.611	2.874	0.585	2.250	0.338	0.076
						$R_{Kr}^{\bar{p}}$		
1	0.00 - 0.05	0.023	13.845	2.695	0.353	0.593	0.020	0.018
2	0.05 - 0.10	0.073	14.890	2.693	0.361	0.609	0.024	0.019
3	0.10 - 0.30	0.184	16.107	2.597	0.364	0.639	0.017	0.020
4	0.30 - 0.50	0.384	17.203	2.503	0.391	0.705	0.030	0.021
5	0.50 - 0.70	0.583	17.909	2.500	0.414	0.749	0.051	0.022
6	0.70 - 0.90	0.790	17.665	2.535	0.441	0.815	0.082	0.024
7	0.90 - 1.10	0.988	18.411	2.715	0.478	0.725	0.112	0.021
8	1.10 - 1.40	1.232	18.664	2.532	0.491	0.833	0.160	0.032
9	1.40 - 1.95	1.644	18.291	2.733	0.487	1.019	0.251	0.029
10	1.95 - 5.00	2.468	19.130	2.971	0.542	1.416	0.572	0.082

Table 4.4: Values of $R(p_t^2)$ of identified hadrons for Krypton, together with its statistical and systematic uncertainties, and the average values of n *, Q^2, z and p_t^2.*

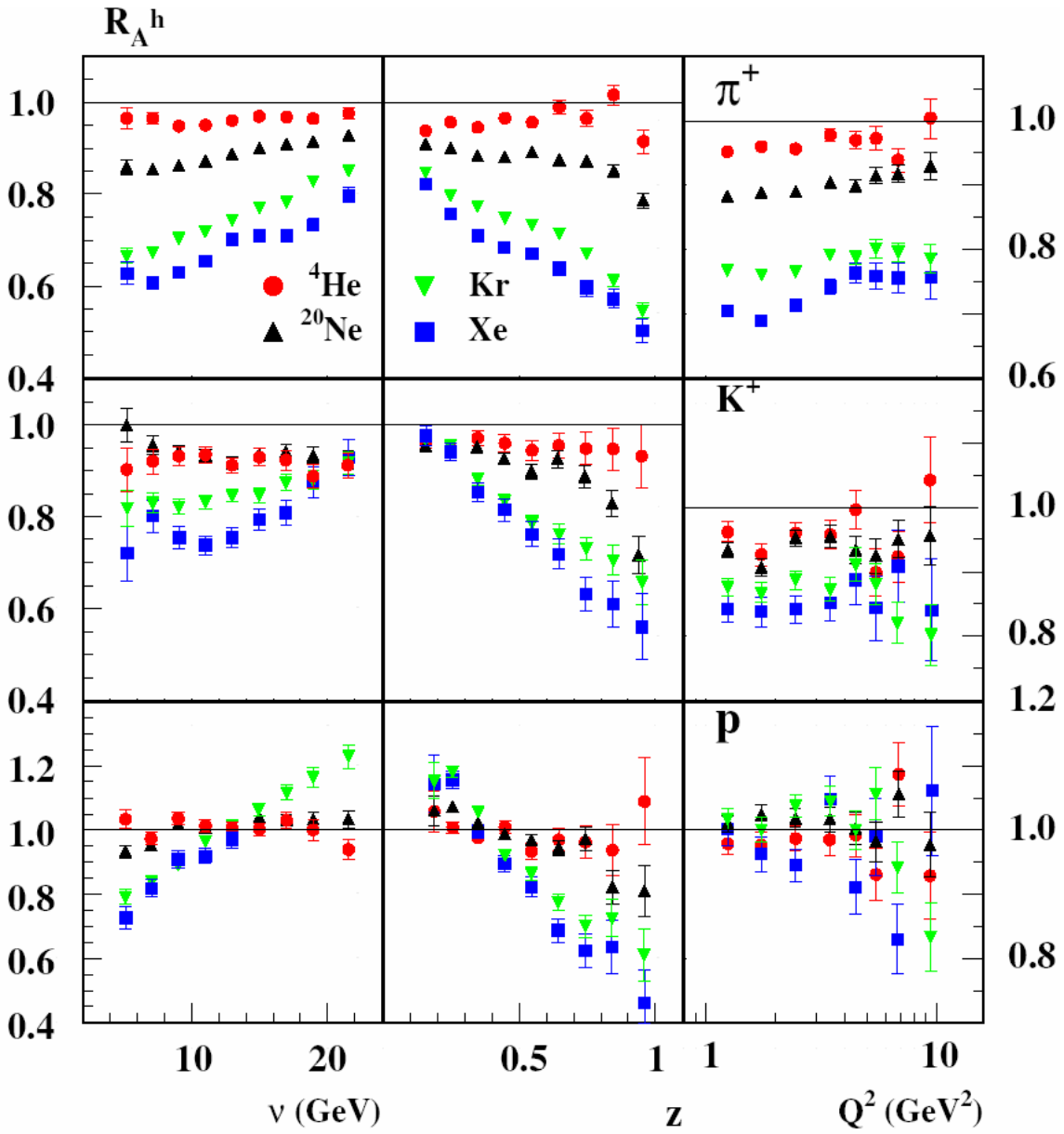

FIG. 4.5: Values of R_A^h for positively charged hadrons as a function of n , z and Q^2 for helium, neon, krypton and xenon.

4.1.1 n - dependence

The first systematic experimental studies of the n dependence of attenuation were reported in ref. [5], where the range 20 < n < 200 GeV) was investigated. It was shown that the nuclear

attenuation vanished at ν > 50 GeV. For that reason the HERMES data at much lower ν are expected to be most informative. The leftmost columns in Figs. 4.5, 4.6, 4.8 clearly show for all particles a positive slope for the ν -dependence of R_A^h, with the value of the slope (as well as the attenuation) increasing with the mass number A of the nucleus, being very small for Helium and sizeable for Xenon

In the absorption-type models this change of slope is explained as being due to an increase in the formation length in the rest frame of the nucleus at higher ν due to Lorentz dilatation, resulting in a larger fraction of the hadronization taking place outside the nucleus. In case of the energy-loss models the effective shift Δz that shifts the fragmentation function is proportional to ε / ν , with ε the quark energy loss.

The fact that for protons R_A^h increases with ν to well above unity is largely due to a change of $\langle z \rangle$ with ν . For example, the value of $\langle z \rangle$ for the lowerst ν -bin is about 0.57, whereas for the highest ν bin it is 0.35.

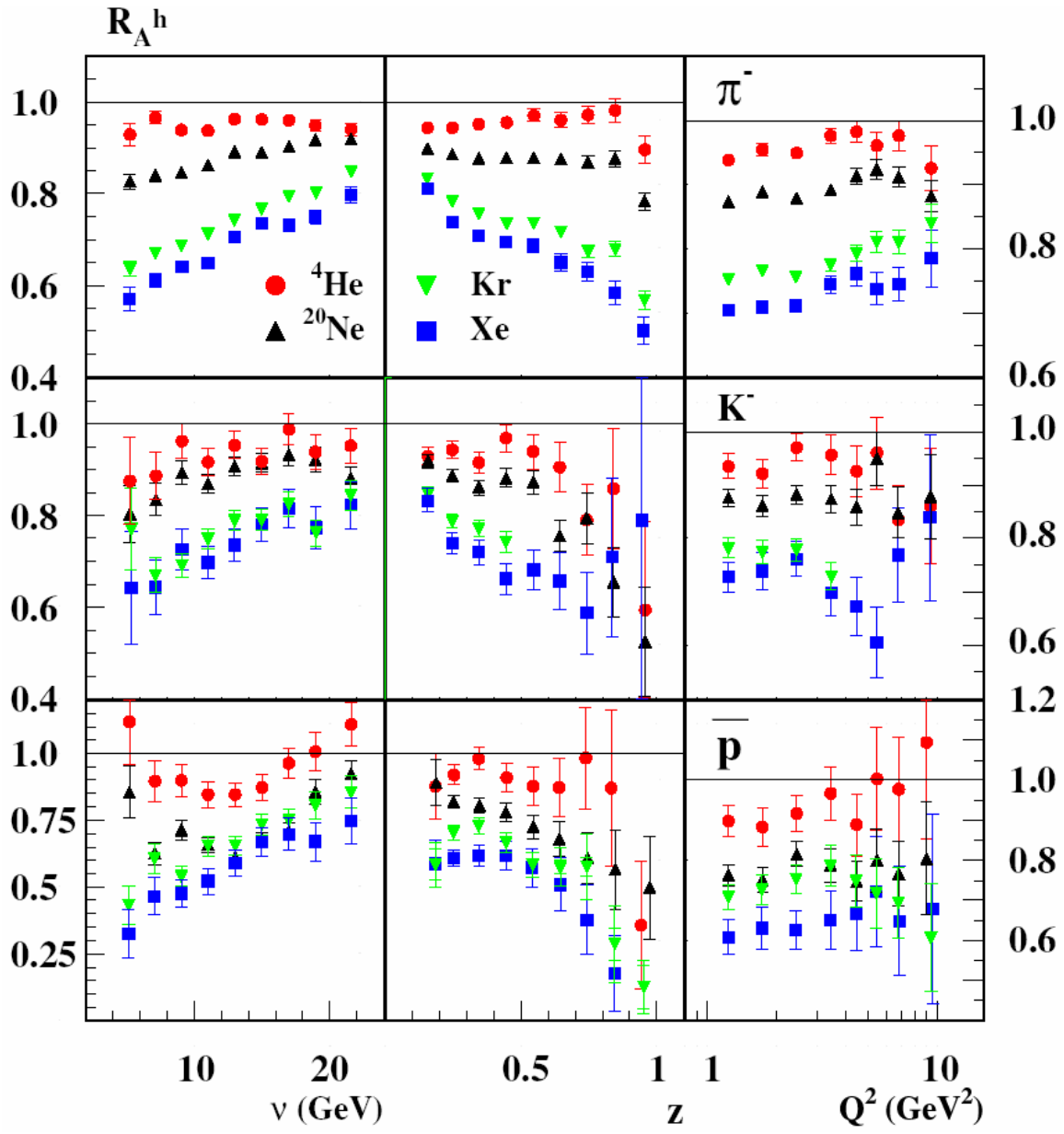

FIG. 4.6: Values of R_A^h for negatively charged hadrons as a function of ν, z and Q^2 for helium, neon, krypton and xenon.

4.1.2 z - dependence

As can be seen from the second column in Figs. 4.5, 4.6, 4.8 for all particles R_A^h decreases strongly with z for Xenon and Krypton, much less for Neon, whereas R_A^h seems to even increase slightly for Helium. In the energy-loss type models this is due to the strong decrease of the

fragmentation function at large z in combination with the Δz resulting from the energy loss. In absorption-type models the overall decrease of R_A^h with increasing z is assumed to be due to a decrease in the (pre-)hadron formation length in combination with (pre-)hadronic absorption.

For the heavier targets, R_A^h rises strongly at low z. In that region also the multiplicity, which is unity down to about z = 0.4, starts to rise. Presumably this is due to large re-scattering effects in the larger nuclei, where particles of higher energy loose energy by generating (other) lower energy particles. As in the case of the n dependence, the behavior of R_A^h for protons is special in that R_A^h gets even above unity, now at small z, presumably as a result of large re-scattering on protons in the target. In evaluating the value of R_A^h in detail, one has to take into account that the average value of n decreases considerably with z, from about 20 GeV for the lowest bin to about 10 GeV for the highest bin. This explains why even at the smallest z the value of R_A^h is still lower than for the highest value of n.

Apart from featuring rather small values of R_A^h (down to almost zero), the z dependence of R_A^h for antiprotons has a peculiar shape, unlike the one for all other particles, in that it decreases at low z for Krypton and Xenon. It was checked that this behaviur is not due to some artefact of the analysis, e.g., the particle identification. Perhaps it reflects the fact that at low z (as well as for high z) the value of L_C becomes small compared to the size of heavier nuclei in combination with the large *pN* cross section. The fact that such a behavior is not visible for other particles might be due to those particles being easily produced by re-scattering, especially at low z, whereas for antiprotons that is highly unlikely.

4.1.3 Q^2 - dependence

As it is seen from the third column of Figs. 4.5, 4.6, 4.8, a small Q^2 dependence is observed for pions, but hardly for kaons and protons, which seems stronger at higher A. Two-dimensional studies using charged pions (see the next subsection) have shown that while the magnitude of the attenuation for pions for each nucleus depends on n , z or p_t^2, the slope with Q^2 remains essentially the same for all bins. Hence, the fragmentation is not very sensitive to Q^2, which is important as it allows us to integrate over Q^2 when studying other dependences.

In the twist-four energy-loss model of Ref. [2, 20] a Q^2-dependence of R_A^h of the form: $R \sim a \ln Q^2$, which is globally consistent with the data. The authors of Ref. [48] have also made a prediction for the Q^2 dependence. In their case the observed Q^2 dependence is the result of two largely canceling processes. This yields a rather small Q^2 dependence, larger for Krypton than for Neon, in global agreement with the data. When describing the attenuation purely as the result of modification of the (effective) fragmentation function [17] due to energy loss, a slight increase of R_A^h with Q^2 is predicted. In the deconfinement model [21] a slight decrease of R_A^h with Q^2 is predicted, which depends weakly on *A*.

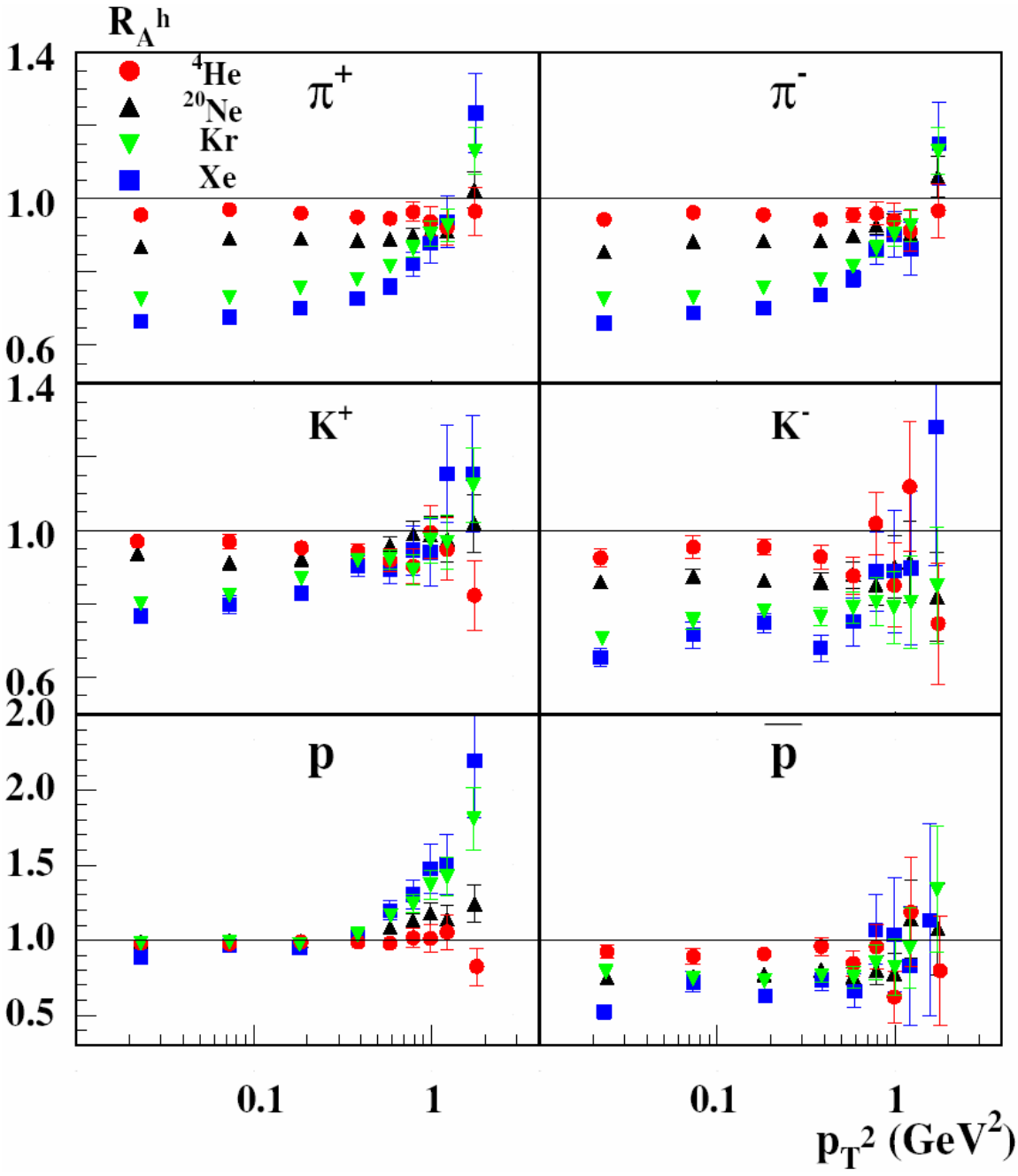

FIG. 4.7: Values of R_A^h for positively (left panel) and negatively (right panel) charged hadrons as a function of p_t^2 for helium, neon, krypton and xenon.

4.1.4 p_t^2 - dependence

Figure 4.7 and the rightmost column of Figure 4.8 shows for the heavier nuclei a rise of R_A^h at high p_t^2, which is an indication of the p_t^2 broadening due to re-scattering. This effect was first observed by EMC [5], and is also known from heavy ion collisions, where it is referred to as the Cronin effect [49]. It is thought to reject p_t^2 broadening due to partonic re-scattering (see also below when discussing the *z*-dependence of the effect for pions).

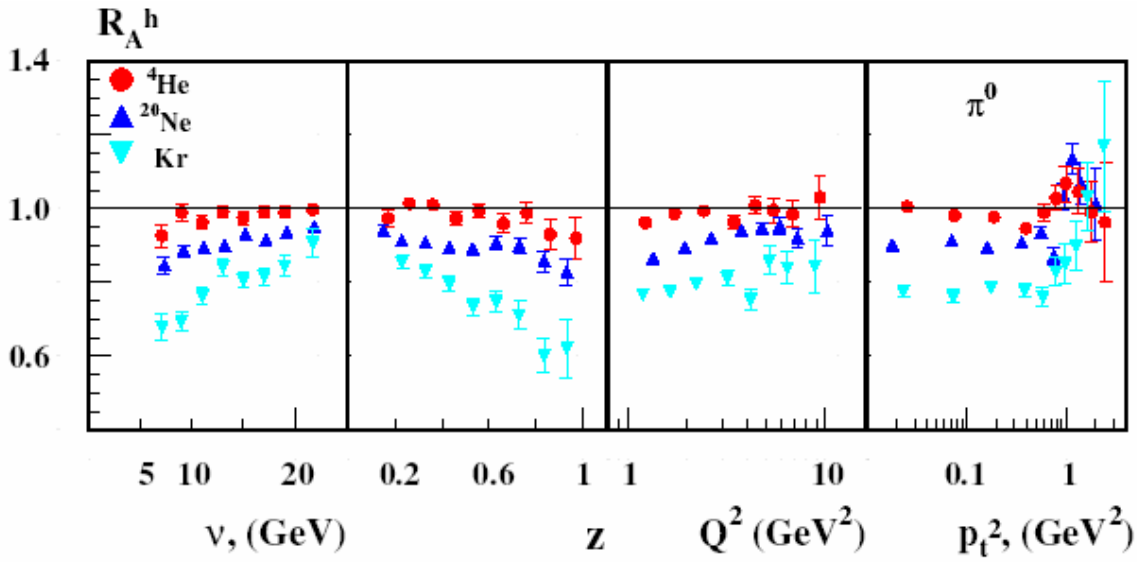

Fig. 4.8: Values of R_A^h for neutral pions as a function of ν, *z*, Q^2 *and* p_t^2 *for helium, neon, krypton and xenon.*

4.2 Two-dimensional results

In order to be able to investigate the behavior of R_A^h in more detail, the data for p^+ and p^- production, which have the best statistics, and are the same within their error bars, have been combined, so that a two-dimensional binning is possible, see Figures 4.9, 4.10,4.11. The bins were used as follows: 6.0-12.0-17.0-23.5 for n, 0.2-0.4-0.7-1.2 for z, and smaller or larger than 0.7 (GeV/c)2 for p_t^2. Fig. 4.9 indicates that the positive slope with n is present for all z, although its value (as well that of R_A^h) depends slightly on z. Within the uncertainties of the data the Q^2 dependence is the same for the different z-bins, so the dependence on z is not influenced when integrating over Q^2. Also the increase of R_A^h at large values of p_t^2 seems to start at about the same value for all z.

The data in the rightmost column indicate that the value of p_t^2 where R_A^h starts to rise strongly, is larger for larger z. A z-dependence of the p_t^2 dependence was predicted in Ref. [23].

The (red) points for the highest z range show a peculiar behavior at small values of p_t^2. This is due to a relatively large contribution of pions coming from r^0 decay in this part of phase space. Also the (less obvious) rise of R_A^h at the lowest Q^2 for this z range is related to the abovementioned.

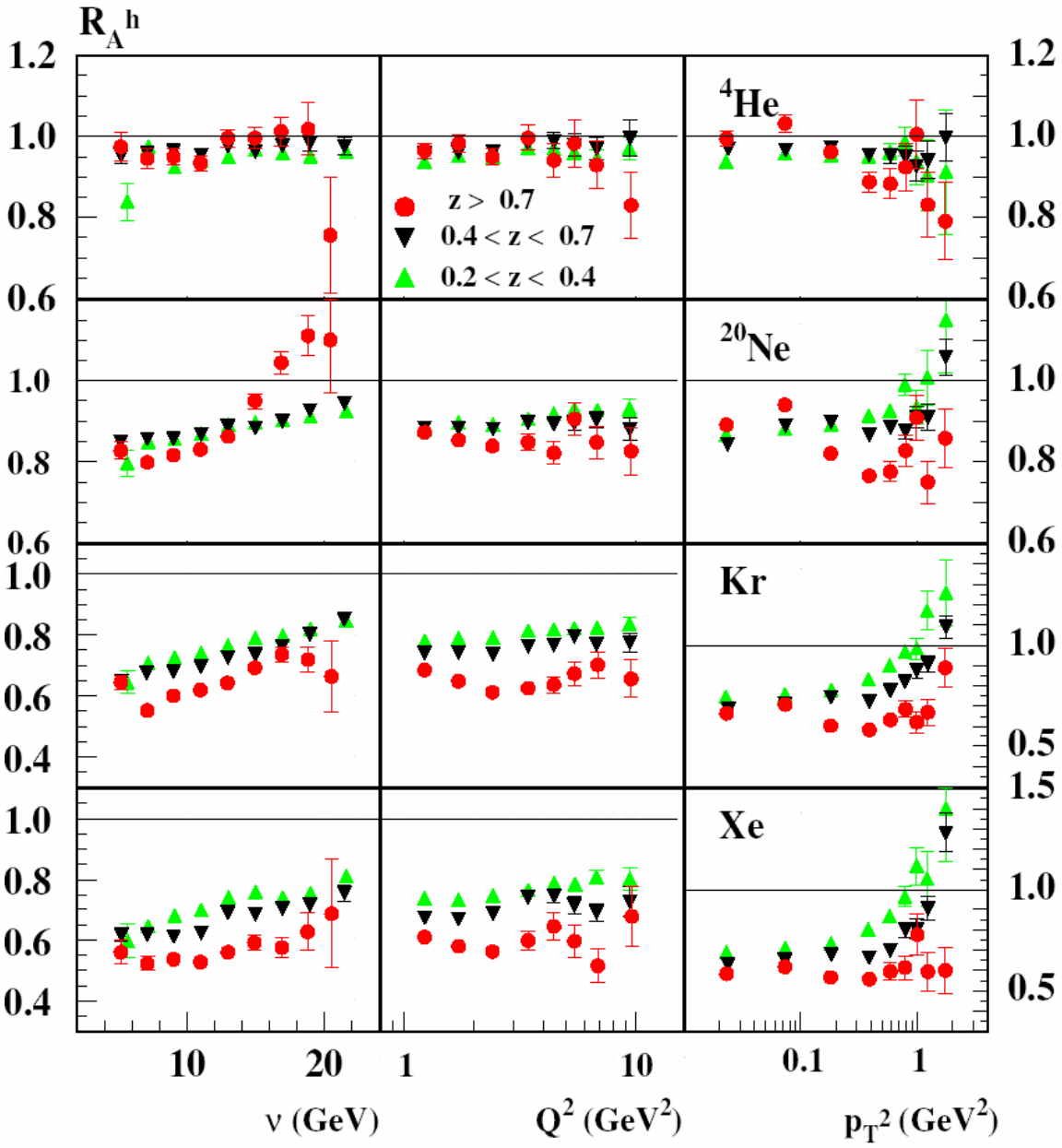

FIG. 4.9: Values of R_A^h for charged pions for all targets for three different z ranges.

The second and third column of Fig. 4.10 indicate that apart from differences in the absolute value of R_A^h, the dependence on Q^2 and p_t^2 is about the same for all n, which as mentioned in the previous section allows one to integrate over them without introducing spurious correlations. However, the leftmost column shows some interesting features in that for Helium and Neon (and perhaps for Krypton) there seems to be a change of the z dependence with the value of n, R_A^h

being about constant at low z and then dropping, the drop occurring at lower z for the lower n bin. Having in mind the notion of a formation length (compare Eqn. (1.23), which yields a value for L_C of about 5 fm for z = 0.6 and n = 15 GeV) one could speculate that the n at part of the z dependence reflects a partonic mechanism, the fall-off at larger z and/or lower n being the result of hadronic (absorption) mechanisms. Detailed calculations including both mechanisms are needed to substantiate any ideas about this. It is clear that these detailed data for a set of nuclei of different size, form a very sensitive test of any calculation of attenuation in nuclei. The A dependence of R_A^h and what can be learned from that will be discussed in a later subsection.

The leftmost column of Fig. 4.11 shows that the values of R_A^h are larger at large p_t^2. Also the dependence on n largely disappears there. This is clearly correlated with the fact that R_A^h increases at large p_t^2 (Cronin effect), as discussed in a previous subsection, and indicates that this effect is largely independent of n. The rightmost column of this figure shows that the Cronin effect disappears at high z. This is in agreement with the predictions of Ref. [23], that the effect should disappear for $z \to 1$ because in that limit the parton is not allowed any energy loss, so there is no room for partonic re-scattering.

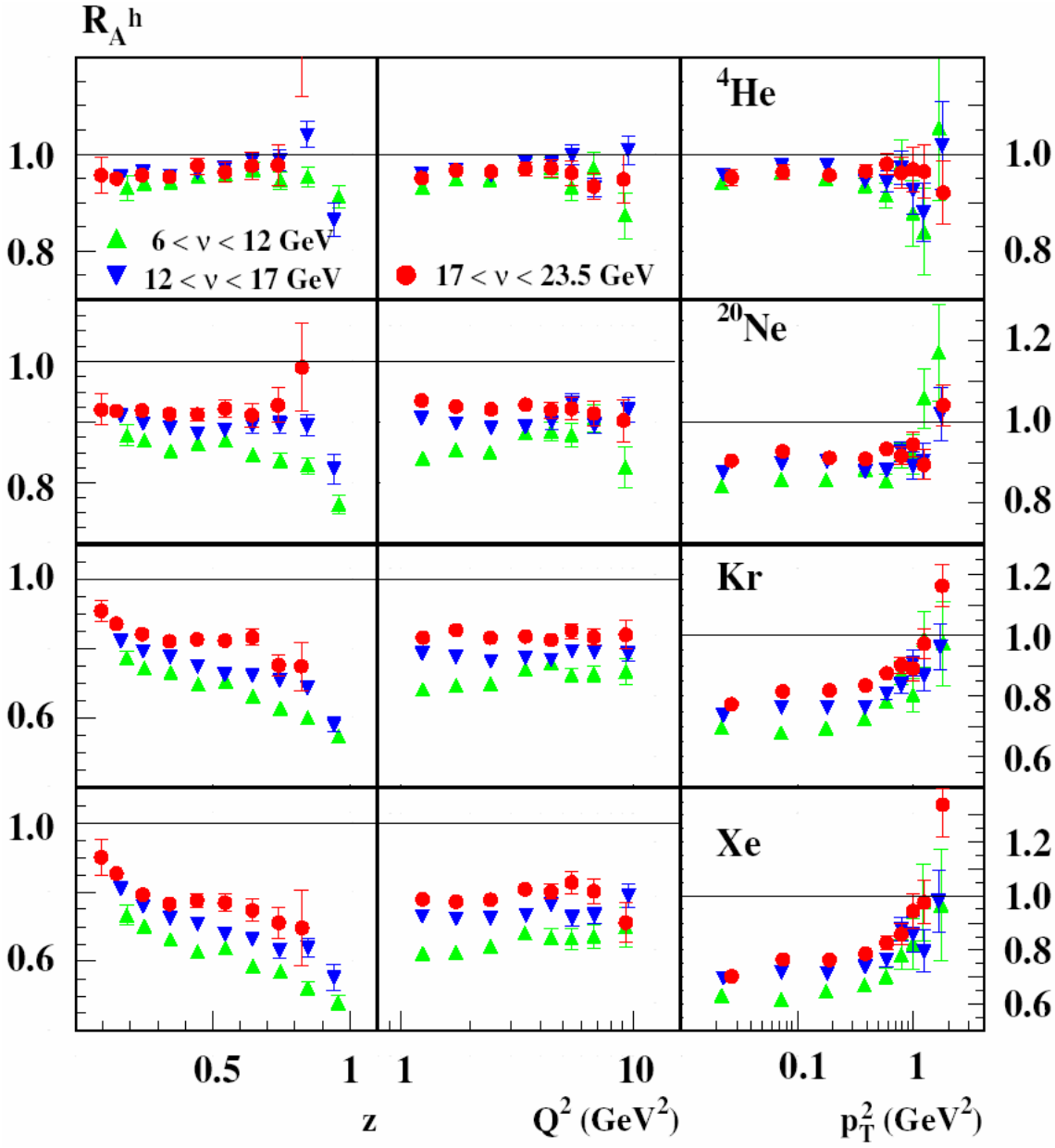

Figure 4.10: Values of R_A^h for charged pions for all targets for three different ν ranges.

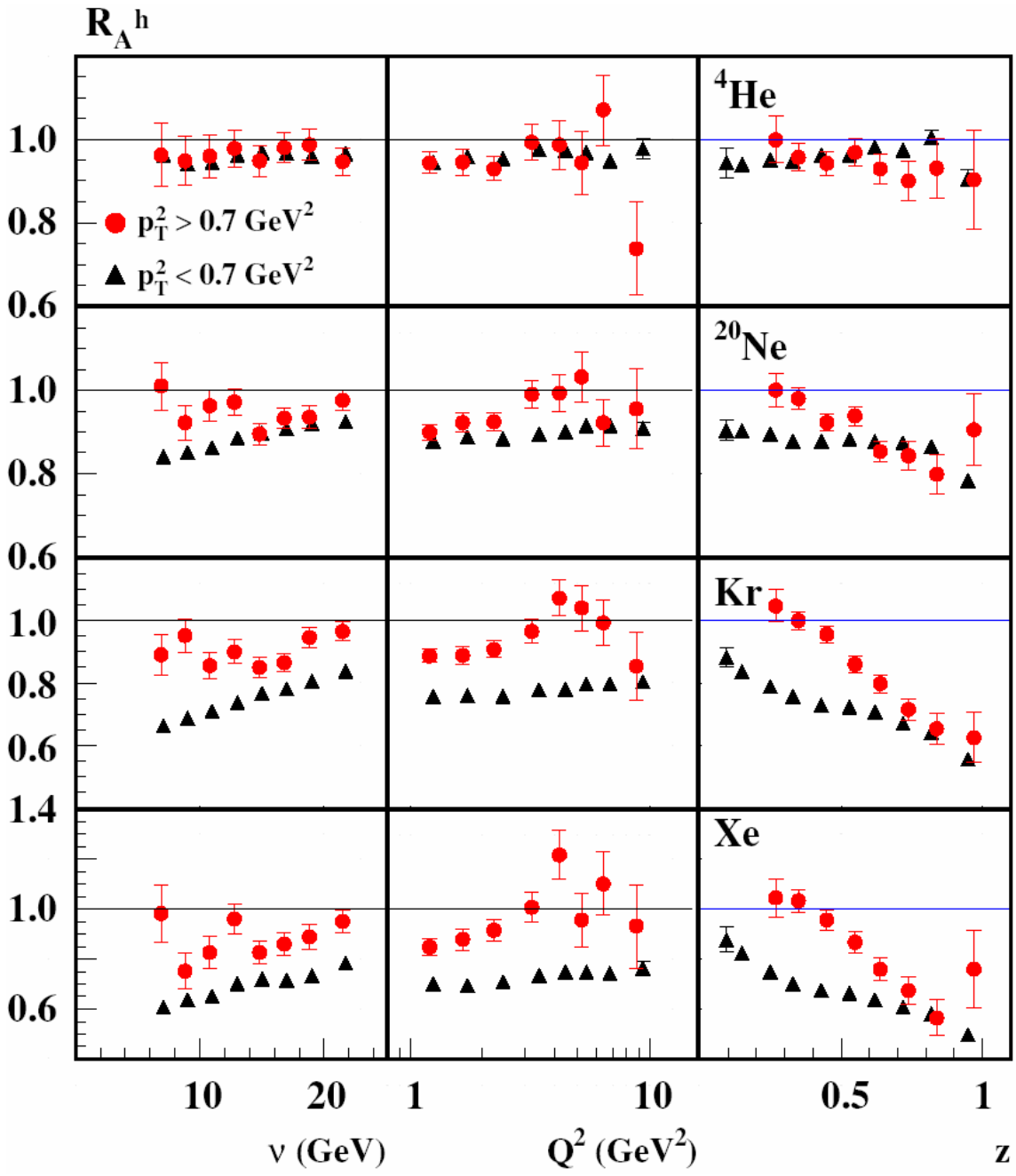

Figure. 4.11: Values of R_A^h for charged pions for all targets for two different p_t^2 ranges.

4.2.1 Dependence of R_A^h on the formation length

Based on the ideas how hadronization proceeds in time (see e.g. Lund type descriptions as used in Refs. [21, 24]), one can argue that the concept of a formation length, which in all models is a combination of n and z, is a better 'first' parameter to describe R_A^h than either n or z separately.

In order to investigate this, the values of R_A^h for the different n , z combinations in Fig. 4.10 for the four nuclei are plotted in Fig 4.12 against L_C, using as estimate for L_C Eq. 2 with k = 1 GeV/fm.

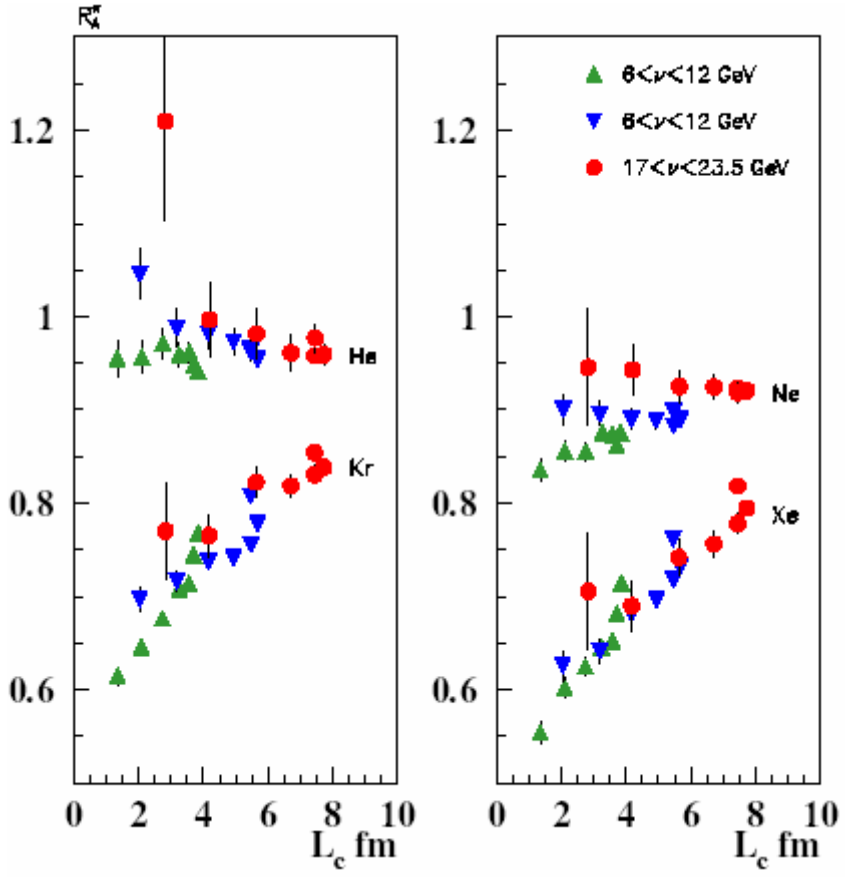

Figure 4.12: Values of $R_A^p(n,z)$ for He, Kr (left panel), and Ne, Xe(right panel) as a function of the formation lenth L_C as given by Eq. 1.23. The value of z for the points with the same symbol decreases from left to right.

As one can note, there is a distinct correlation between the values of R_A^h and L_C, most of the the variation of R_A^h with n or z in Figs. 4.9 and 4.10 now appearing as a variation with L_C. However, even if most of the variation in Figs. 4.9 and 4.10 is eliminated by L_C, for a given value of L_C there is still some spread, i.e., variation with the value of n . Especially the points for the lowest two z values (the rightmost in the sequence of same symbols), which are at about the same value of L_C, do not have the same value of R_A^h. Most probably this is due to large re-scattering

effects in the lowest z bin (note the relatively strong rise of R_A^h at low z in Figs. 4.5 and 4.6). The origin of the residual dependence of R_A^h on the value of n at the higher values of z is not so clear, but one should not forget that the formation length L_C is an *average*, the actual formation lengths for the various events being distributed over some range around this value. Also one could question if this picture of string breaking can be applied *quantitatively* for the present values of n, where after all there is only enough energy to produce a few particles. Nevertheless it is clear that the attenuation as represented by the value of R_A^h is mainly determined by a combination of n and z.

The leftmost column of Fig. 4.11 shows that the increase of R_A^h with n disappears at large values of p_t^2. This is clearly correlated with the fact that R_A^h increases at large p_t^2 (Cronin effect), as discussed in the previous subsection. The rightmost column of this figure indicates that the effect is only substantial at low z. This would be in agreement with the predictions of ref. [48], that the effect should disappear for $z \to 1$ because L_C goes to zero.

4.3 A-dependence

Because of the wide range of different nuclear targets at Hermes, and the good particle identification over a large range of momenta provided by the RICH detector, we are in the unique position to study the A dependence of hadronization for different final-state particles. Before presenting the results, some remarks should be made about how to fit the A- dependence and what conclusions could be drawn from it.

The data were fitted in a phenomenological way by using as fit function

$$R_A^p = \exp\left[-b\,(A/100)^a\right]. \qquad (4.1)$$

The scale factor of 100 is introduced to reduce the correlation between a and b and to make the value of b more representative of the attenuation in a nucleus. For moderate values of $b\,A^a$ this is equivalent to using $1 - R_A^h = b\,A^a$, a parameterization that has been used before [7], but the present

form has the advantage that R_A^h does not become non-physical for very large values of A. However, since R_A^h is the ratio of the multiplicity in nucleus A vs. the multiplicity in the deuteron, this fit function is internally inconsistent, unless one assumes no attenuation in D. One could use the A- dependence of Eq. 4.1 for the *hadron multiplicity* on nucleus A, which would lead to a formula for R_A^h of the form

$$R_A^h = \exp\left[-b\,(A^a - D^a)\right], \qquad (4.2)$$

where D represents the effective value of A for the attenuation in the deuteron. Assuming that the attenuation depends on the (average) density times the radius of the nucleus one finds [26] for this effective A a value of about 0.6, because the deuteron is such a loosely bound system. The influence of such a value on the value of a obtained using Eq. 4.2 is small (about -0.07), so all subsequent results are based on Eq. 4.2, but in drawing a possible conclusions one should remember that the real value of a is slightly lower.

A second remark concerns what A dependence is expected to be given some model for the mechanism. As already mentioned in section 2 the attenuation in the energy-loss model of ref. [25] is given as $1-R_A \sim L^2 \sim A^{2/3}$, whereas in (Glauber type) absorption models it is often presumed that $1-R_A \sim L^2 \sim A^{1/3}$. However, these estimates are too simple. First of all, by taking $L^2 \sim A^{1/3}$ one assumes the nucleus to be a rigid sphere or of a Gaussian shape, which is certainly not a good approximation. Taking realistic values for the nucleus matter distribution yields [26] effective values of L^2 that are globally proportional to $A^{0.74}$. Furthermore, it has been demonstrated already in Ref. [21] that inclusion of a distribution for the formation length L_C in absorption calculations increases the exponent above the value of 1/3, yielding values for a nucleus described as a rigid sphere for $1-R_A$ that approximately follow an $A^{2/3}$ pattern for large values of L_C. Using realistic matter distributions one finds for L_C = 0; 2; 4 fm, correspondingly, an $A^{0.40,0.54,0.60}$ behavior [26].

Thus, in principle it would be possible to discriminate between such a quark energy loss mechanism and an absorption mechanism by looking at the A- dependence when selecting small values of L_C.

Before presenting and discussing the results some remarks should be made about the uncertainty in the fitted values of a. The systematic uncertainty in the values of R is largely a scale uncertainty. The influence of this on the value of a was found to be about 0.05. The statistical uncertainty was directly used in the fit, and gives the corresponding uncertainty of a shown in the figures. In most cases the value of chi-squared is around unity, but in some cases the description of the values of R for the four nuclei was not very good, indicating that the A-dependence is more complicated than can be described with one exponential. Finally it should be kept in mind that including attenuation in deuterium will lower the value of a (by about 0.07 according to our estimate).

4.3.1 A-dependence results for pions

For detailed studies of the A- dependence, the most statistically supported pion data sample was used and observed as a function of n and z, using again the data (binned in both z and n) shown in Figs. 4.9 and 4.10. The results for a and b as functions of n for three z- bins are shown in Fig. 4.13. The behavior of b is smooth and rejects the dependence of the attenuation on n and z. The value of a is within uncertainties independent of n, but slightly dependent on z, changing from about 0.5 for the low z-bin to about 0.6 for the higher. (The points for the highest z-range should be viewed with caution, since they may be influenced by contributions from the decay of the r_0). The results for n = 6-8 GeV are slightly irregular, but there the fits are not very good in terms of large values of chi-squared.

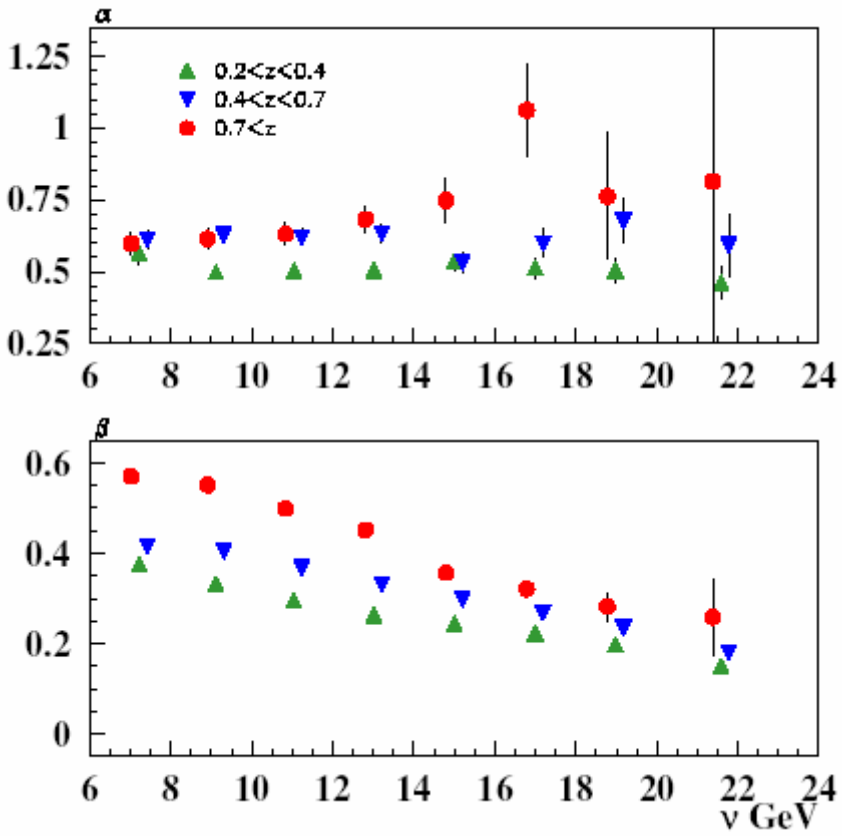

FIG 4.13: The n dependence of the parameters a and b (see Eq. 4) for three different z bins, using the combined sample of charged pions. Points slightly offset for better visibility.

Results for a and b as functions of z for three n bins are shown in Fig. 4.14. Once again, the values of b reflect the global behavior of R (more attenuation at higher z and lower n). There is an increase of a from about 0.5 to 0.6 with z and possibly at higher z a slight increase with n. However, in the latter region the results may be influenced by contributions from the decay of the r_0. The results for the highest z-bin do not follow the pattern of the lower z-bins. This is due to the behavior of R for Helium and Neon, seen in Fig. 4.10. As mentioned before, if those values are real, and not a statistical fluctuation, this could result from the formation length becoming so small that even in helium and neon hadronic mechanisms start to become important.

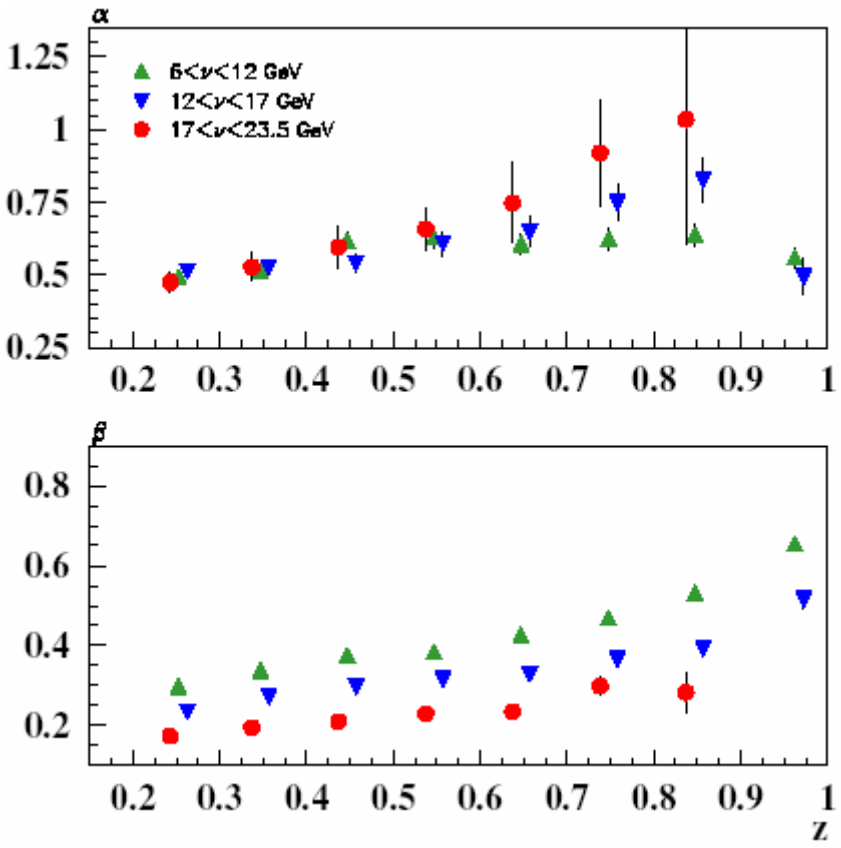

FIG. 4.14: The z dependence of the parameters a and b (see Eq. 4) for three different n bins, using the combined sample of charged pions. Points slightly offset for better visibility.

Given these results for separate n and z dependences it has also been investigated how a and b depend on the value of L_C. For that purpose the data have been binned in eight L_C bins, using the values of n and z of each event in Eqn. (1.10<L_c expression>). In order to avoid possible contributions of the r_0 at high z and large re-scattering effects at low z only data with $0.3< z<0.7$ were used. The resulting values of R are shown in Fig. 4.15, and the corresponding values of a and b - in Fig. 4.16. The behavior of b reflects what can be observed already in Fig. 4.15 for the heavier nuclei. Consistent with what has already been found above, the value of a decreases from about 0.6 at small L_C to less than 0.5 at large L_C. This behavior is not due to the cuts applied, so should be considered to be a real effect.

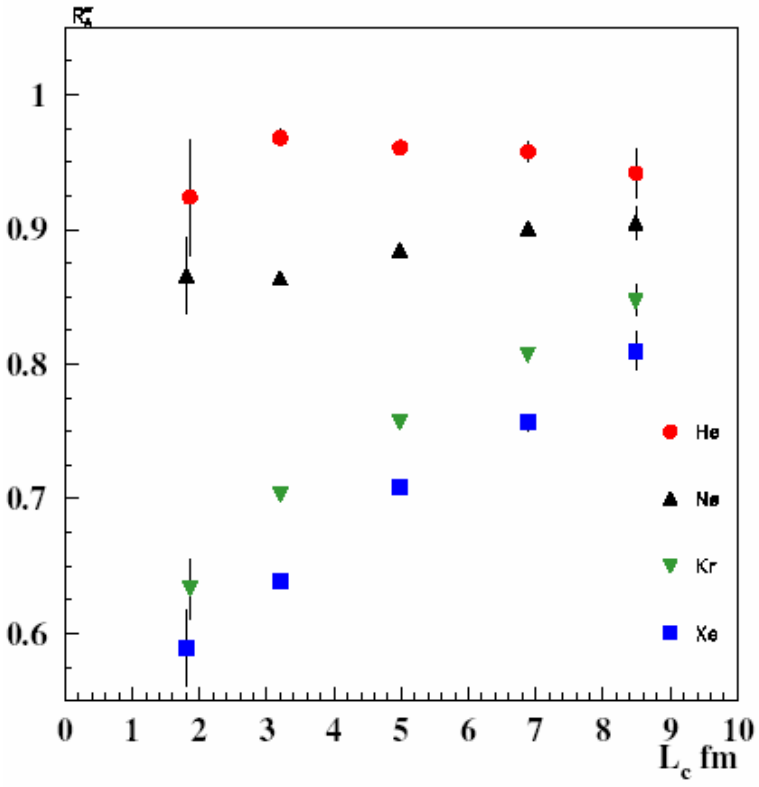

FIG. 4.15: Values of R_A^p for He, Ne, Kr and Xe as a function of the formation length L_C, as given by Eq. 2. This figure is for the case when R is binned in L_C for $0.3 < z < 0.7$.

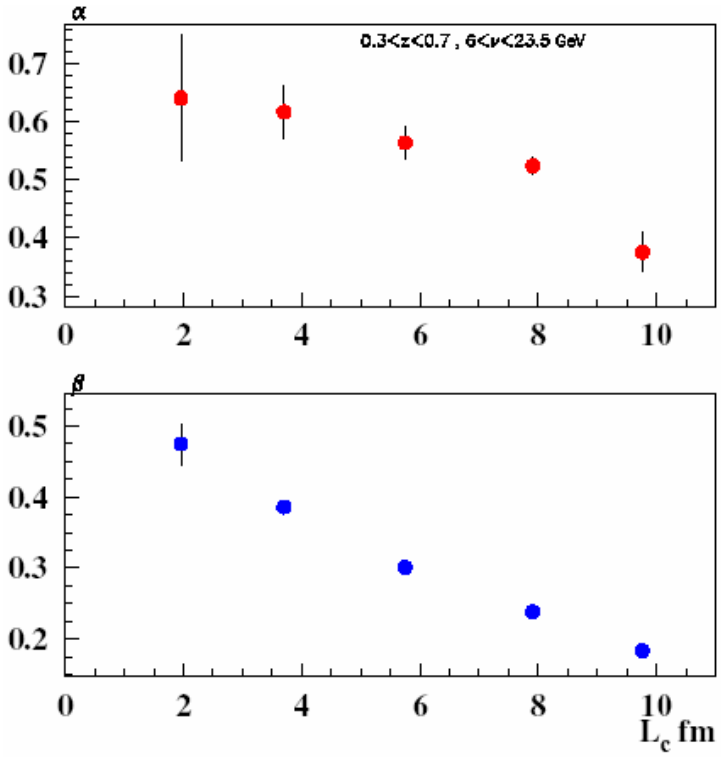

Figure 4.16: The dependence of the parameters a and b on the value of L_C for $0.3 < z < 0.7$.

Assuming that (perhaps not perfectly, but at least approximately) the value of L_C is indicative of the average distance scale where hadronization occurs, so that partonic effects are most prominent at large values of L_C*, this leads to some tentative conclusions. First of all the decrease of a with L_C seems to rule out the mechanism of Refs. [2,19] and [17], since those would give a value of a to be even above 2/3 [26]. (The fact that the Q2 dependence of R discussed before did not show an $A^{2/3}$ dependence suggests the same conclusion). Instead this decrease of a would indicate that a possible partonic mechanism should have an A- dependence with an exponent well below 0.5. In fact the model of Ref. [21] has a value of a for the partonic part of about 0.25. It does not seem possible to draw firm conclusions about the A-dependence of a (pre)hadronic absorption type mechanism. As demonstrated in refs. [21, 26] a pure absorption mechanism would yield a value of a that increases with L_C. Possibly such an increase is more than compensated for by an increasing influence of the partonic mechanism.

To estimate the systematic errors for the obtained values of a the systematic uncertainties ΔR_{sys} for the values of R_A^h (Tables 4.1, 4.2) were taken into account. The central values for the R_A^h used in the A-dependence fit procedure were shifted by the values of it's average systematic error, and the fit has been performed with the values of $R_A^h + \Delta R_{sys} = R_{sys}^{up}$. And $R_A^h - \Delta R_{sys} = R_{sys}^{down}$. The results of these studies are shown in Figure 4.17(a, b, c) for the central, up and down input values for R_A^h, respectively. The systematic uncertainties for a were then calculated as half of the difference between these two instances for a^{up} and a^{down}, and resulting uncertainty after the fit procedure is on the level of 10-15% depending on the L_c bin in which a was extracted.

* Here one should note that the average distance that a created parton travels through a nucleus (assuming it is not absorbed) is only 3/4R, with R the radius of that nucleus, because the virtual photon can interact anywhere in a nucleus. This means that even for Krypton with a radius of about 5 fm, hadronic mechanisms get small when $L_C > 4$ fm.

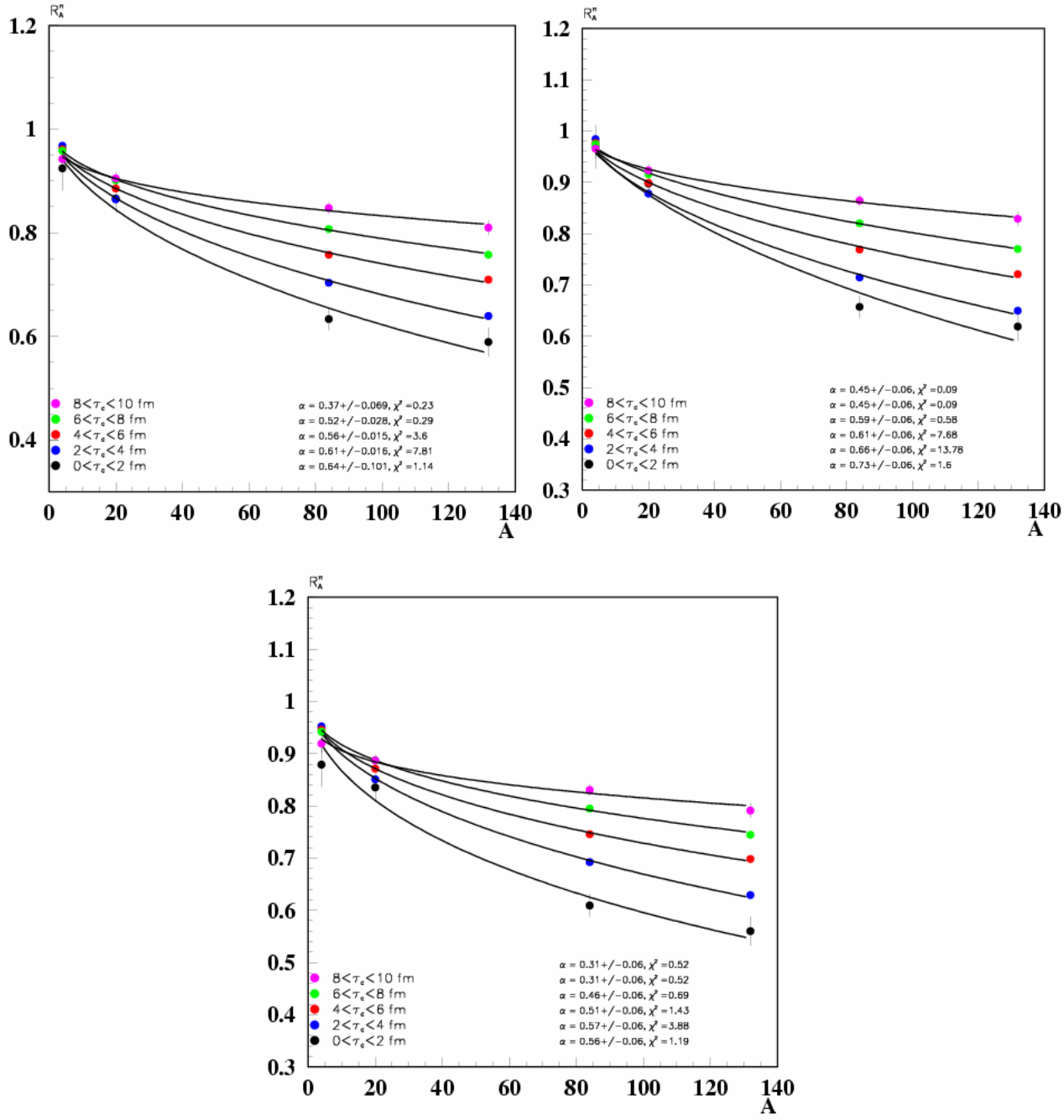

Figure 4.17 (a,b,c): Values of A-dependence of the R_A^h for central, up and down values as explained in the text.

Another part of these studies were aimed to estimate the influence of the fitting function (4.1) and (4.2) on values of a and b with and without taking into account the normalization on Deutron. Figures 4.18(a,b,c,d) shows the A-dependence of R_A^h for different fitting functions, while the corresponding plots for a and b are shown in Figure 4.19.

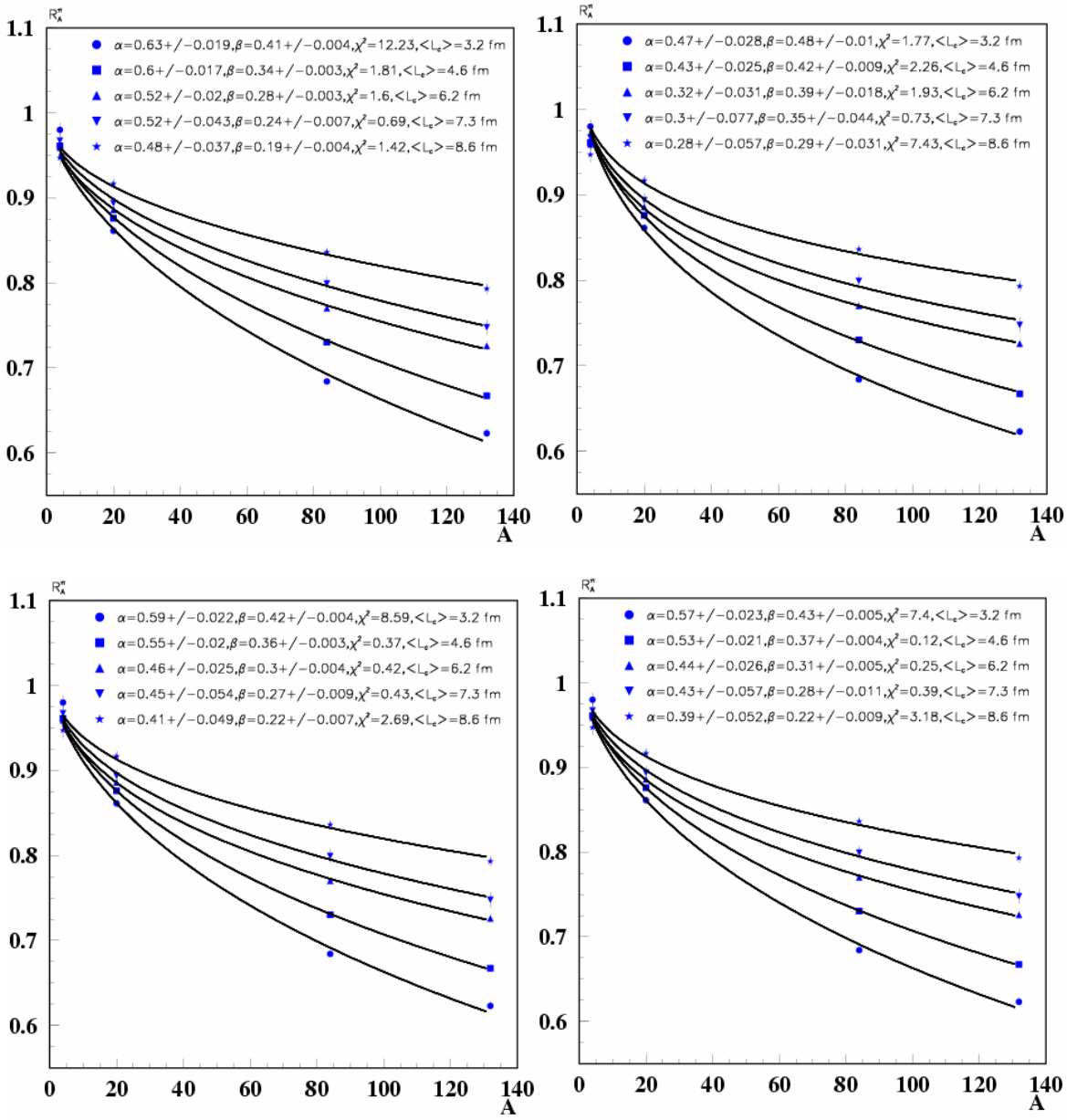

Figure 4.18: A-dependence of R_A^h for different types of fitting functions

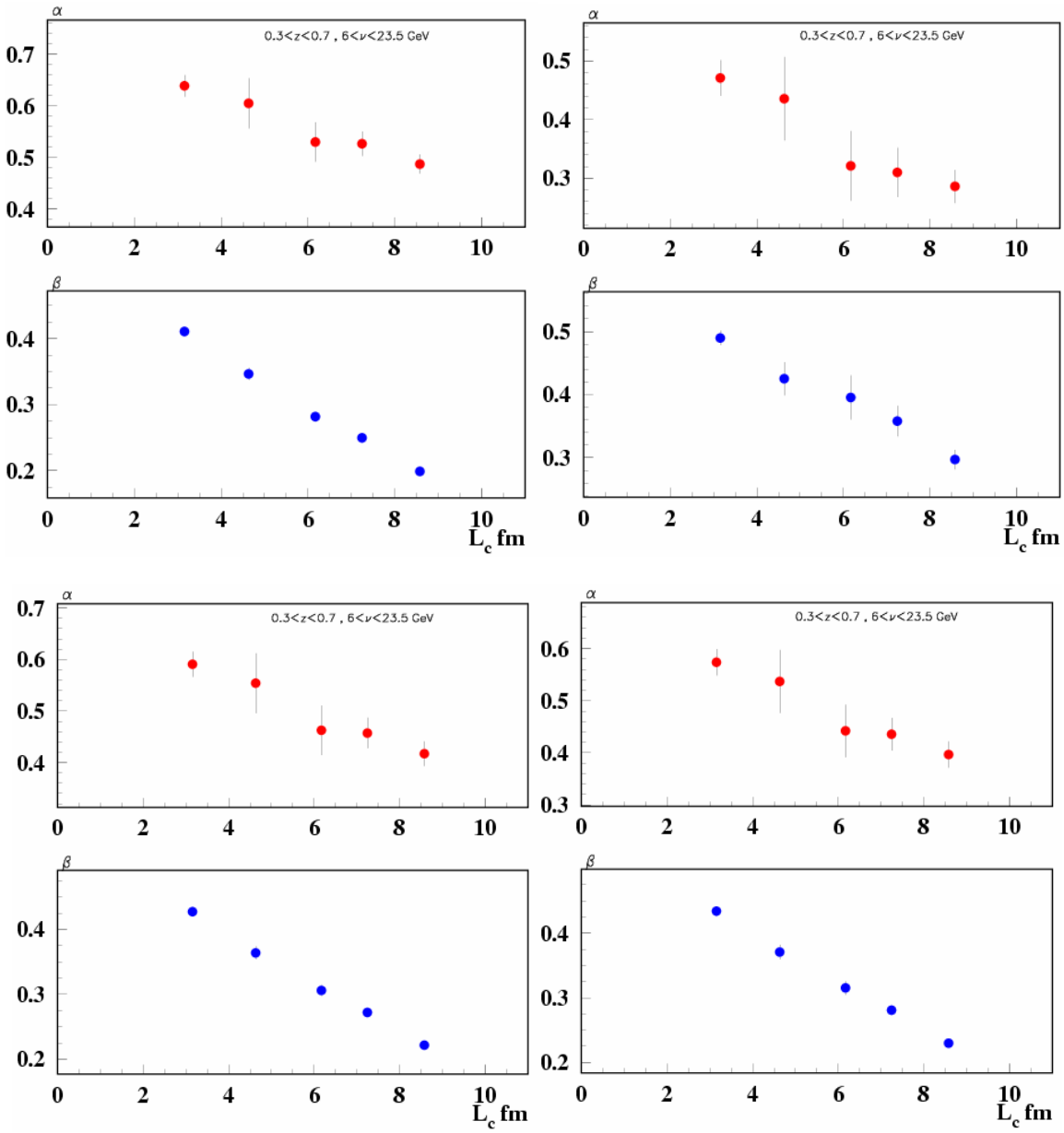

Figure 4.19 (a,b,c,d): Values of a *and* b *corresponding to Fig. 4.18.*

For this studies the binning over L_C defined as:

$$L_c = \frac{n}{k} z^{0.35} (1 - z)$$

was chosen to be as follows: `0 - 3.6 - 5.2 - 6.8 - 7.4 - 10 (fm)` to provide more or less equal statistics in each bin. Fig. 4.18(a) shows the result of the fit done with the basic fitting function (4.1); the real atomic mass number for deuteron was used for the fitting function (4.2) for the results are shown in Fig. 4.18(b). If the effective atomic mass number for deuteron (see section 4.3) is set to be equal to 0.4 for the fitting function (4.2), the *A*-dependence looks like shown in Fig.

4.18(c). And finally, a more realistic value for atomic mass number for deuteron equal to 0.6 corresponds to the results shown in Fig. 4.18(d). One can see that based on the obtained reduced c^2 values there is an indication that the normalization on Deuteron in form of (4.2) is the one that should be used, also the effective atomic mass number for Deuteron is close to 0.6. Comparing the results obtained from these detailed studies and the results shown in Fig. 4.16 done with different binning over the L_C, the main conclusion is that the values of a and b weekly depend on the binning, and keep the prominent behavior whereas a increases with decreasing L_C. In order to assign realistic errors for the obtained values of a and b one can use the values of the reduced c^2 and make the inflation of errors as:

$$\Delta a_{\text{inf}} = \Delta a \, sqrt(c^2)$$

4.3.2 A-dependence for other particles

For the other particles the statistics does not allow for a two-dimensional binning and study of the A dependence, so there the A dependence is presented for n-bins of 6.0-12.0-17.0-23.5 GeV/c (integrated over all z), and for z-bins of 0.2-0.4-0.7-1.2 (integrated over all n). For comparison the values for p^+ and p^- in the same bins are given as well. The results are shown in Fig. 4.20.

The only prominent (beyond the statistical and systematic uncertainties) feature that should be mentioned is the different behavior seen for K^+ particles at high n and low z. This may be due to large re-scattering effects, suggested by the data at low z in Fig. 4.5. K^- behaves differently from K^+, more like p^-, but a is smaller.

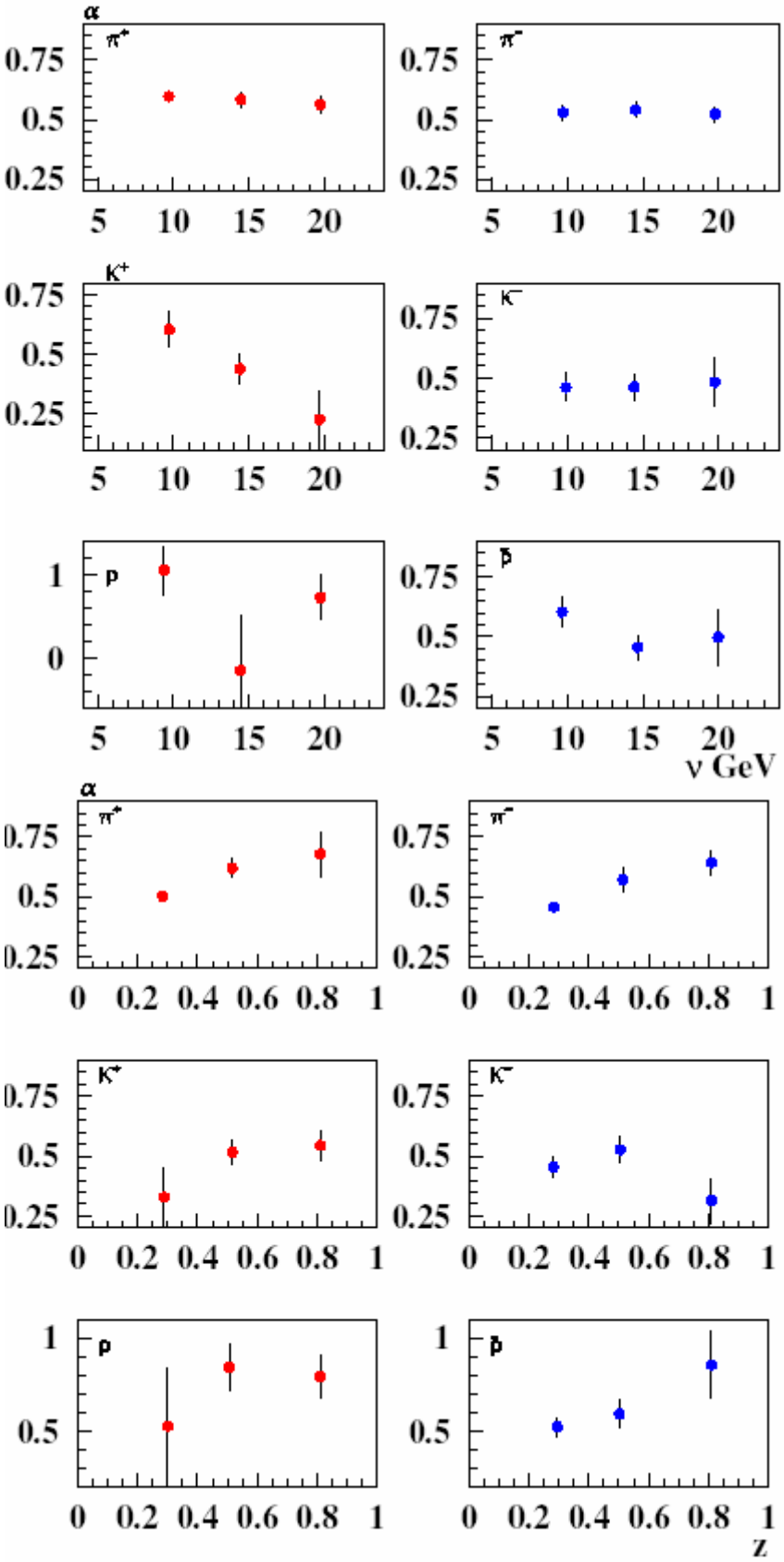

Figure 4.20: The extracted values of the parameter α, done in three different ν ranges for pions, kaons and protons (upper six panels), and in three different z ranges (lower six panels).

4.4 Double-hadron attenuation

Despite the accurate experimental data from single-hadron leptoproduction presented in previous sections, the underlying mechanisms in theoretical models for hadronization in the nuclear medium differ greatly. Double-hadron production offers an additional was to study hadronization. If the partonic energy loss of the struck quark were the only mechanism involved, it would be naively expected that the attenuation effect does not strongly depend on the number of hadrons involved, and the double-hadron to single-hadron ratio for a nuclear target should only be slightly dependent on the mass number A. On the other hand, if the final hadron absorption was the dominant process, the requirement of an additional slower sub-leading hadron that is more absorbed would suppress the two-hadron yield from heavier nuclei [2, 50], so that this ratio would decrease with A.

Measurement of double-hadron leptoproduction on Nitrogen, Krypton and Xenon relative to Deuterium has been performed, for all charged hadrons and neutral pions [51]. The SIDIS scattering data are presented in terms of the ratio:

$$R_{2h}(z_2) = \frac{\left(\frac{dN^{z_1>0.5}(z_2)/dz_2}{N^{z_1>0.5}} \right)_A}{\left(\frac{dN^{z_1>0.5}(z_2)/dz_2}{N^{z_1>0.5}} \right)_D} \qquad (4.3)$$

The values z_1 and z_2 correspond to the leading (largest z) and sub-leading (second largest z) hadrons, respectively. The quantity $dN^{z_1>0.5}$ is the number of events with at least two detected hadrons in a bin of width dz_2 at z_2 with z_1>0.5. The quantity $N^{z_1>0.5}$ is the number of events with at least one detected hadron with z_1>0.5. Labels $A(D)$ indicate that the term is calculated for the given nuclear and deuterium target. In addition to the previously discussed cuts, a more restrictive cut on n >7 GeV has been used to limit the kinematical correlations.

Since the leading hadron is selected with z_1>0.5, one expects it to contain the struck quark with high probability. No explicit constraints were applied to z_2. Both z_1 and z_2 were calculated assuming that all hadrons have the mass of the pion.

Two methods of double-hadron event selection were used. Selection I contrains only the combinations of hadron charges (leading-subleading) ++, --, +0, 0+, -0, 0-, 00. This suppresses the contributions from the $r^0 \to p^+ p^-$ decay because the +- and -+ combinations are missing. Fig. 4.21 shows the double ratio R_{2h} as a function of z_2 for Selection I. The kinematic variables are in the range $\langle n \rangle$=21 to 16 GeV and $\langle Q^2 \rangle$=2.1 to 2.6 GeV^2 as z_2 goes from 0.09 to 0.44. The averages over z_2 are $\langle n \rangle$=17.7 GeV and $\langle Q^2 \rangle$=2.4 GeV^2.

The ratio R_{2h} is generally below unity with no significant difference between the three nuclei. These data clearly show that the nuclear effect in the double-hadron ratio is much smaller than for the single-hadron attenuation measured under similar kinematic conditions. For z_2 <0.1, where R_{2h} rises towards and possibly above 1, the slow hadrons originate largely from target fragmentation.

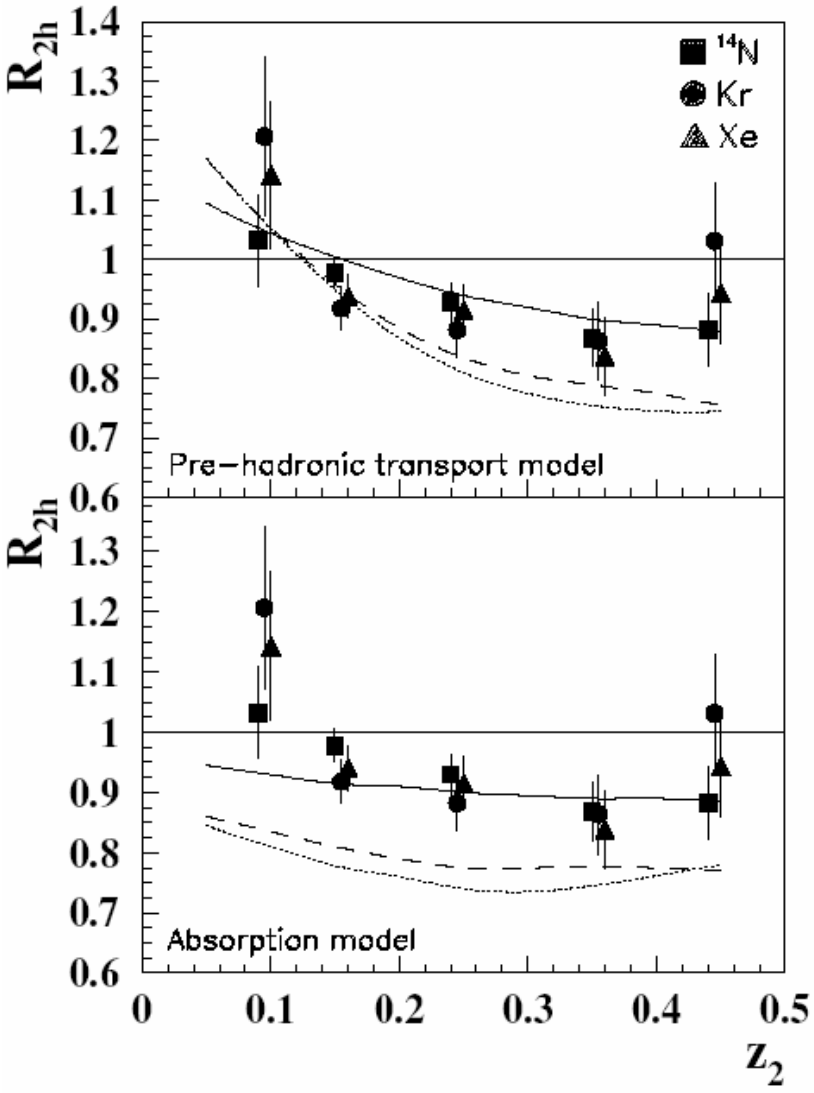

Figure 4.21: The ratio R_{2h} as a function of z_2 for Nitrogern (squares), Krypton (circles) and Xenon (triangles) with z_1>0.5. Selection I is considered. The systematic uncertainty is 2% for all the targets. In the upper panel the curves are calculated within a BUU transport model [24,52]. In the bottom panel the data are shown with calculations that assume only absorption for the three nuclei.

Also for z_2>0.4, where the two hadrons have close energies, R_{2h} seems to rise towards unity. The upper panel of Fig. 4.21 shows calculations based on a PYTHIA event generator with a fully coupled-channel treatment of the final-state interactions by means of a BUU transport model [24,52]. In this model, the fragmentation function is modified by pre-hadron interactions and re-scattering in the medium. Although the general trend of the data is reproduced, the model predicts an effect twice as large for Xenon and Krypton as for Nitrogen above z_2>0.1, which is not

supported by the data. Bottom panel of the same Figure shows the data compared to a calculation with a purely absorptive treatment of the interaction of the pre-hadronic or the final hadronic states.

Figure 4.22 presents the R_{2h} calculated for all hadron charge combinations (Selection II). Inclusion of the +- and -+ pairs does not change the value of R_{2h} significantly, contrary to all of the naïve space-time evolutionary models of hadronization.

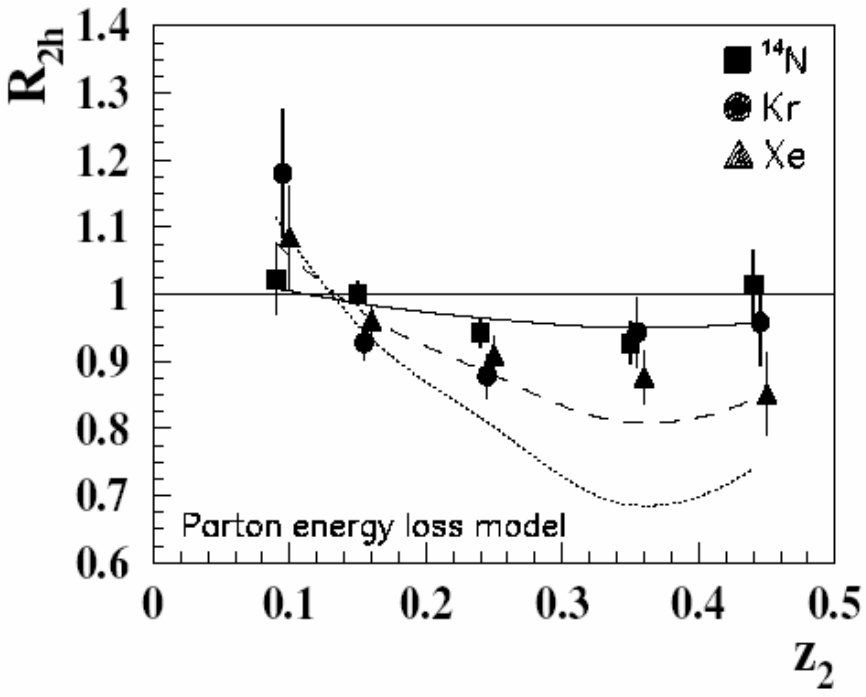

Fig 4.22: The ratio R_{2h} as a function of z_2 for Nitrogen (squares), Krypton (circles) and Xenon (triangles) with $z_1 > 0.5$ for Selection II.

Overall, the double-hadron production provides an effective tool to fine-tune the different contributions of processes to the fragmentation. The data do not seem to support the naïve expectations for pre-hadronic and hadronic final state interactions that are purely absorptive. Models that interpret modifications to fragmentation as being due to pre-hadronic scattering or partonic energy loss are also not completely consistent with the data.

4.5 Improved Two-Scale Model

4.5.1 Introduction

As it has already been mentioned before, studies of the hadron production in deep inelastic semi-inclusive lepton–nucleus scattering (SIDIS) offer a possibility to investigate the quark (string, color dipole) propagation in dense nuclear matter and the space-time evolution of the hadronization process. It is well known from QCD that confinement forbids the existence of an isolated color charge (quark, antiquark, etc.). Consequently, it is clear that after the deep inelastic scattering (DIS) of a lepton on the intra-nuclear nucleon, a complicated colorless pre-hadronic system arises. Its propagation in the nuclear environment involves processes like multiple interactions with the surrounding medium and induced gluon radiation. If the final hadron is formed inside the nucleus, it can interact via the relevant hadronic cross section, causing further reduction of the hadron yield [53]. QCD at present cannot describe the process of quark hadronization because of the major role of "soft" interactions. Therefore, the understanding of quark hadronization is of basic importance for the development of QCD. For this purpose the nuclear attenuation (NA) is investigated [14]. The experimentally measured observable is given by expression (1.22). The one-dimensional data sets are used from the ones presented in previous sections, which assumes that integration is done over all other kinematic variables.

Presently, there are numerous phenomenological models on the market for the investigation of the NA [2,5,10,11,12,13,17,21,24,48,50,54,55]. In this work, the two-scale model (TSM) [5] and its improved version (ITSM) [14] are used to perform a fit to the results on nuclear multiplicity ratios presented in previous sections and in [3, 8]. For the fit procedure the high-statistics and therefore the more precise part of the data sample is used, which includes data for the n and z dependences of NA for p+ and p- mesons on two nuclear targets (Nitrogen and Krypton). The n and z dependences of NA for p^0, K+, K-, and antiproton, produced on the Krypton target, are described with best values of the parameters obtained from the abovementioned fit. Then, the set of

parameters is used also for the prediction of the n , z, and Q^2 dependences of NA for the data from the Xenon target.

4.5.2 The two-scale model

The TSM is a string model which was proposed by EMC [5] and used for the description of their experimental data. The basic formula is:

$$R_A = 2p \int_0^\infty bdb \int_{-\infty}^\infty dx\, r(b,x) \times \left[1 - \int_x^\infty dx' s^{str}(\Delta x)\, r(b,x') \right]^{A-1} \qquad (4.4)$$

where b is the impact parameter, x the longitudinal coordinate of the DIS point, $?(b, x)$ the nuclear density function, x' the longitudinal coordinate of the string–nucleon interaction point, $s^{str}(\Delta x)$ the string–nucleon cross section on a distance $\Delta x = x' - x$ from the DIS point, and A the atomic mass number.

The string models are based on the idea that after DIS the knocked-out (anti)quark does not leave the nucleon remnant, and forms a string (color dipole) with the (anti)quark on the fast and the nucleon remnant on the slow end, while the color string itself consists of gluons. Its longitudinal size must be larger than the transverse size, but cannot be essentially larger than the hadronic size because of confinement. The string can then break down into two strings according to the following scenarios. First, when the quark–antiquark pair from the color field of the string is produced; and second, when the color interaction between the string and the nucleon (lying on its trajectory) has occurred (see for instance [18]). In the "history" of the string there are two time scales which are of interest to us. These are the time scales connected with the production of the first constituent (anti)quark of the final hadron and the interaction of two constituents for the first time.

As it has been mentioned above, the model contains two scales (see Fig. 4.23): t_c (l_c) the constituent formation time (length)*; and t_h (l_h) the yo-yo formation time (length). The yo-yo

* In relativistic units ($\hbar = c = 1$, where $\hbar = 2p$ is the reduced Planck constant and c the speed of light) $t_i = l_i$, i = c,h because partons and hadrons move with near-light speeds.

formation means that a colorless system with valence content and quantum numbers of the final hadron is formed, but without its "sea" partons.

In the two-dimensional string models which satisfy the following conditions: (a) quark–antiquark pairs arising from the vacuum do not have energy; (b) energy loss of the leading quark on unit length (string tension) is constant (a widely known example is the Lund model), there is a simple connection between t_h and t_c:

$$t_h - t_c = zn / k \qquad (4.5)$$

where k is the string tension (string constant). In further two different expressions for t_c will be used. The first expression for t_c is obtained for hadrons containing a leading quark [56]:

$$t_c = (1-z)n / k \qquad (4.6)$$

The color string fully spends its energy on a distance of $L = n / k$. beginning from the DIS point (see Fig. 4.23). The last hadron produced from the string is $h = H_1$, which contains a leading quark and carries energy E_h. At distance L, the energy of the leading quark becomes equal to zero and the whole energy of the hadron is concentrated in another constituent. This constituent collects its energy from the string and will have energy E_h on a distance L only if it was produced on a distance $E_h / k = zn / k$ from L. This is reflected in (4.6). It is important to note that the hadron produced on the fast end of string is not always necessarily the fastest hadron. The second expression for the average value of t_c used in this paper was obtained in [9,12] in the framework of the standard Lund model [23]:

$$t_c = \int_0^\infty l dl D_c(L, z, l) / \int_0^\infty dl D_c(L, z, l) \qquad (4.7)$$

where $D_c(L, z, l)$ is the distribution of the constituent formation length l of hadrons carrying momentum z. This distribution is

$$D_c(L, z, l) = L(1+C)\frac{l^C}{(l+zL)^{C+1}} \times \left(d(l - L + zL) + \frac{1+C}{l+zL} \right) q(l) q(L - zL - l) \qquad (4.8)$$

where $L = n/k$ and C = 0.3 is the parameter which controls the steepness of the standard Lund fragmentation function. The path traveled by the string between the DIS and interaction points is $\Delta x = x' - x$. The string–nucleon cross section is

$$s^{str}(\Delta x) = q(t_c - \Delta x)s_q + q(t_h - \Delta x)q(\Delta x - t_c)s_s + q(\Delta x - t_h)s_h \qquad (4.9)$$

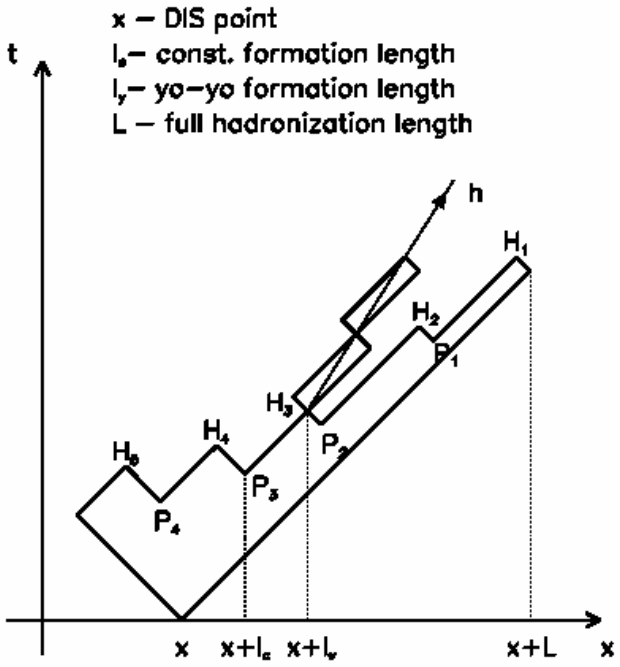

Figure 4.23: Space-time structure of hadronization in the string model. The two constituents of the hadron are produced at different points. The constituents of the hadron h are created at the points P2 and P3. They meet at H3 to form the hadron

where s_q, s_s, and s_h are the cross sections for the interaction with the nucleon of the initial string, the open string (which means the string containing the first constituent (anti)quark of the final hadron on its slow end) and the final hadron respectively (see Fig. 4.24).

It is worthy to add that (4.4) is written for the case where the nuclear properties of deuterium are neglected. In our calculations we also take into account absorption in deuterium, and use the ratio $R_M^h = R_A / R_D$ with R_A as defined in (4.4).

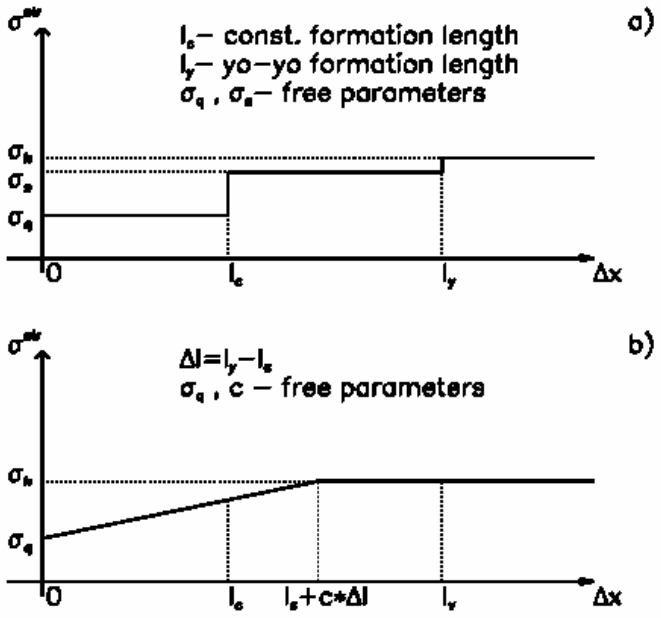

Figure 4.24: a) The behavior of the string–nucleon cross section as a function of the distance in the TSM. B) The same as in a for ITSM taking into account a more realistic smoothly increasing string–nucleon cross section

4.5.3 Inclusion of the Q^2 dependence in the TSM

In the following discussion two quantities will be used for the virtuality of the string: Q^2 (precise value) for consideration of the Q^2 dependence, and $\hat{Q}^2$ (average value) for consideration of the n and z dependences. The TSM was introduced in [5] for the description of the n and z dependences of NA and does not contain a direct Q^2 dependence, while it deals with cross sections measured at average values of Q^2:

$$s_q = s_q(\hat{Q}^2); \qquad s_s = s_s(\hat{Q}^2_{t_c}) \tag{4.10}$$

where $\hat{Q}^2$ is average value of Q^2 in the moment of DIS. $\hat{Q}^2_{t_c} = \hat{Q}^2(t_c)$ is the value of $\hat{Q}^2$ for the open string, or in the time interval t_c after DIS. $\hat{Q}^2_{t_c}$ must be smaller than $\hat{Q}^2$, because the string radiates gluons and diminishes its virtuality. QCD predicts the Q^2 dependence of the string–nucleon cross section in the form [57, 58]

$$s_q(Q^2) \sim 1/Q^2; \qquad s_s(Q^2_{t_c}) \sim 1/Q^2_{t_c} \tag{4.11}$$

Using this prediction we can express the cross section for the initial string as follows:

$$s_q(Q^2) = (\hat{Q}^2 / Q^2) s_q(\hat{Q}^2) \qquad (4.12)$$

In the same way the expression for the open string cross section can be written as

$$s_s(\hat{Q}^2_{t_c}) = (\hat{Q}^2_{t_c} / Q^2_{t_c}) s_s(\hat{Q}^2_{t_c}) \qquad (4.13)$$

where $Q^2_{t_c} = Q^2(t_c)$ is the virtuality of the string in the time interval t_c after DIS. In order to estimate the ratio of $\hat{Q}^2_{t_c} / Q^2_{t_c}$ one has to adopt the scheme given in [59, 60]. In accordance with this scheme, during time t the quark decreases its virtuality from the initial Q^2 to the value $Q^2(t)$ as follows:

$$Q^2(t) = n(t) \frac{Q^2}{n(t) + tQ^2} \qquad (4.14)$$

where $n(t) = n - k\,t$. The calculations show that for the HERMES kinematics ($1.2 < Q^2 < 9.5$ GeV2 and $\hat{Q}^2$ =2.5 GeV2), the values for the ratio $\hat{Q}^2_{t_c} / Q^2_{t_c}$ are close to 1 (for t_c in the form of (3), it changes in the region 0.97–1.04, and in the form of (4) in the region 0.92–1.12). This ratio is not dependent on n, while it depends on z and Q^2, and only at z larger than 0.7 for t_c in the form of (4.7), it deviates from 1 by more than 10%.

However, in the case of a Q^2 dependence, just the average value of z in a given Q^2 bin should be taken into account. Since the multiplicity as a function of z diminishes at large z values, the average value of z cannot be greater than 0.5 depending on the kinematics of the experiment. Calculations show that the inclusion of a factor $\hat{Q}^2_{t_c} / Q^2_{t_c}$ instead of unity leads to a maximal deviation in the R^h_M value for the lowest and highest Q^2, which in the case of HERMES kinematics corresponds to 2% at $Q^2 = 1\ GeV^2$ and 2.5% at $Q^2 = 10\ GeV^2$. Taking into account the above-mentioned arguments we can conclude that the constant approximation for s_s is quite reasonable in the HERMES kinematics.

4.5.4 Improved version of the two-scale model

In the TSM the string–nucleon cross section is a function which jumps in the points $\Delta x = t_c$ and t_h. In reality the cross section increases smoothly until it reaches the size of the hadronic cross section, hence it makes direct sense to improve the model in order to reject this (see Fig. 4.24).

We introduce the parameter c ($0 < c < 1$) in order to take into account the well-known fact that the string starts to interact with the hadronic cross section soon after the creation of the first constituent quark of the final hadron and before the creation of a second constituent. The string–nucleon cross section starts to increase from the DIS point, and reaches the value of the hadron–nucleon cross section at $\Delta x = t$. However, in that case one cannot extract the exact form of s^{str} from perturbative QCD, at least in the region of $\Delta x \sim t$. This means that some model for the shrinkage–expansion mechanism has to be introduced. We use four versions for the definition of s^{str}. Two of them were taken from [61].

Let us briefly discuss the physical reason behind the linear or quadratic dependence of the cross section on $\Delta x / t$, which will be presented below [62]. The QCD lattice calculations show that the confinement radius is much smaller than the mean hadronic radii. Consequently the color field in the hadrons is located in tubes with a transverse size much smaller than the longitudinal one. The valence quarks and di-quarks are placed at the end-points of these tubes. In case of inelastic scattering, the interacting hadron-tubes intersect in the impact-parameter plane. The probability of the crossing of the tubes is proportional to their length. This means that s^{str} increases proportional to $\Delta x / t$. In the naïve parton model, the inelastic cross section of a hadron with a nucleon is proportional to the transverse area which is filled in by its partons, i.e. s^{str} increases proportionally to $(\Delta x / t)^2$.

The first version of the definition of s^{str} is based on quantum diffusion:

$$s^{str}(\Delta x) = q(t - \Delta x)[s_q + (s_h - s_q)\Delta x / t] + q(\Delta x - t)s_h \qquad (4.15)$$

where $t = t_c + c\Delta t$, $\Delta t = t_h - t_c$.

The second version follows from the naive parton case:

$$s^{str}(\Delta x) = q(t - \Delta x)[s_q + (s_h - s_q)(\Delta x / t)^2] + q(\Delta x - t)s_h \qquad (4.16)$$

Two other expressions for s^{str} were also used [10, 54]:

$$s^{str}(\Delta x) = s_h - (s_h - s_q)\exp\left(-\frac{\Delta x}{t}\right) \qquad (4.17)$$

and

$$s^{str}(\Delta x) = s_h - (s_h - s_q)\exp\left(-\left(-\frac{\Delta x}{t}\right)^2\right) \qquad (4.18)$$

One can easily note that at $\Delta x / t \ll 1$ the expressions (4.18) and (4.17) turn into (4.16) and (4.15), respectively. At first glance it may seem that the ITSM, as opposed to the TSM, is actually a one-scale model. But one must note that t is a function of the two scales $t = (1-c)t_c + ct_h$ whereas the parameter *c* regulates the inclusion of each scale into t .

4.5.5 Results

In previous sections one of possible improvements of the TSM has been formulated and a fit has been performed to the HERMES data using the TSM and ITSM. Only the NA data for the n and z dependences for $p+$ and $p-$ mesons on Nitrogen and Krypton nuclei were used for the actual fit. For each measured bin the values of $\hat{z}$ (averaged over the given n bin) in the case of the n dependence, and $\hat{n}$ in the case of a z dependence were taken from the experimental data, whereas the use of these values allows one to avoid the problem of additional integration over z and n in (4.4). The string tension (string constant) was fixed at a static value determined by the Regge trajectory slope [60, 63]

$$k = 1/(2\pi\alpha'_R) = 1 GeV/fm \qquad (4.19)$$

The nuclear density functions (NDF) were used as follows: for deuterium the hard core deuteron wave functions from [63] were used. For Helium and Nitrogen, the shell model [64] is used, according to which four nucleons (two protons and two neutrons) fill the s-shell, and the other *A-4* nucleons are on the p-shell:

$$r(r) = r_0\left(\frac{4}{?} + \frac{2}{3}\frac{(A-4)}{A}\frac{r^2}{r_A^2}\right)\exp\left(-\frac{r^2}{r_A^2}\right) \qquad (4.20)$$

where r_A = 1.31 fm for 4He and r_A = 1.67 fm for Nitrogen. For Neon, Krypton, and Xenon the Woods–Saxon distribution was used:

$$r(r) = r_0 /(1+\exp((r-r_A)/a)) \qquad (4.21)$$

These three sets of NDF's were used for the fitting with the following corresponding parameters: the first set [9],

$$r_A = (0.978 + 0.0206A^{1/3})A^{1/3} fm \qquad (4.22)$$

The second set [65], a = 0.54 fm,

$$r_A = \left(1.19A^{1/3} - \frac{1.61}{A^{1/3}}\right) fm \qquad (4.23)$$

and the third set [66], a = 0.545 fm,

$$r_A = 1.14A^{1/3} fm \qquad (4.24)$$

where the values of r_0 are determined from the normalization condition:

$$\int d^3 r r(r) = 1 \qquad (4.25)$$

The parameter a is practically the same for all three sets; the radius r_A for the third set is larger by approximately 6% than the one for the first and second sets. Two expressions for t_c were used for the fitting procedure: (4.5) and (4.6). For $s^{str}(\Delta x)$ one expression in TSM, (4.8), and four different expressions in ITSM, (4.15)–(4.18), were used. The values of s_h (hadron–nucleon inelastic cross section) used in the fit were set equal to $s_{p^+} = s_{p^-}$ = 20mb. Two parameters were determined from the fit. In the case of TSM they are s_q and s_s, and s_q and c in the case of ITSM. The meaning of the parameter c was introduced in Section 4.5.4. Afterwards, using the best fit parameters, different predictions were made for the n, z, and Q^2 dependences for the identified hadrons on Xenon as well.

NDF	s_q(mb)	s_s(mb)	c^2/DOF	s_q(mb)	s_s(mb)	c^2/DOF
(19)	5.3± 0.01	17.1± 0.08	4.3	4.2 ±0.01	16.6± 0.07	2.3
(20)	5.5± 0.01	17.7± 0.08	4.5	4.3± 0.01	17.3± 0.07	2.4
(21)	5.8± 0.01	18.3± 0.08	4.8	4.4± 0.01	18.1± 0.07	2.6

Table 4.5. The TSM: the best values for the fitted parameters and c^2/DOF ($N_{\exp}$ = 58, N_{par} = 2)

s^{str} (12)				s^{str} (13)		
NDF	s_q (mb)	c	c^2/DOF	s_q (mb)	C	c^2/DOF
(19)	0.46±0.02	0.32± 0.03	1.4	3.5±0.01	0.23±0.002	1.9
(20)	0.62±0.01	0.31± 0.01	1.7	3.7±0.01	0.22±0.02	2.1
(21)	0.78±0.02	0.30±0.03	1.8	3.9±0.01	0.21±0.003	2.3

s^{str} (14)				s^{str} (15)		
NDF	s_q (mb)	c	c^2/DOF	s_q (mb)	C	c^2/DOF
(19)	1.1 ± 0.01	0.15 ± 0.03	2.1	3.7 ± 0.01	0.15 ± 0.02	2.3
(20)	1.3 ± 0.02	0.15 ± 0.03	2.4	3.9 ± 0.01	0.14 ± 0.02	2.6
(21)	1.5 ± 0.02	0.14 ± 0.03	2.8	4.1 ± 0.01	0.14 ± 0.02	2.9

Table 4.6. The ITSM: t_c (3). The best values for the fitted parameters and c^2/DOF ($N_{\exp}$ = 58, N_{par} = 2)

s^{str} (12)				s^{str} (13)		
NDF	s_q (mb)	c	c^2/DOF	s_q (mb)	C	c^2/DOF
(19)	0.0 ± 0.001	0.56 ± 0.02	4.6	0.97 ± 0.01	0.17 ±0.002	1.6
(20)	0.0 ± 0.002	0.53 ± 0.02	4.3	1.0 ± 0.02	0.17 ± 0.02	1.5
(21)	0.0 ± 0.002	0.49±0.006	4.0	1.1 ± 0.02	0.16 ± 0.02	1.6

s^{str} (14)				s^{str} (15)		
NDF	s_q (mb)	c	c^2/DOF	s_q (mb)	C	c^2/DOF
(19)	0.0 ± 0.001	0.24 ± 0.02	3.0	1.5 ± 0.02	0.103±0.02	1.5
(20)	0.0 ± 0.002	0.21 ± 0.02	2.9	1.7 ± 0.02	0.096±0.02	1.6
(21)	0.0 ± 0.002	0.18 ± 0.02	2.8	1.8 ± 0.02	0.089±0.02	1.8

Table 4.7. The ITSM: t_c (4). The best values for the .tted parameters and c^2/DOF ($N_{\exp}$ = 58, N_{par} = 2)

The results of the performed fit are presented in Tables 4.5, 4.6, and 4.7. Table 4.2 shows the best values of the fitted parameters, their errors and c^2/DOF for the TSM. Tables 4.6 and 4.7 show these values for the ITSM. The only difference between Tables 4.6 and 4.7 is the form of t_c that was used.

Results for the TSM (Table 4.5) are qualitatively close to the results of [5]. The values of $s_q \ll s_h$ and s_s are approximately equal to s_h, while s_q obtained in the present analysis is larger than the same in [5], because $\hat{Q}^2$ for the HERMES kinematics is smaller than at the EMC

experiment. The lowest (best fit) value of c^2/DOF = 1.4 was obtained for the ITSM (see Table 4.6) for NDF by (19), $s^{str}(\Delta x)$ as in (12) and the constituent formation time t_c in the form of (3). Values close to c^2/DOF = 1.5, were obtained for the two other versions of the ITSM with the constituent formation time t_c in the form of (4.7) (see Table 4.7) for NDF, (4.23), $s^{str}(\Delta x)$, (4.16), and NDF, (4.22), $s^{str}(\Delta x)$, (4.18).

For the TSM (Table 4.5) the best fit value of c^2/DOF =2.3 was obtained for NDF as in (4.22), and the constituent formation time t_c in the form of (4.7). The results for NA, calculated with the best values of the fit parameters from the ITSM and TSM, for the n and z dependences of the produced charged pions on the Nitrogen and Krypton targets are presented on Fig. 4.25. One can see that where precise experimental data are available, it is useful to perform not only a visual comparison of the models to the data but also use the correct quantitative comparison using the c^2 criterion. Indeed, even though a visual comparison hardly allows one to determine which model better describes the data, the value of c^2/DOF for the ITSM is substantially smaller. Furthermore, the NA for the hadrons produced on the Krypton target (but not included in the fit), were calculated. In Fig. 4.26 one can see the n and z dependences for these identified hadrons. The values of s_h that were used are as follows: $s_{p^0} = s_{K^-}$ = 20mb, s_{K^+} = 14mb, and $s_{\bar{p}}$ = 42mb. The curves correspond to the ITSM and TSM model calculations with the best set of parameters.

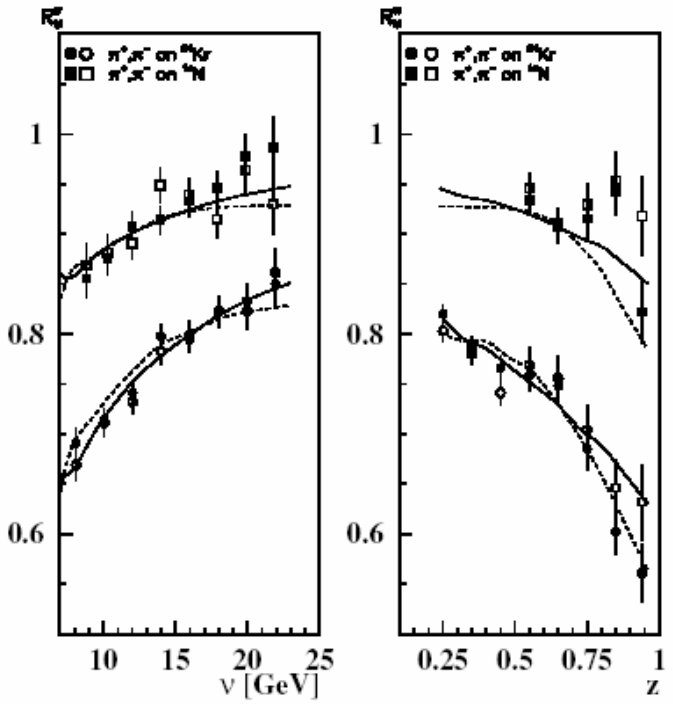

Fig. 4.25. Hadron multiplicity ratio R of charged pions for the Nitrogen [8] and Krypton [3] nuclei as a function of ν *(left panel) and z (right panel). The solid curves correspond to the ITSM with NDF, (4.20), for Nitrogen and NDF, (4.22), for Krypton and* σ^{str}*, (4.15), with* τ_c *in the form (4.6) for the values of the parameters* σ_q *= 0.46mb, c = 0.32. The dashed curves correspond to the TSM with the same NDF for nuclei and* τ_c *in the form (4.7) for the values of parameters* σ_q *= 4.2mb,* σ_s *= 16.6mb. These data were included in the fit and the curves were obtained as the fit result.*

Satisfactory agreement is achieved for all of the considered hadrons. The proton was not included in these calculations due to the following reasons. Among others, the proton is quite unique, because it already exists in the nucleus before the DIS act. All other hadrons are mainly produced as a result of fragmentation of the knocked-out quark and only the proton has more complicated production mechanisms: from the remnant of the nucleon on which the DIS takes place, from the fragmentation of the knocked out quark. Also, another possible scenario could be the color interaction of the other nucleons with the string. Figure 4.27 shows the results of the TSM and ITSM in comparison with the experimental data for the NA of charged hadrons on the Cuprum target [5] performed in the region of ν and Q^2 values higher than in the HERMES kinematics. In order to compare with the EMC data one had to have redefined σ_q to the $\hat{Q}^2_{EMC}$ ~ 10.6 GeV2 according to the expression (4.12). The Fig. 4.27 is worth to be discussed in detail for several reasons. First, the EMC data for the NA are for charged hadrons and it is not quite clear which

value should be used for s_h. We use the same s_h as for the pions, due to the simple assumption that at higher energies mainly the pions are produced; moreover, it has been checked that the NA weakly depends on s_h at higher energies. Secondly, one can see that the high energy data can be used to distinguish, or choose more precisely, different versions of the models. In particular, the EMC data seem to agree better with the case where the constituent formation time t_c is used as in (4.7).

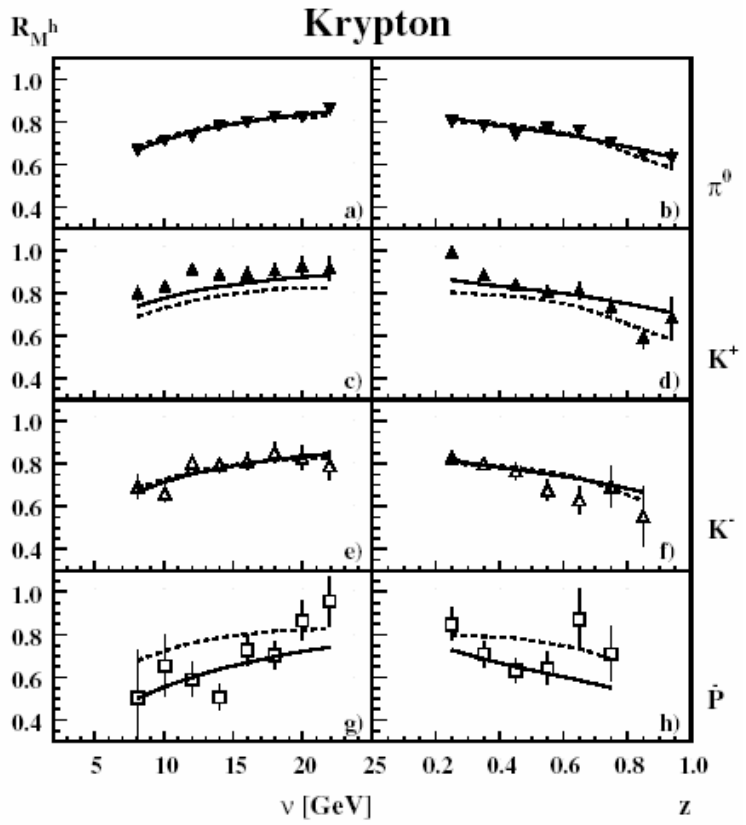

Figure 4.26. Hadron multiplicity ratio R of different species of hadrons produced on the Krypton target [3] as a function of n *(left panel) and z (right panel). These data were not included in the fit. The curves are calculated with the best fit parameters described in the caption of Fig. 4.22*

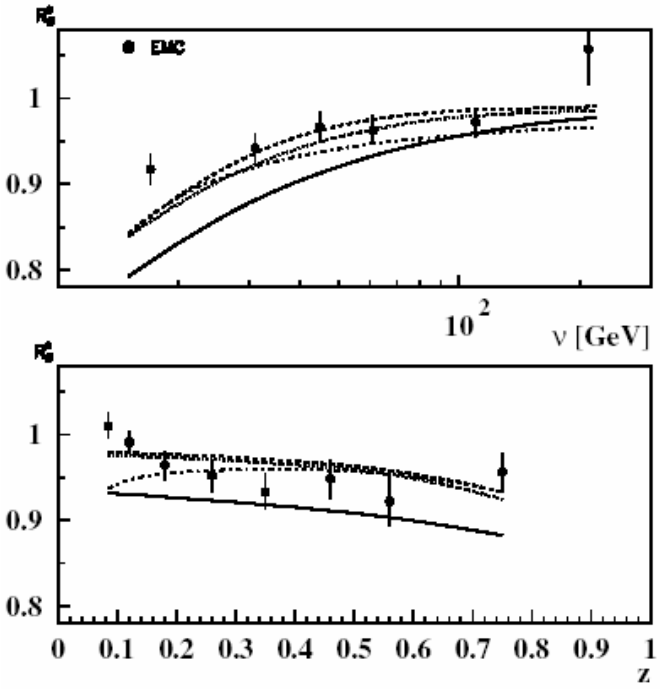

Fig. 4.27. The ratio R for charged hadrons for Cuprum [5] as a function of ν *(upper panel) and z (lower panel). The solid, dashed, and dotted curves correspond to three sets of parameters with the minimal values of* χ^2*/DOF in case of ITSM (see Tables 4.6 and 4.7): solid NDF, (4.22),* σ^{str}*, (4.15),* τ_c *(4.6),* σ_q *= 0.46mb, c = 0.32,* χ^2*/DOF = 1.4; dashed NDF, (4.23),* σ^{str}*, (13),* τ_c*, (4.7),* σ_q *= 1.0mb, c = 0.17,* χ^2*/DOF = 1.5; dotted NDF, (4.22),* σ^{str}*, (4.18),* τ_c*, (4.7),* σ_q *= 1.5mb, c = 0.103,* χ^2*/DOF = 1.5. The dashed-dotted curves correspond to the best set of parameters in case of TSM (see Table 4.5): NDF, (4.22),* τ_c*, (4.7),* σ_q *= 4.2mb,* σ_s *= 16.6mb,* χ^2*/DOF = 2.3*

The investigation of NA is incomplete until one includes also the Q^2 dependence into the consideration. This was already discussed in Section 4.5.3. On the figures that show the results for the Q^2 dependence it is convenient to represent the NA ratio versus the inverse of Q^2, because of the connection of this dependence with higher twist effects. Indeed, from (4.12), (4.9), (4.15)–(4.18), and (4.4) one can conclude that in first approximation the expansion over the degrees of $1/Q^2$ for the NA ratio can be represented in the form $R_A = a + b/Q^2$, where b is negative. One has to note that for the calculation of the Q^2 dependence, $\sigma_q(Q^2)$ was used instead of σ_q, whereas the corresponding expression is given by (9).

Finally, let us briefly discuss the nuclear matter distribution functions. For medium and heavy nuclei the preferable NDF is the Woods–Saxon distribution. However, there is some freedom

in the choice of the parameters themselves, therefore we have included three sets of parameters, (4.22)–(4.23), in order to study the uncertainty of the fitting procedure related to the NDFs.

As one can observe, the two-parameter fit demonstrates satisfactory agreement with the HERMES data. A minimum c^2 (best fit) was obtained for the ITSM, including the expression (4.15) for s^{str} and (4.6) for t_c. The accumulated data do not give the possibility to make a firm choice between the expressions (4.15)–(4.18) for the s^{str}, as well as to make a distinct preference of the definitions (4.6) or (4.7) for t_c, because they give close values of c^2.

Preferable NDF's are the sets (4.22) and (4.23) as described in Sect. 4.5.4, because with these NDF's, the lowest values of c^2 were obtained for both TSM and ITSM. Moreover, considering ten versions of different forms for t_c and s^{str} in TSM and ITSM, only two of them with the relative minimal c^2 values correspond to NDF (21) (see Tables 4.5, 4.6, and 4.7).

4.5.6 Application of TSM and ITSM to the double-hadron data

An attempt at application of the models described in the previous sub-sections to the double hadron data (See section 4.4) has been made [67]. Moreover, a prediction for the n -dependence of the two-hadron system attenuation has been calculated, and presented in this sub-section.

In articles [10,11,12] the process of leptoproduction of two-hadron system on a nucleus with atomic mass number *A* was theoretically considered for the first time:

$$l_i + A \to l_f + h_1 + h_2 + X \qquad (4.26)$$

where the hadrons h_1 and h_2 carry fractions z_1 and z_2 of the total available energy. The NA ratio for that process can be expressed in form:

$$R_M^{2h} = 2ds_A(n, Q^2, z_1, z_2) / Ads_D(n, Q^2, z_1, z_2) \qquad (4.27)$$

where s_A and s_D are the cross-sections for the reaction (4.26) on nuclear and deuterium targets, respectively, n and Q^2 denote the energy of the virtual photon and square of its four-momentum. One can picture the reaction (4.26) as shown in Fig. 4.28. The interaction of the lepton with nucleon occurs at the point (b,x), where the intermediate state *q* begins to propagate (*b* and *x* are impact

parameter and longitudinal coordinate of DIS point). At some points the string breaks, and as a result the first constituents of hadrons h_1 and h_2 are produced at the points (b, x_1) and (b, x_2).

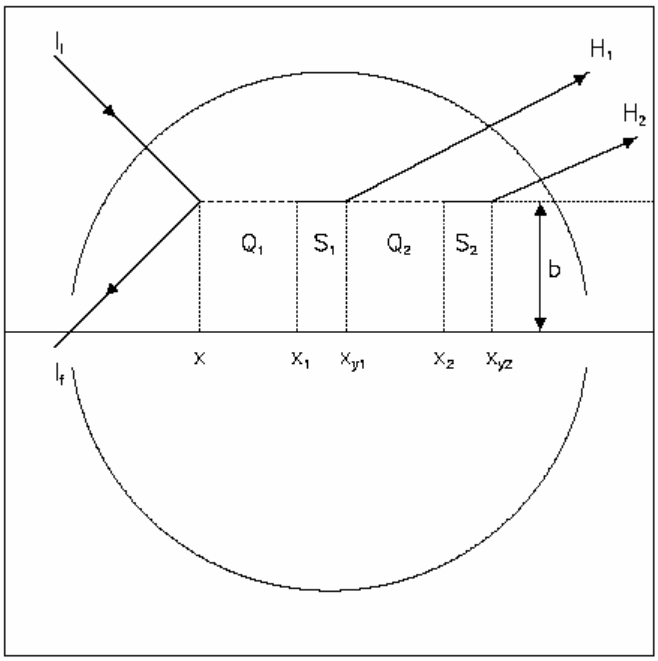

Figure 4.28: Leptoproduction of two-hadron system on nuclear target. Details see in text.

Also, at the points (b, x_{xy1}) and (b, x_{xy2}) the yo-yo of the hadrons h_1 and h_2 is formed ("yo-yo" system means, that the colorless system with valence content and quantum numbers of the final hadron is formed, but without its "sea" partons). In the string model there are simple connections between the points $x_{xy1} - x_1 = z_1 L$ and $x_{xy2} - x_2 = z_2 L$, where L is the full hadronization length, $L = n / k$, k is the string tension (string constant). The NA ratio can be presented in the following form:

$$R_M^{2h} \approx \frac{1}{2} \int d^2 b \int_{-\infty}^{\infty} dx \int_x^{\infty} dx_1 \int_{x_1}^{\infty} dx_2 \, r(b, x) \times \qquad (4.28)$$

$$\times \left[D(z_1, z_2, x_1 - x, x_2 - x) W_0(h_1, h_2; b, x, x_1, x_2) + D(z_2, z_1, x_1 - x, x_2 - x) W_0(h_2, h_1; b, x, x_1, x_2) \right]$$

where $D(z_1, z_2, l_1, l_2)$ (with $l_1 < l_2$) is the distribution of the formation lengths l_1 and l_2 of the hadrons and $r(b, x)$ is the nuclear density function normalized to unity. W_0 is the probability that neither the hadrons h_1, h_2 nor the intermediate state leading to their production (initial and open strings) interact inelastically in the nuclear matter:

$$W_0(h_1,h_2;b,x,x_1,x_2)=(1-Q_1-S_1-(H_1+Q_2+S_2+H_2-H_1(Q_2+S_2+H_2)))^{(A-1)} \quad (4.29)$$

where Q_1 and Q_2 are the probabilities for the initial string to be absorbed in the nucleus within the intervals (x,x_1) and (x_{y1},x_2), respectively. S_i (i=1, 2) is the probability for the open string containing the first constituent parton for h_i to be absorbed in the nucleus within an interval (x_i,x_{yi}), and H_i (i=1, 2) is the probability for the hi to interact inelastically in the nuclear matter, starting from the point x_{yi}. The probabilities Q_1,Q_2,S_1,S_2,H_1,H_2 can be calculated using the general formulae:

$$P(x_{\min},x_{\max})=\int_{x_{\min}}^{x_{\max}} s_P r(b,x)dx \quad (4.30)$$

where the subscript P denotes the particle (initial string, open string or hadron), s_P its inelastic cross section on nucleon target, and $x_{\max}$ and $x_{\min}$ are the end points of its path in the x direction, as it is shown in Fig. 4.28.

Results for the double ratio R_M^{2h} as a function of z_2 are presented on Fig. 4.29. On panels a), c), e) three options of the theoretical curves are shown: solid curves correspond to the TSM with CFT1; dashed curves correspond to the ITSM with CFT2; dotted curves correspond to the ITSM with CFT1. According to the ideology of the string model, the transverse size of the string is much less than longitudinal one. It means that the hadrons produced from the string have close impact parameters, and could partly screen one another, which in turn must lead to the weakness of NA (partial attenuation). To study this effect and to compare with the basic supposition, that two hadrons attenuate independently (full attenuation), we consider partial attenuation in it's extreme case, when two hadrons fully screen one another, and as a result the two-hadron system attenuates as a single hadron. The results of calculations within this conditions are shown in panels b), d), f).

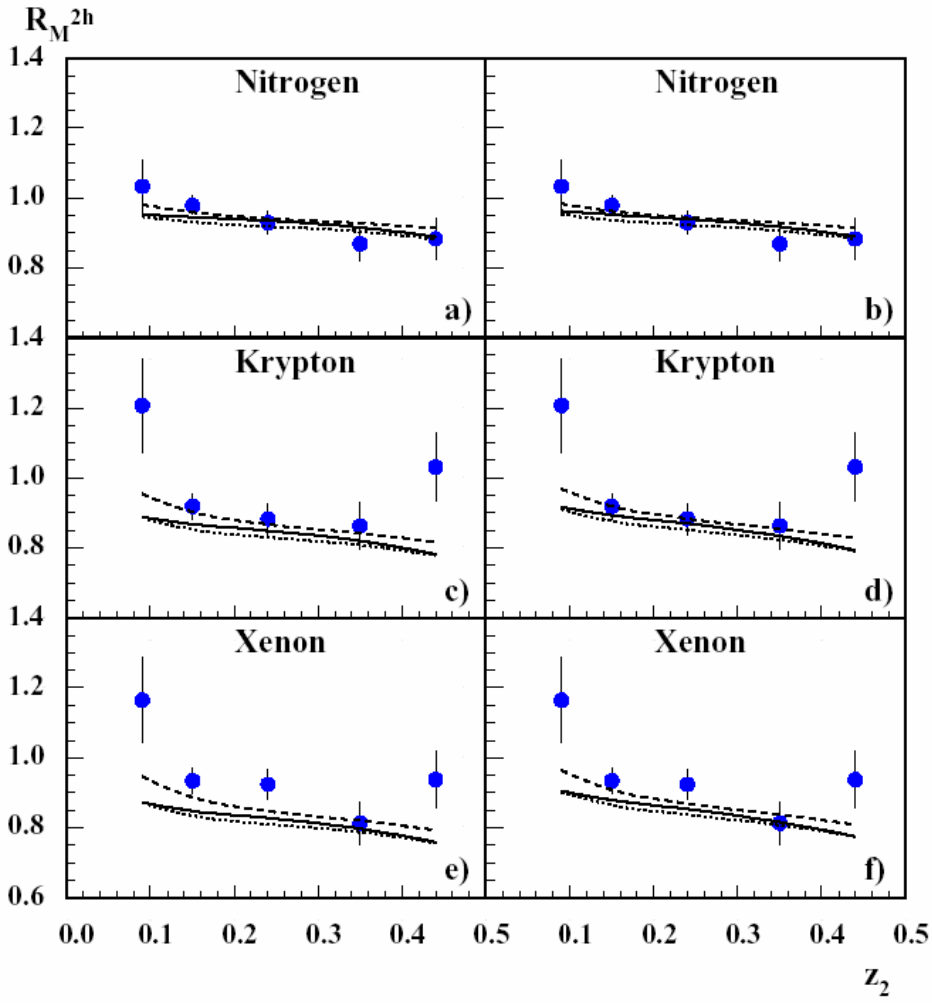

Figure 4.29: Double ratio R_M^{2h} as a function of z_2. The explanations for the points and curves are given in the text.

Fig. 4.30 shows the model prediction for n -dependence of double ratio R_M^{2h} for Nitrogen, Krypton and Xenon targets. On panels a), c), e) three varieties of the theoretical curves are shown: solid curves correspond to the TSM with CFT1; dashed curves correspond to the ITSM with CFT2; dotted curves correspond to the ITSM with CFT1. On panels b), d), f) the same curves are shown, but calculated with an additional condition that only the first produced hadron attenuates (partial attenuation). Easy to see, that curves corresponding to the full and partial attenuation have different behavior at low values of n . In Fig. 4.31 Krypton only data is shown, as an example. Curves are marked in the same way as in Fig. 4.30.

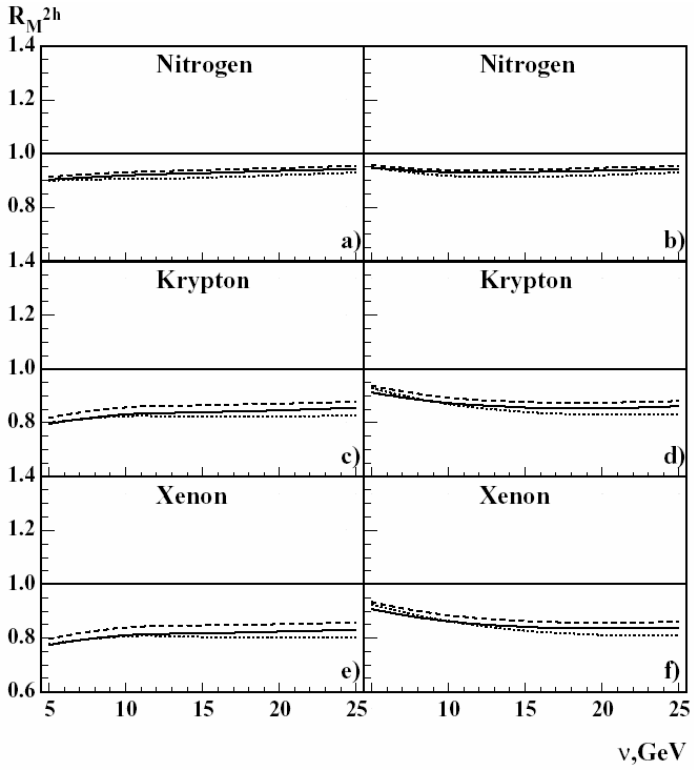

Figure 4.30: Double ratio R_M^{2h} as a function of n . *The explanations for the curves are given in text.*

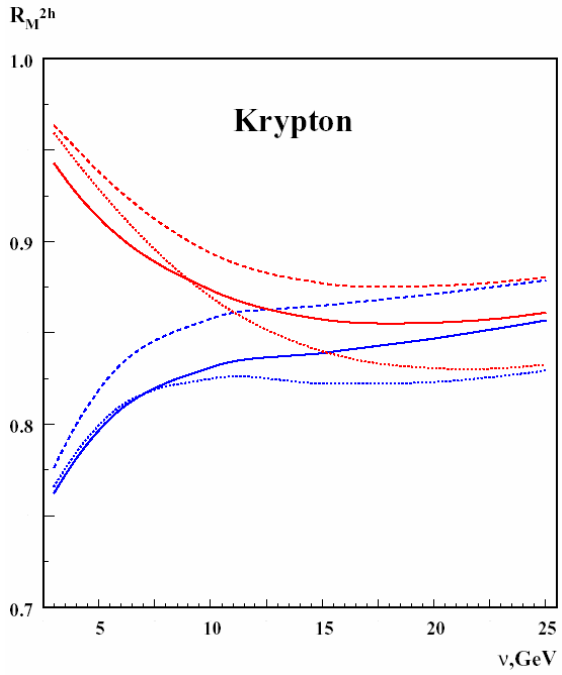

FIG. 4.31: Double ratio R_M^{2h} as a function of n . *The explanations for the curves are given in the text. Lower curves correspond to the case that two hadrons attenuates independently (full attenuation) and upper curves correspond to the case that only first produced hadron attenuates (partial attenuation)*

Lower curves correspond to the case of full attenuation and upper curves correspond to the case that only first produced hadron attenuates (partial attenuation). The measurement of NA ratio in the region of n from 3 to 10 GeV allows to verify a prediction about possible mutual screening of hadrons in string. Such an experiment can be useful for comparison with the results obtained at RHIC by STAR Collaboration [68], which show that two hadrons from one jet absorbed more weakly than two hadrons from away-side jets.

Conclusions

The thesis is dedicated to one of the main direction of modern high energy physics – the studies of quark hadronization. An extensive and substantially statistically supported data has been obtained for lepton scattering on a variety of nuclear targets, and measurements of the nuclear multiplicity ratios have been performed. Moreover, for the part of the data that provide exceptionally high statistics, not only conventional measurements of one-dimensional dependencies have been made, but also two-dimensional analysis in phase-space for the virtual photon energy and part of the energy carried by the hadron in final state. These data are very important in understanding the details of the hadronization process and correlations between its dependence on various kinematic variables.

Furthermore, results have been obtained for the dependence of the nuclear attenuation on atomic mass number. Various detailed fits have been performed using the best statistically supported data set to obtain the said dependence in exponential form according to the parameterization (4.1). As another novelty of these studies, interesting results for the dependence of those exponential parameters on the formation length have also been shown in this thesis. Another important result is the measurement of the double-hadron to one-hadron multiplicity ratios, which may provide a fine-tuning tool for distinguishing different mechanisms of the hadron energy loss. Like the jet correlation measurements in heavy-ion collisions, the double-hadron observables in semi-inclusive deep inelastic scattering can provide new information for differentiating between models of hadronization in nuclei that are indistinguishable in single-hadron measurements.

An attempt at interpretation of some of the results has been made. An Improved Two-Scale model has been formulated and developed in this work, and a very satisfactory describe the data on a quantitative level, be it for the conventional multiplicity ratio, or for the double-hadron attenuation.

The results presented in this thesis have been reported at numerous seminars at DESY and YerPhI, as well as at several international conferences, and are well recognized by the nuclear

physics community world-wide. These studies will undoubtedly help in further development of the theory, understanding of the quark-gluon interaction processes and planning new experiments.

Acknowledgments

This work would not have been possible without my colleagues from the nuclear group at HERMES, Norik Akopov, Garry Elbakian, Pasquale DiNezza, Henk Blok. Levon Grigorian for his patience in explaining me the theoretical background of the studies presented in this work. I would also like to thank many HERMES colleagues for helpful discussions and suggestions, Elke Aschenauer, Delia Hasch and many others. And naturally, to my supervisor Robert Avakian for all the effort in making this happen.

Ամփոփագիր

Ատենախոսությունը նվիրված է ժամանակակից բարձր էներգիաների ֆիզիկայի հիմնախնդիրներից մեկին, այն է՝ քվարկի հադրոնիզացումը խնդրին: Առաջին անգամ հաջողվել է ստանալ տարբեր միջուկների վրա լեպտոնների ցրման վերաբերյալ մեծ ստատիստիկայով փորձարարական տվյալներ և անցկացնել ոչ միայն ավանդական՝ տարբեր կինեմատիկական փոփոխականներով հադրոնների կլանման ֆունկցիայի միաչափ վերլուծություն, այլև ֆազային տարածության մեջ երկչափ վերլուծություն՝ ըստ վիրտուալ ֆոտոնի էներգիայի n և էներգիայի մասնաբաժնի z, որը իր հետ տանում է հադրոնը:

Բացի դրանից, ատենախոսության մեջ առաջին անգամ ստացվել են կարևոր արդյունքներ աստիճանային ցուցչի վարքի վերաբերյալ, որը մտնում է հադրոնների կլանման ֆունկցիայի կախվածության պարամետրիզացման մեջ՝ կախված միջուկային թիրախի ատոմական համարից, L_C մեծությունից, որը բնորոշում է հադրոնի ձևավորման միջին երկարությունը:

Ստացված տվյալների նկարագրման համար մշակված է և իրականացված լարի երկչափանի վերափոխված մոդելը, որը հնարավորություն է տալիս բավականաչափ լավ նկարագրել փորձարարական տվյալները, ինչպես սովորական կլանման ֆունկցիայի համար, այնպես էլ վերջնական վիճակում երկու հադրոնների դեպքի համար:

Ատենախոսության մեջ բերված արդյունքները բազմիցս քննարկվել են ԵրՖԻ-ի և DESY-ի սեմինարներում, զեկուցվել են միջազգային կոնֆերենցիաներում և լայնորեն հայտնի են մասնագետների շրջանում: Ստացված արդյունքները, անկասկած, կնպաստեն տեսության հետագա զարգացմանը, քվարկների և գլյուոնների փոխազդեցության դինամիկայի հասկացմանը, ինչպես նաև կօգտագործվեն ապագա գիտափորձերը նախագծելիս:

Bibliography

1. *A. Airapetian et al., (HERMES) Quark helicity distributions in the nucleon for up, down, and strange quarks from semi-inclusive deep-inelastic scattering. Phys. Rev. D71, 2005, 012003*
2. *E. Wang and X.-N. Wang, Jet tomography of dense and nuclear matter. Phys. Rev. Lett. 89, 2002, 162301*
3. ***A. Airapetian, N. Akopov, Z. Akopov et al., (HERMES), Quark Fragmentation to \pi+/-, \pi0, K+/-,p and pbar in the Nuclear Environment, Phys. Lett. B577, 2003, 37***
4. *F. Halzen and A.D. Martin. Quarks&Leptons, Jhon Wiley&sons, 1984*
5. *J. Ashman et al., (EMC) Comparison of forward hadrons produced in muon interactions on nuclear targets and deuterium. Z.Phys. C52, 1991, 1*
6. *M. Adams et al., (E665) Scaled energy (z) distributions of charged hadrons observed in deep inelastic muon scattering at 490-GeV from xenon and deuterium targets. Phys. Rev. D50, 1994, 1836*
7. *L Osborne et al., Electroproduction Of Hadrons From Nuclei. Phys. Rev. Lett. 40, 1978, 1624*
8. ***A. Airapetian, N. Akopov, Z. Akopov et al., (HERMES) Hadron Formation in Deep Inelastic Positron Scattering from 14N and 2H, Eur.Phys.J. C20, 2001,479***
9. *A. Bialas, M. Gyulassy, Lund Model And An Outside - Inside Aspect Of The Inside-Outside Cascade. Nucl. Phys. B291, 1987, 793*
10. *A. Bialas, Attenuation Of High-Energy Particles Leptoproduced In Nuclear Matter. Acta Phys. Pol. B11, 1980, 475*
11. *M. Gyulassy and M. Plumer, Jet quenching in lepton nucleus scattering. Nucl. Phys. B346, 1990, 1*

12. *J. Czyzewski and P. Sawicki, Fragmentation of colored strings in nuclear matter. Z.Phys. C56, 1992, 493*
13. *N. Akopov, G. Elbakian, L. Grigoryan, Nuclear attenuation of charged mesons in deep inelastic scattering. hep-ph/0205123, 2002*
14. ***N. Akopov, L. Grigoryan, Z. Akopov, Application of the Two-Scale Model to the HERMES Data on Nuclear Attenuation, Eur. Phys.J. C44, 2005, 219***
15. *B.G. Zakharov, Fully quantum treatment of the Landau-Pomeranchuk-Migdal effect in QED and QCD. Pis'ma Zh. Eksp. Teor. Fiz. 63, 1996, 906*
16. *X.F. Guo and X.-N. Wang, Multiple scattering, parton energy loss and modified fragmentation functions in deeply inelastic e A scattering. Phys.Rev.Lett. 85, 2000, 3591*
17. *F. Arleo, Tomography of cold and hot QCD matter: Tools and diagnosis. JHEP 11,2002,44; F. Arleo, Quenching of hadron spectra in DIS on nuclear targets. Eur.Phys.J. C30, 2003, 213*
18. *Gyulassy, I. Vitev, X.-N. Wang and B.-W. Zhang, Jet quenching and radiative energy loss in dense nuclear matter. "Quark-Gluon Plasma" vol.3, 2004, 123, Ed. By R.Hwa, X.-N. Wang*
19. *X.-N. Wang, Particle production in high-energy heavy ion collisions. hep-ph/0111404, 2001*
20. *L. Landau, I. Pomeranchuk, Electron cascade process at very high-energies. Dokl.Akad.Nauk. SSSR 92, 1953, 535*
21. *A. Accardi, V. Muccifora, H.J. Pirner, Hadron production in deep inelastic lepton nucleus scattering. Nucl.Phys. A720, 2003, 131 and nucl-th/0211011, 2002*
22. *B. Andersson et al., Parton Fragmentation And String Dynamics. Phys.Rep. 97, 1983, 31; B. Andersson The Lund Model, Cambridge University Press,1998*
23. *B.Z. Kopeliovich, J. Nemchik, E. Predazzi and A. Hayashigaki, Nuclear hadronization: Within or without? Nucl.Phys. A740, 2004, 211*
24. *T. Falter and U. Mosel, Electroproduction of hadrons on nuclei at GeV energies. Fizika, B13, 2004, 165; T. Falter, W. Cassing, K. Gallmeister and U. Mosel, Hadron formation and attenuation in deep inelastic lepton scattering off nuclei. Phys.Lett. B594, 2004, 61; T. Falter, W. Cassing, K. Gallmeister and U. Mosel, Hadron attenuation in deep inelastic lepton-nucleus scattering. Phys.Rev. C70, 2004, 054609*

25. *X.-N. Wang, Jet tomography of quark gluon plasma. Braz.J. 34, 2004, 1288*
26. *H.P. Blok and L. Lapikas, A-dependence of hadronization in nuclei. Phys.Rev.C73, 2006, 038201*
27. *The HERMES Experiment: From the Design to the First Results, M. Dueren, DESY Grey Report: DESY-HERMES 95-02*
28. *K. Ackerstaff et al., The HERMES spectrometer. Nucl. Instrum. Meth., A417, 1998, 230*
29. *C. Baumgarten et al., A gas analyzer for the internal polarized target of the HERMES experiment. Nucl. Instrum. Meth., A508, 2003, 268*
30. *T. Shin, The Nuclear Dependence of Structure Function Ratios from Unpolarized Deep Inelastic Scattering. PhD thesis, Hampton University, Massachusetts Institute of Technology, 2000*
31. *N. Akopov et al. The HERMES dual-radiator ring imaging Cherenkov detector. Nucl. Instrum. Meth. A479, 2002, 511*
32. *H. Avakian et al., Performance of F101 radiation resistant lead glass shower counters. Nucl. Instrum. Meth., A378, 1996, 155*
33. *H. Avakian et al., Performance of the electromagnetic calorimeter of the HERMES experiment. Nucl. Instrum. Meth., A417, 1998, 69*
34. *A. Airapetian et al. The Time of flight technique for the HERMES experiment. Nucl.Instrum. Meth.A, 2005, 540*
35. *A. Airapetian et al. (HERMES) The Q**2 dependence of nuclear transparency for exclusive rho0 production. Phys.Rev.Lett.90, 2003 .052501*
36. *R. Kaiser, B. Hommez, H. Jackson and Y. Miyachi, Using the RICH detector for physics analysis. HERMES Internal Note, see HERMES RICH Group web site.*
37. *R. Kaiser Unfolding of Hadron Distributions and Asymmetries. HERMES Internal Note 00-027.*
38. *A. Hillenbrand, Measurement and Simulation of the Fragmentation Process at HERMES. PhD Thesis Friedrich Alexander Universitat Erlangen Nuernberg, 2005*

39. *A. A. Akhundov, D.Y. Bardin ,N. M Shumeiko, ELECTROMAGNETIC CORRECTIONS TO THE DEEP INELASTIC mu p SCATTERING AT HIGH-ENERGIES. Sov.J.Nucl.Phys.,26, 1977 ,660*
40. *D.Y. Bardin and N.M. Shumeiko, ON THE WEAK NEUTRAL CURRENT AND ELECTROMAGNETIC CORRECTION EFFECTS ON THE QUANTITIES MEASURED IN DEEP INELASTIC lepton+- N SCATTERING. Sov.J.Nucl.Phys.,29,1979,499*
41. *A. A. Akhundov, D.Y. Bardin ,N. M Shumeiko, Electromagnetic Corrections To Elastic Radiative Tail In Deep Inelastic Lepton - Nucleon Scattering. Sov.J.Nucl.Phys,44 ,1986, 988*
42. *I. Akushevich,N. Shumeiko and A. Soroko, Radiative effects in the processes of hadron electroproduction. Eur.Phys.J.,C10, 1999 ,681*
43. ***A. Airapetian, N. Akopov, Z. Akopov et al., Semi-Inclusive Deep-Inelastic Scattering on Nuclei to be published in Nucl. Phys. B***
44. *E. Garutti, Nuclear Effects in Semi-Inclusive Deep Inelastic Scattering off 84Kr and other nuclei, PhD thesis, Universitet van Amsterdam, 2003*
45. *RhoMC generator, http://hermes.desy.de/hmc/RhoMC*
46. *P. Liebing, Can the gluon polarization in the nucleon be extracted from HERMES data on single high pT hadrons?, PhD thesis Universitat Hamburg, 2004*
47. ***Z. Akopov, Electroproduction of Pseudoscalar Mesons on Nuclei at Hermes, AIP Conference Proceedings – August 30, 2004, Volume 717, pp. 807-811***
48. *B. Kopeliovich, J. Nemchik and E. Predazzi, Hadronization in nuclear environment. Proceedings of the workshop on Future Physics at HERA, Ed. By G. Ingelman, A. De Roeck and R. Klanner, DESY, 1995/1996, vol. 2, 1038(nucl-th/9607036); B. Kopeliovich et al., Nucl.Phys., A740, 2004 ,211*
49. *J.W. Cronin et al., PRODUCTION OF HADRONS WITH LARGE TRANSVERSE MOMENTUM AT 200-GeV, 300-GeV, AND 400-GeV. Phys.Rev., D11,1975,3105*
50. *X.-N. Wang and X. Guo, Multiple parton scattering in nuclei: Parton energy loss. Nucl.Phys. A696, 200 , 788*
51. ***A. Airapetian, N.Akopov, Z. Akopov et al. (HERMES), Double-hadron leptoproduction in the nuclear medium, Phys.Rev.Lett. 96,2006,162301***

52. *K. Gallmeister and W. Cassing, Jet quenching by (pre-)hadronic final state interactions at RHIC. Nucl.Phys. A748, 2005, 241*
53. *N. Nikolaev, NUCLEAR EFFECTS IN PHOTOPRODUCTION AND LEPTOPRODUCTION: WHERE ARE THEY? ARE THEY NEGLIGIBLE? Z.Phys. C5, 1980,291; V. Anisovich et al., Yields Of Projectile Fragments In Hadron - Nucleus Interactions And Quark Structure Of Hadrons, Nucl.Phys. B133, 1978, 477; G. Davidenko and N. Nikolaev, Hadron Final States In Deep Inelastic Leptoproduction On Nuclei. Nucl.Phys. B135,1978,333*
54. *R. Badalyan, Fast hadron formation mechanism in leptoproduction in nuclei. Z.Phys., C55, 1992, 647*
55. *D.J. Dean et al., Multiparticle production in lepton nucleus collisions and relativistic string models. Phys.Rev. C46, 1992, 2066*
56. *B. Kopeliovich, ARE HIGH-ENERGY QUARKS ABSORBED IN NUCLEAR MATTER? Phys.Lett. B243, 1990, 141*
57. *B. Kopeliovich, B. Povh, Interplay of soft and hard interactions in nuclear shadowing at high q**2 and low x.***, Proceedings of the workshop on Future Physics at HERA, Ed. By G. Ingelman, A. De Roeck and R. Klanner, DESY, 1995/1996,vol.2,959*
58. *K. Golek-Biernat et al., Saturation effects in deep inelastic scattering at low Q**2 and its implications on diffraction.Phys.Rev.,D59, 1998, 014017*
59. *B. Kopeliovich et al., Hadronization of highly virtual quark in deep inelastic scattering on nuclei. "Hadron Structure '92" Proceedings Stara lesna, Czecho-Slovakia, Sept. 6-11, 1992, 164*
60. *B. Kopeliovich, J. Nemchik, Hadronization of highly virtual quarks in nuclei. preprint JINR E2-91-150, 1991; preprint of INFN-ISS, 91/3, 1991, Roma*
61. *G. Farrar et al., Transparency In Nuclear Quasiexclusive Processes With Large Momentum Transfer. Phys.Rev.Lett., 61 ,1988, 686*
62. *T. Sjostrand, L. Lonnblad, S. Mrenna, PYTHIA 6.2: Physics and manual. hep-ph/0108264, 2001;LU TP 01-21*
63. *L. Elton, "Nuclear Sizes", Oxford University Press, 1961, p.34*

64. *A. Bialas et al., Leptoproduction Of Hadrons From Nuclear Targets And Fragmentation Of Quarks Into Hadrons. Phys.Lett., B133, 1983, 241*

65. *A. Capella, A. Krzywicki, A Theoretical Model Of Soft Hadron – Nucleus Collisions At High-Energies. Phys.Rev, D18, 1978, 3357*

66. *R.V. Reid, Local phenomenological nucleon-nucleon potentials. Annals of Physics 50, 1968, 411*

67. ***N. Akopov, L. Grigoryan, Z. Akopov, Nuclear attenuation of high energy two-hadron system in the string model, hep-ph/0605128, 2006; submitted to Eur.Phys.J. C***

68. *J. Adams et al., Evidence from d + Au measurements for final state suppression of high p(T) hadrons in Au+Au collisions at RHIC. Phys.Rev.Lett., 91, 2003, 072304*

Appendix A. Detailed studies of RICH unfolding effect

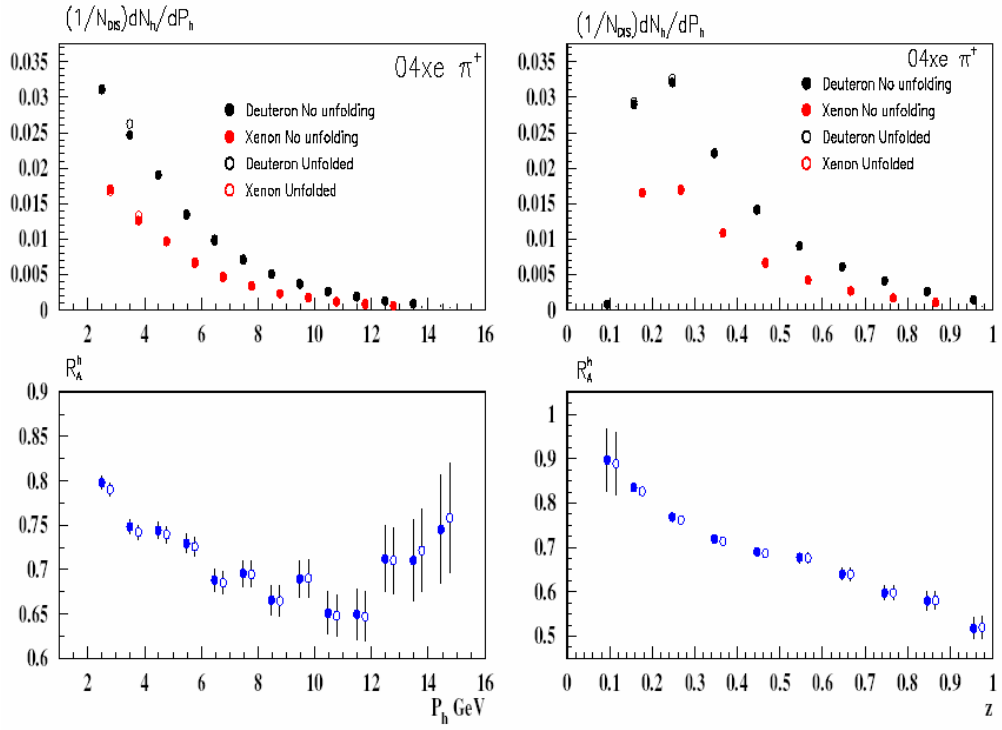

Figure A.1: Distributions of the multiplicities with and without the unfolding, versus the hadron momentum (left panel) and z (right panel) for positive pions.

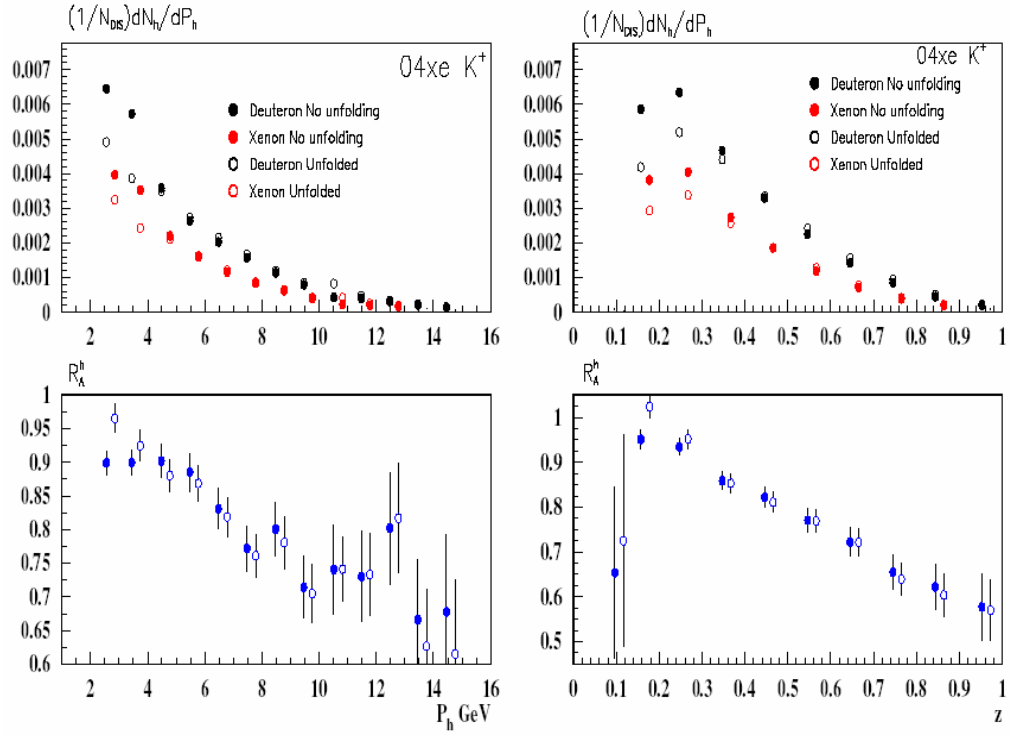

Figure A.2: Distributions of the multiplicities with and without the unfolding, versus the hadron momentum (left panel) and z (right panel) for positive kaons

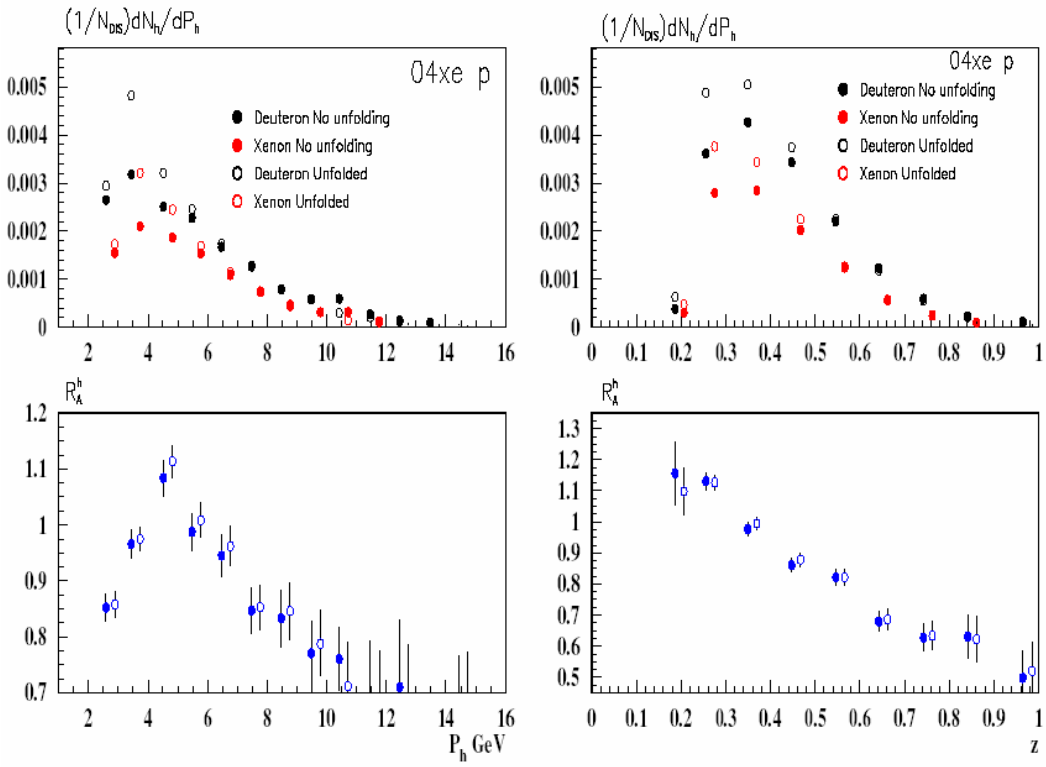

Figure A.3: Distributions of the multiplicities with and without the unfolding, versus the hadron momentum (left panel) and z (right panel) for protons

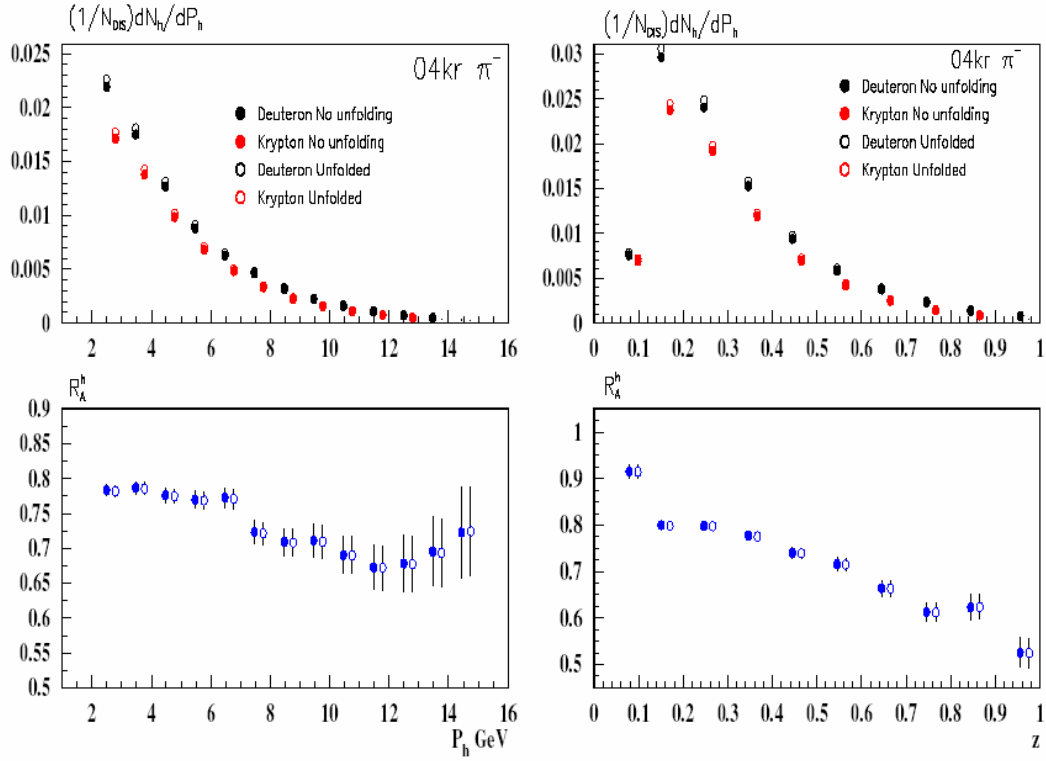

Figure A.4: Distributions of the multiplicities with and without the unfolding, versus the hadron momentum (left panel) and z (right panel) for negative pions

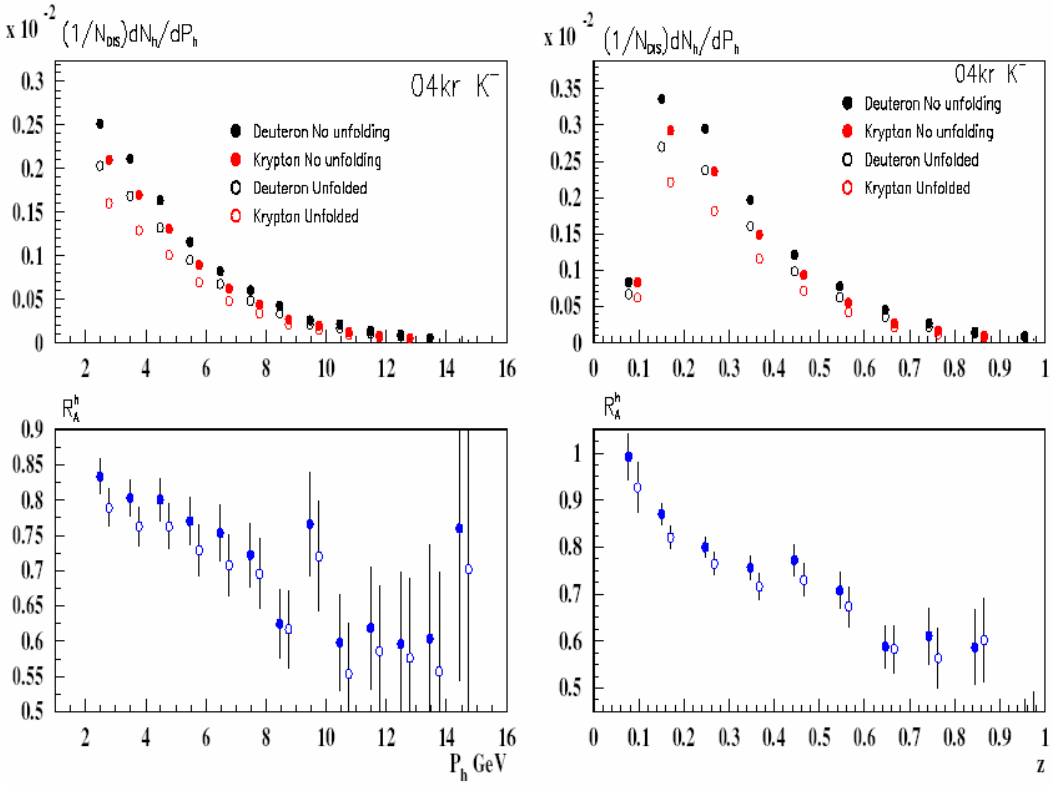

Figure A.5: Distributions of the multiplicities with and without the unfolding, versus the hadron momentum (left panel) and z (right panel) for negative kaons

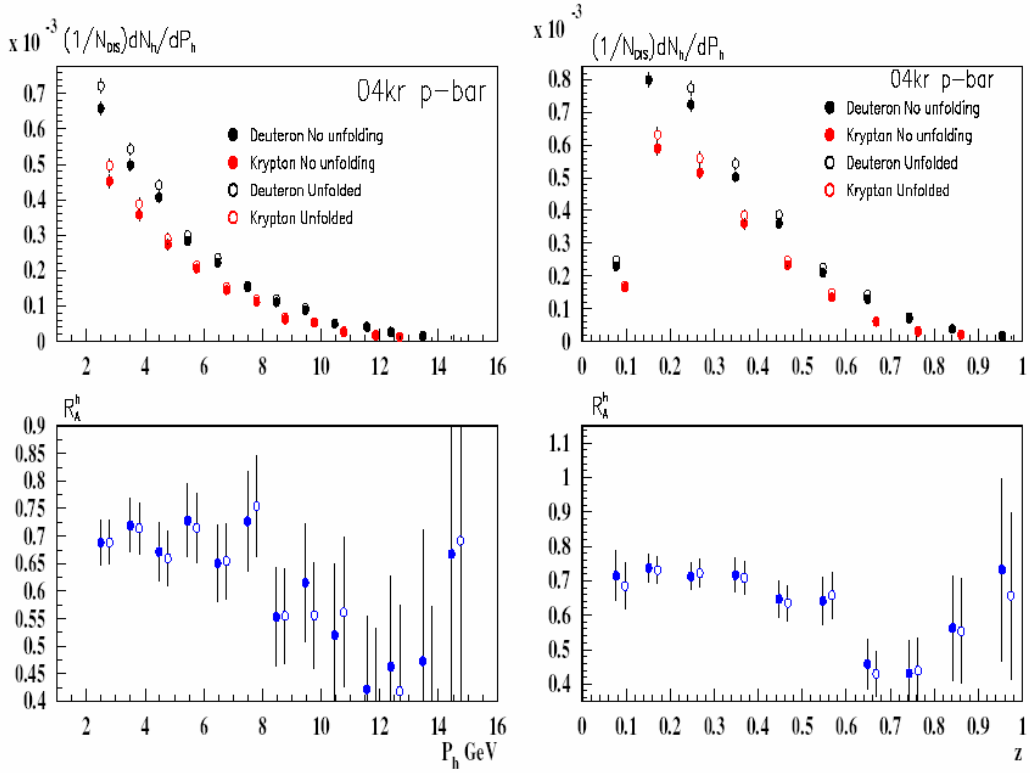

Figure A.6: Distributions of the multiplicities with and without the unfolding, versus the hadron momentum (left panel) and z (right panel) for anti-protons

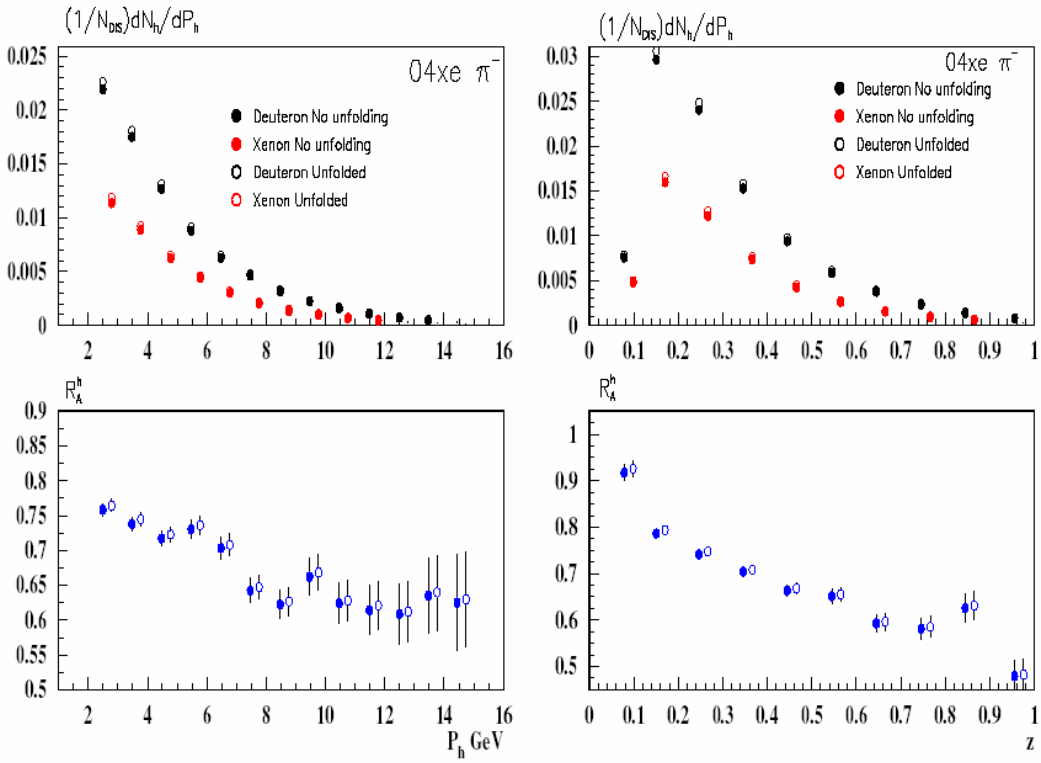

Figure A.7: Distributions of the multiplicities with and without the unfolding, versus the hadron momentum (left panel) and z (right panel) for negative pions

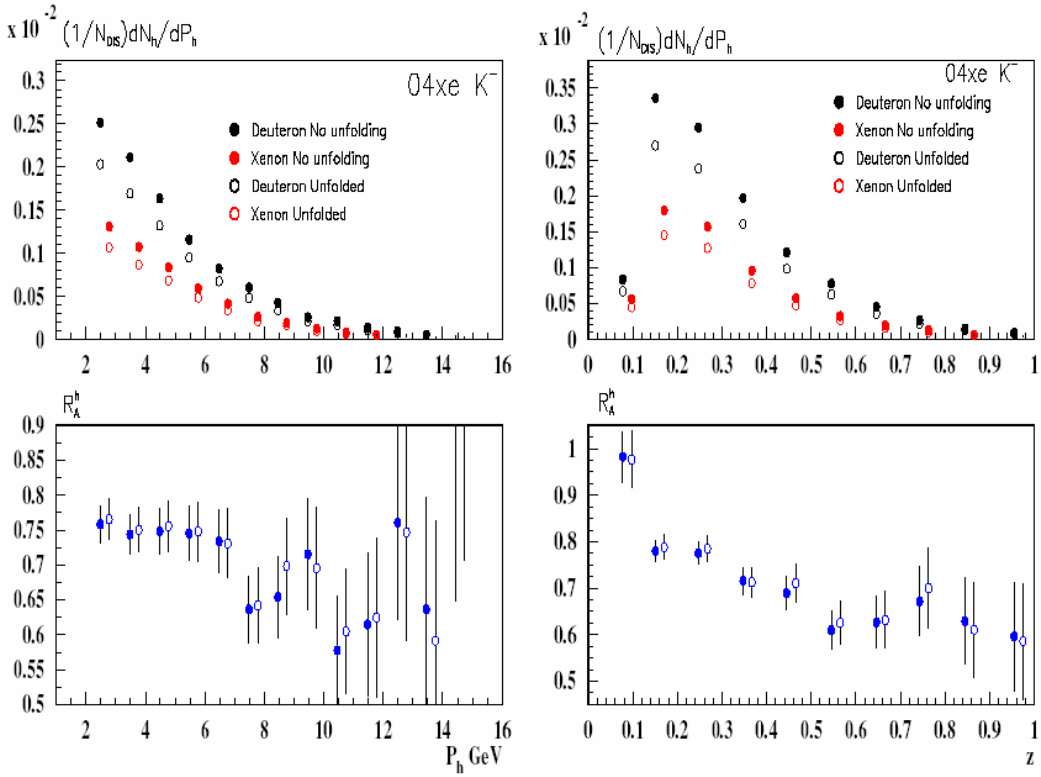

Figure A.8: Distributions of the multiplicities with and without the unfolding, versus the hadron momentum (left panel) and z (right panel) for negative kaons

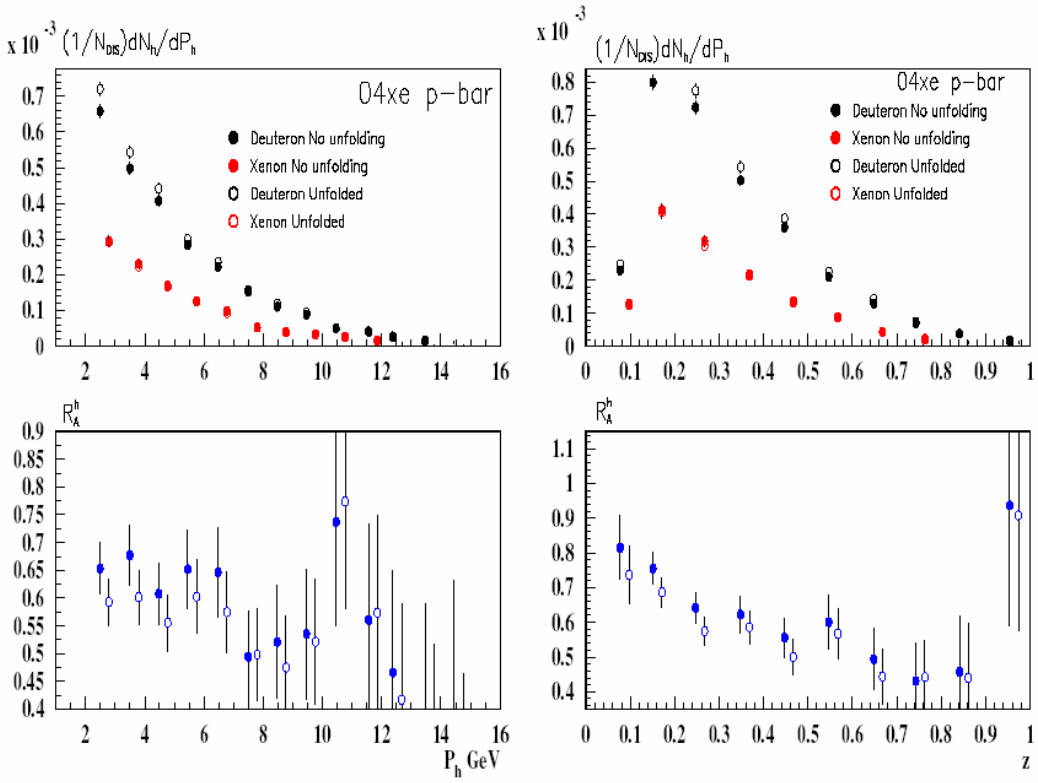

Figure A.9: Distributions of the multiplicities with and without the unfolding, versus the hadron momentum (left panel) and z (right panel) for anti-protons